Synthesis, Annealing Strategies and *in-situ* Characterization of Thermally Stable Composite Thin Pd/Ag Alloy Membranes for H_2 Separation

BY

M. ENGIN AYTURK

A PHD THESIS

SUBMITTED TO THE FACULTY OF THE

WORCESTER POLYTECHNIC INSTITUTE

IN PARTIAL FULFILLMENT OF THE REQUIREMENT FOR THE

DEGREE OF DOCTOR OF PHILOSOPHY

IN CHEMICAL ENGINEERING

BY

MAY 2007

APPROVED BY:

DR. YI HUA MA (ADVISOR)

DR. DAVID DIBASIO (HEAD OF DEPT.)

DR. NIKOLAOS K. KAZANTZIS
(COMMITTEE MEMBER)

DR. SATYA S. SHIVKUMAR
(COMMITTEE MEMBER)

TO DIDEM:

“YOU ARE THE REASON I *AM*…

YOU ARE *ALL* MY REASONS…”

Acknowledgements

First and foremost, I would like to take this opportunity to express my sincere appreciation and deepest gratitude to my advisor Prof. Yi Hua Ma for his excellence in scientific guidance, insight and continuous support. It has been an amazing experience and I had tremendous personal and professional growth under Prof. Ma's supervision. 谢谢你. I am also thankful to the research committee members Prof. Nikolaos Kazantzis and Prof. Satya Shivkumar for their continuous support and valuable suggestions.

This work wouldn't be complete without the continuous support, technical and experimental feedback provided by Dr. Erik E. Engwall and Dr. Ivan P. Mardilovich. I am very much indebted to Dr. Erik E. Engwall for all the encouragement and more importantly for his friendship. To my lab-mates over the past five years: Dr. Federico Guazzone, Ceylan Akis, Dr. Sutheerawat Shamingprai, Diana Otalvaro, Alpna Saini, Rajkumar Bhandari, Natalie Pomerantz and Chao-Huang Chen. Thank you for all the invaluable discussions, endless ideas and most of all, for your friendship in making this multi-cultural experience a remarkable one. The financial support provided by the Shell International Exploration and Production Inc. and Shell Hydrogen is also gratefully acknowledged. On behalf of the entire Shell Team, I would like to thank to Dr. Andreas Matzakos for his professionalism, dedication to research and for the synergy and motivation he has generated for this research.

I am also cordially grateful to Dr. Andrew Payzant and Dr. Scott Speakman at the high temperature materials lab (HTML) in Oak Ridge National Laboratories (ORNL) for the time and effort they have invested during the HTXRD experiments and also helping me to understand the key aspects of my research. I could not embrace more of your vast knowledge and experimental expertise.

I would like to thank the faculty of Chemical Engineering Department at WPI and the administrative staff, Sandra Natale, Joseph Kaupu, Elaine Brady and Felicia Vidito for their support and help during the last five years. I am sincerely thankful to Jack Ferraro and Douglas White for their assistance and ingenuity in equipment design and maintenance. Special thanks to Doug for all the fruitful discussions and the encouragement for the bass guitar.

Some people walk into our lives, leave footprints in our hearts and we are never the same after that. Nayef Alsindi, thank you for your generous friendship and sharing all that laughter with me. Special thanks go to Patrick Busch, Florentin Groeli, Kaan Yuksel, Kotaro Kobayashi, Dr. Ray J. Emerson, Liz Teixeira, Larry Capriotti, Arzu Atabek, Taskin Family, Bihter Padak and Erdem Sasmaz and many more for always being my friends now and then.

I would like thank to my parents Semiha and Mustafa Ayturk for their everlasting love and support. You taught me to be more committed to my dreams, to see opportunity in every difficulty and gave courage to discover new oceans in life. I miss you both very much. To my brother Gokhan: I believe in you even when the words aren't spoken and I always care about you even when we are apart. If I could reach up and hold a star for every time you made me proud, I would have the whole sky in the palm of my hand. I would also like to thank to my in-laws Umit and Mete Avcioglu, whose support and understanding had a profound impact on me from the very beginning. Thank you *Ümü* from the bottom of my heart for nurturing strength in my spirit with your tenderheartedness, candor and generosity. *Üstad*, you taught me to build a door if the opportunity doesn't knock and I am grateful for all the trust and love you have invested in me. I have gained invaluable experience since you have awakened me on the responsibilities that pertain to life and, I wanted to let you know that, you helped me make this possible. I would also like to thank to grandma-Avcioglu for her support, love and benevolent wishes.

Last, but definitely not the least, it is with the greatest of pleasure that I humbly dedicate this work to my beloved wife Didem. I am sincerely thankful to her precious existence, heavenly smile, for her unshakable faith in me, and her willingness to endure the vicissitudes of my endeavors in every step of the way over the past 10 years. I don't know if anyone has ever measured how much the hearth can hold, but all I know is I love you wholeheartedly and I always will.

"A mind that has been stretched will never return to its original dimension"

Albert Einstein

Abstract

Composite thin Pd/Ag alloy membranes with long-term thermal and chemical stabilities have potential applications for H_2 separation via catalytic membrane reactors and may be one of the key determinants to achieve the 21st century's global hydrogen economy.

This work provides a detailed microstructure characterization study and a better understanding of the fundamental principles involved in the synthesis of a novel Pd/Ag intermetallic diffusion barrier formed by the bi-metal multi-layer (BMML) deposition technique. The BMML deposition technique formed an extremely effective Pd/Ag intermetallic diffusion barrier and significantly improved the thermal and long-term stability of the composite Pd and Pd/alloy membranes over a temperature range of 500-600°C. In addition, high temperature annealing studies over a temperature range of 500-800°C in H_2 atmosphere led to a thorough understanding of the surface interactions and the phase changes between the Pd and Ag metals and the porous metal support elements (Fe, Cr and Ni) and it was shown by the SEI, EDX and X-ray phase analyses that the Ag/Fe and Ag/Ni binary systems exerted complete immiscibility compared to the completely miscible solid solutions of Pd/Fe and Pd/Ni phases.

A novel characterization method of *in-situ* time-resolved high temperature X-ray diffraction (HTXRD) analysis was used to elucidate the mechanistic details of the isothermal nucleation and growth kinetics of the Pd/Ag alloy phase over a temperature range of 500-600°C in H_2. The nucleation of the Pd/Ag alloy phase was instantaneous where the growth mechanism was through diffusion-controlled one-dimensional thickening of the Pd/Ag alloy layer. The Pd/Ag alloy phase growth was strongly dependent upon the deposition morphology of the as-synthesized Pd and Ag layers due to the presence of the heterogeneous nucleation sites. Based on the empirical rate constants derived from the solid-state reaction models, the estimated activation energies for the Pd/Ag alloy phase transformation were 236.5 and 185.6 kJ/mol and in good agreement with the literature values of 183-239.5 kJ/mol.

The successful utilization of surface modification techniques and modified plating conditions led to the synthesis of several dense Pd/Ag layers, which were as thin as 5-15 μm with a bulk Ag content in the 10-40 wt% range. The long-term testing of the composite Pd/Ag membranes (5-15 μm) at 500°C showed stable hydrogen permeances as high as 30 to 54 $m^3/m^2\text{-h-atm}^{0.5}$ with H_2/He selectivities ranging from 200 to 14000.

Furthermore, the atomic absorption flame analysis was used for the first time to elucidate the effects of temperature, initial metal ion concentration, initial hydrazine concentration and bath agitation on the electroless plating rates of Pd and Ag. The electroless plating of both Pd and Ag were strongly affected by the external mass transfer in the absence of bath agitation. The external mass transfer limitations for both Pd and Ag deposition have been overcome at or above an agitation rate of 400 rpm, resulting in a maximum conversion of the plating reaction and dramatically shortened plating times with the added advantage of uniform deposition morphology as evidenced by the SEI micrographs. Finally, the agitation rate of 400 rpm was successfully employed for the synthesis of composite Pd and Pd/Ag membranes. The H_2 permeance for a 4.7 μm thick pure-Pd membrane at 400°C was as high as 61 $m^3/m^2\text{-h-atm}^{0.5}$ with H_2/He selectivity over 310 after a total testing period of 690 hours.

Executive Summary

The successful utilization of catalytic membrane reactors for the production of pure hydrogen may be one of the key determinants to achieve the 21st century's global hydrogen economy. Worldwide R&D efforts for the development of inorganic membrane-based separation technologies have been steadily increasing for the past decade. Composite Pd and Pd/Alloy membranes prepared by the electroless plating on porous sintered metal supports are well-suited for the high purity hydrogen production in steam reforming reactors, as well as in hydrogen separation and purification. For the realization of economically viable membrane technologies, thin Pd and Pd/Alloy layers with high hydrogen permeation rates, high selectivity and long-term thermal and chemical stability are required. The main objective of this thesis was to provide a fundamental understanding to obtain highly selective, thermally and chemically stable, composite thin Pd/Ag alloy membranes and to investigate the role of Ag metal on the long-term stability and performance of the composite Pd/Ag alloy membranes via alternate synthesis routes and *in-situ* characterization techniques at high temperatures.

A detailed microstructure characterization study provided a better understanding of the fundamental principles involved in the synthesis of a novel Pd/Ag intermetallic diffusion barrier formed by the bi-metal multi-layer (BMML) deposition technique. The BMML deposition technique involves the formation of a porous Pd/Ag composite layer on the surface of the support by consecutive deposition of Pd and Ag layers with no intermediate surface activation and drying prior to the application of the dense hydrogen selective layer. By the use of the porous Pd/Ag barrier layer formed via the BMML developed in our group, the most significant improvement in membrane performance has been the increase in the safe operational temperature of the composite Pd/PSS and Pd/Alloy/PSS membranes at 500°C or above. The BMML deposition technique formed an extremely effective Pd/Ag intermetallic diffusion barrier and enhanced the thermal and the effective life of the composite Pd and Pd/Alloy membranes supported on porous

sintered metal tubes. The BMML deposition generated a certain extent of grading of the PSS support without affecting its overall resistance and made it possible to deposit a thin Pd and/or Pd/Ag layer.

The atomic absorption flame analysis was used for the first time for the determination of electroless plating kinetics of Pd and Ag metals. The effects of temperature, initial metal ion concentration, initial hydrazine concentration and bath agitation on the electroless plating rates of Pd and Ag were investigated extensively. It was found that the electroless plating of both Pd and Ag were strongly affected by the external mass transfer in the absence of bath agitation. The external mass transfer limitations for both Pd and Ag deposition have been overcome at or above an agitation rate of 400 rpm, resulting in maximum conversion of the plating reaction and dramatically shortened the plating times with the added advantage of uniform deposition morphology as evidenced by the SEI micrographs. The successful utilization of the plating solutions through the understanding of the electroless plating kinetics have a substantial impact on reducing both labor and manufacturing costs and furthermore, eliminating the necessity for a metal recovery or waste treatment unit.

In-situ annealing of a 12 µm thick Pd/Ag/PSS (12 wt% Ag) membrane showed that a temperature of 550°C led to the slow formation of a Pd/Ag alloy with subsequent enhancement in H_2 permeance and no significant leak formation, a process that was not complete even after 500 hours. Although the formation of uniform Pd/Ag alloys at an annealing temperature of 600°C has been verified by XRD studies, significant cluster sintering, also confirmed with the SEI micrographs, resulted in the progressive growth of the leak. These observations suggested that mild annealing temperatures with longer time duration may be needed to alleviate leak development.

The preparation of nano-crystalline Pd/Ag alloy particles was investigated as an alternative route for the synthesis of membranes with leak stability. Pd/Ag alloy nanoparticles with an average grain size of 4 nm and an Ag content of 25-30 wt% have been successfully synthesized at room temperature. Dip coating of the Pd/Ag alloy nanoparticles between electrolessly formed Pd and Ag layers led to a dense Pd/Ag (31 wt% Ag) membrane with a total thickness as thin as 4.6 µm and showed a hydrogen permeance of 32 m^3/m^2-h-$atm^{0.5}$ at 500°C. However, the selectivity of the Pd/Ag membrane was altered by the presence of Kirkendall voids and/or porosity.

Among several different approaches to form Pd/Ag alloys, *ex-situ* studies carried out by conventional X-ray point scanning detectors might fail to reveal the key aspects of the phase transformation between Pd and Ag metals during high temperature annealing. Therefore, a novel characterization method of *in-situ* time-resolved high temperature X-ray diffraction (HTXRD) analysis was again for the first time used to study the Pd/Ag alloy phase nucleation and growth kinetics in collaboration with the Oak Ridge National Laboratories. By the use of linear position sensitive detectors (LPSD), advanced optics and advanced software JADE-6.5, the isothermal phase evolution of the Pd/Ag alloy at 500°C, 550°C and 600°C under hydrogen atmosphere was quantified to elucidate the mechanistic details of the Pd/Ag alloy phase nucleation and growth pattern. The analysis of the *in-situ* time-resolved HTXRD data was achieved through the use of well-recognized solid-state reaction models (i.e., the Avrami kinetic model and the parabolic rate law) indicated that the nucleation of the Pd/Ag alloy phase was instantaneous where the growth mechanism was through diffusion-controlled one-dimensional thickening of the Pd/Ag alloy layer. Furthermore, the nucleation of the Pd/Ag alloy phase was through a heterogeneous nucleation mode. The cross-section SEI micrographs indicated that the Pd/Ag alloy phase growth was strongly dependent upon the deposition morphology of the as-synthesized Pd and Ag layers. Based on the empirical rate constants derived from the solid-state reaction models used in this study, the estimated activation energies for the phase transformation were 236.5 and 185.6 kJ/mol and in good agreement with the literature values of 183-239.5 kJ/mol.

The hole blowing technique (HBT) was developed to selectively deposit Pd and Ag metals by targeting only the pore mouth and valleys located at the outer surface of the metal support by processing both the activation and plating solutions, particularly Ag, through the tube-side of the membrane tube by the use of pressurized air. As confirmed by the cross-sectional SEI micrographs, selective deposition via the HBT was effective in blocking the large pores on the surface of the support metal by taking advantage of the dendritic growth characteristics of the Ag clusters. In addition, increasing the concentration of the electroless Ag plating solution 20 folds resulted in the formation of uniform Ag deposits due to the increase in the total number of nucleation sites on the surface of the support metal. The modified Ag plating bath chemistry was used to form almost gas tight Ag layers over a thickness range of 2-5 μm and led to the synthesis of dense Pd/Ag layers with Ag contents as high as 40 wt%. Moreover, bath agitation at or above a stirring rate of 200 rpm not only had a substantial impact on the plating rates but also provided an improved deposition morphology for both Pd and Ag metals.

The gradual smoothing of the metal support surface was achieved via depositing $Al(OH)_3$ powder from a $Al(OH)_3$ grading solution in a reduced number of synthesis steps. Detailed FT-IR and XRD analyses revealed that the ~60% of the support pores filled with the $Al(OH)_3$ powder transformed to a denser state at high temperatures (350-500°C). From a standpoint of support surface modification with small effect on the mass transfer resistance as the result of the low residual volume of $Al(OH)_3$ formed at high temperatures.

The aforementioned use of surface modification techniques coupled with the modified plating conditions led to the synthesis of several dense Pd/Ag layers, which were as thin as 5-15 μm with a bulk Ag content in the 10-40 wt% range. After testing at 500°C for several hundred hours, the hydrogen permeance of the composite Pd/Ag membranes (5-15 μm) were as high as 30 to 54 m^3/m^2-h-$atm^{0.5}$ with H_2/He selectivities ranging from 200 to 14000, which were in close proximity to the industrial standards set for the commercialization of the membrane technologies.

The research conducted along this dissertation provides a better understanding on the synthesis, characterization and long-term testing of thermally stable composite thin Pd/Ag alloy membranes by elucidating the mechanistic details via *in-situ* methodologies, which can be directly applied for the development of large scale robust technologies for hydrogen separation and integrated in industrial steam reformer reactors.

Table of Contents

List of Figures

List of Tables

1. Introduction

Mankind's energy needs have evolved for centuries and are continuing to evolve today. From wood to animal fat, to coal, to petroleum, to natural gas, we have used a succession of fuels for heating, manufacturing, lighting and transportation. Hydrogen is the latest in the succession as an energy carrier, with many social, economic and environmental benefits to its credit. Hydrogen is used extensively today to make ammonia, methanol, gasoline, heating oil, and rocket fuel. It is also used to make fertilizers, glass, refined metals, vitamins, cosmetics, semiconductor circuits, soaps, lubricants, cleaners, and even margarine and peanut butter. Hydrogen is the simplest and the ubiquitous element in the universe, which is colorless, odorless, tasteless and non-poisonous. Hydrogen is the third most abundant element on the Earth's surface and mostly found in combination with oxygen as water, then in fossil fuels like petroleum, coal and natural gas and it is in plants and organic waste. Over the next several decades, it is imminent that we will all begin to see an amazing shift away from the fossil fuel economy we have today toward a much cleaner hydrogen future, what is broadly known as the hydrogen economy-widespread and diverse production and use of hydrogen.

Currently, every aspect of modern existence is made from, powered with, or affected by fossil fuels. While fossil fuels have played an important role in getting society to the point it is today, there are numerous big problems that fossil fuels create, including environmental pollution, energy policy concerns, global climate change, local air quality, noise and security of energy supply and most importantly, the economic dependence on oil-rich countries, which generate technological, economic and political barriers that keep us bound to petroleum and other fossil fuels. The hydrogen economy promises to eliminate all of the problems that the fossil fuel economy generates. However, this could only be achieved by a combination of technological innovation, global cooperation and strategic thinking and a determination to take oil off the international chessboard of power politics and replace it with the ultimate energy carrier, hydrogen.

As also noted by Don Huberts from Shell Hydrogen "*The stone age didn't end because they ran out of stones; the oil age won't end because we run out of oil*" (Walker, 2001). The hydrogen economy is simply the urge to provide better standards for the continuous evolution of mankind, which can be considered as a promissory note for a safer world.

Hydrogen can be produced from a wide range of sources by a number of different routes such as electrolysis, photoelectrolysis, biological methods, partial oxidation and steam reforming[*]. Electrolysis is simply the use of electric current to split water into hydrogen and oxygen. The most common form of electrolysis, being alkaline electrolysis, has been used industrially for over 80 years but is now used on large scale only where cheap electricity is available, since electrolysis is the most energy-intensive way to produce energy. However, there exists sufficient interest in very small scale electrolysers such as domestic applications.[†] Photoelectrolysis on the other hand, uses solar cells that split water without use of electricity and it is considered to be one of the most promising technologies. Several types of bacteria (i.e., microalgae) can produce hydrogen by photosynthesis or by fermentation. Although some methods may have commercial potential, most are at the R&D stage. Partial oxidation is achieved by reacting heavier hydrocarbons (i.e., oil, coal) with oxygen and steam, which is a commercially available process and is of interest for countries with large coal resources[‡]. The commercially usable high purity hydrogen currently is being produced mostly from steam reforming of natural gas via wet-scrubbing (H_2 purity: 97%) and pressure swing adsorption (H_2 purity:

---

[*] www.hydrogen.energy.gov
[†] www1.eere.energy.gov
[‡] www.hyweb.de/index-e.html

99.8%) type process technologies[§]. One drawback of steam reforming reaction is the CO_2 released to the atmosphere, which is considered as a greenhouse gas.

The worldwide annual production of hydrogen in 2001 was estimated to be 35 million tons[**], which increased to 50 million tons as of 2006[††]. The future hydrogen demand is also expected to increase due to increased use for hydrodesulfurization of heavy, sour crude oils, fuel cells for both stationary and mobile applications, home heat and power, distributed power generation, fleet vehicles and automobiles and other chemical and petrochemical applications including reformulated gasoline.

The production of ultra-high purity hydrogen (>99.999%) can be achieved through the successful utilization of membrane separations and membrane reactors. If hydrogen can selectively be removed from the highly endothermic reaction systems that require high reaction temperatures to attain industrially acceptable levels of conversion, such equilibrium-limited reactions can achieve higher conversions at lower temperatures (Kikuchi, 2000). Combining reaction and membrane separation in a membrane reactor offers additional advantages such as savings on energy consumptions, reducing costs, prolonging the life of reactor materials and catalysts, simplified downstream separation and recovery and improved selectivity (Shu *et al.*, 1991a). Indeed, high pressure CO_2 formed during the steam reforming of methane in a membrane reactor is suitable for sequestration via tertiary oil recovery or storage into deep saline aqufiers.

In this respect, dense composite Pd and Pd/alloy membranes supported on a porous substrate are well-suited for high temperature hydrogen separation and for the production of pure hydrogen via membrane reactor applications. The choice of porous substrates used for the fabrication of Pd and Pd/alloy membranes include ceramic, porous glass, tantalum, ceramic hollow fibers, vanadium-nickel and porous sintered metal supports (PM). Porous sintered metal supports (i.e., porous stainless steel (PSS), porous Hastelloy (PHST) and Inconel) are promising candidates due to their various advantages over other substrates such as having similar thermal expansion coefficients between the membrane metals (i.e., Pd, Ag and Cu), providing good mechanical strength, being less fragile and

---

[§] http://fossils.energy.gov/

[**] CryoGas International, 2001

[††] www.cleanenergy.org

resistant to cracking, and allows operation at high pressures and temperatures. Furthermore, composite Pd/PM and Pd/Alloy/PM membranes, welded from both ends with non-porous support tubes, can be assembled and integrated into a process stream very easily.

The deposition of the metal film on the porous substrates can be accomplished by several techniques including electroplating, electroless plating, chemical vapor deposition, magnetron sputtering, spray pyrolysis, e-beam evaporation and many others. Among these techniques, the main advantages of electroless plating are providing membranes without pinholes and cracks, uniform deposition on complex geometries and large surface areas, hardness of the deposited film, good adhesion to the substrate, simple equipment and easy to scale-up. One problem yet to be solved associated with the electroless deposition of Pd and Pd/alloy membranes on PM supports is the intermetallic diffusion of support elements (Fe, Cr and Ni) into the membrane layer, which results in a significant loss of hydrogen permeance. This can be avoided by the utilization of a diffusion barrier layer between the PM support and the membrane film such as the use of an oxide layer or a novel Pd/Ag barrier layer. The technology regarding the formation of an intermediate intermetallic diffusion by the controlled *in-situ* oxidation of the PM supports or by forming a Pd/Ag barrier layer via the bi-metal multi-layer (BMML) deposition technique have already been developed by Ma *et al.* (2000; 2007).

In the case of pure Pd membranes, nucleation of β-hydride phase of Pd from the α-phase introduces severe lattice strains, in which $\alpha \leftrightarrow \beta$ phase transformations during hydrogen loading/un-loading and temperature cycles cause pure Pd membranes to become brittle. Although hydrogen embrittlement is one of the main issues that greatly affect the long-term stability and the life of the Pd membranes, it can be avoided by alloying Pd with other metals such as Ag, Cu, Au, Y, Ce and etc. The addition of an alloying metal narrows the region corresponding to the miscibility gap of the α and β phases. Pd alloys are attractive not only in terms of overcoming H_2 embrittlement, but also due to several other reasons such as, cost reduction of about ~50% for Pd/Ag (23 wt% Ag) and ~57% for Pd/Cu (40 wt% Cu) alloys, improved resistance to H_2S in the case of Pd/Au and Pd/Cu alloys and enhanced hydrogen permeability at certain alloys compositions compared to that of pure palladium.

Among various binary and ternary alloys of Pd, the Pd-Ag-H system is particularly interesting. One of the net alloying effects for the Pd/Ag alloys is the shift in the α↔β transformation, in which the transition follows a smoother path above 20 wt% Ag and disappears above 30 wt% Ag. The heat of solution of the Pd/Ag alloys increases with the Ag content and the interaction between the intersititial hydrogen and the Ag ion results in an increase in solubility. As a result of these simultaneous changes, permeability of Pd/Ag alloy membranes reaches a maximum at an Ag content of 20-25 wt%. It is believed that hydrogen in Pd/Ag alloys occupies energetically higher tetrahedral sites with respect to hydrogen occupancy at lower energy octahedral sites in the case of pure Pd. Indeed, the hydrogen distribution follows a disordered pattern in Pd-Ag-H system and hydrogen adsorption at different sites in Pd/Ag alloys differs significantly. These changes are strongly dependent on both temperature and the Ag content of the alloy.

The main objective of the research conducted within the context of the present dissertation was to understand the fundamental principles involved in the synthesis, H_2 permeation characteristics and the long-term thermal and chemical stabilities of composite Pd and Pd/Ag membranes formed by the electroless plating technique on porous sintered metal supports. In summary, the specific objectives of this study were:

- ◊ To understand electroless deposition morphology of Pd and Ag metal on porous sintered metal supports.
- ◊ To understand and characterize the hydrogen transport mechanism through composite Pd/Ag membranes.
- ◊ To provide a detailed microstructure characterization analyses and a better understanding of the concepts involved in the synthesis of a novel Pd/Ag intermetallic diffusion barrier formed by the bi-metal multi-layer (BMML) deposition technique and to investigate its long-term stability and effectiveness as a barrier layer against intermetallic diffusion.

- ◊ To understand the effect of high temperature annealing on the formation of Pd/Ag alloy layers via thorough microstructure characterization analyses.
- ◊ To understand the nucleation and growth kinetics of the Pd/Ag alloy phase transformation.
- ◊ To understand the intermetallic diffusion mechanism by studying the surface interactions and the phase changes between the support metals (Fe, Cr and Ni) and the Pd and Ag layers and the respective effects on the hydrogen permeance.
- ◊ To understand how the conventional electroless Ag plating baths can be modified to obtain uniform deposition layers and to study the effect of Ag metal on the long-term thermal and chemical stability of composite Pd/Ag membranes.
- ◊ To understand the possible mechanisms that lead to the formation of progressive leak growth in composite Pd/Ag membranes and investigate ways to mitigate leak growth.
- ◊ To understand how the electroless plating process and the surface modification techniques can be utilized to achieve thin Pd/Ag membrane layers.
- ◊ To understand the effect of external mass transfer on the electroless plating rates and the deposition morphologies of Pd and Ag.

2. Literature Review

2.1. The Pd-H System

The hydrogen permeability of transition metals was first observed by Deville and Troost (1863) and Deville (1864). Soon afterwards, the measurements carried out by Graham (1866) on a tube of palladium indicated that not only did Pd permit high quantities of hydrogen but also large volumes of hydrogen were absorbed by the tube when it was cooled down to room temperature in an atmosphere of hydrogen. Graham (1866) used the term “occluded” for his observations on the absorption of hydrogen by palladium. From Graham (1866) onwards, the high solubility and diffusivity of hydrogen in palladium in comparison to other elements over a wide range of temperature and pressures of hydrogen gas has long been a fascination for scientists and has attracted a larger number of experimental investigations more than any other metal/gas system Lewis (1967).

The first measurements relating the pressure of hydrogen to the hydrogen content in the solid (i.e., cast palladium) were reported by Troost and Hautefueille (1874). A much more comprehensive series of measurements were conducted by Bruning and Sieverts (1933), Gillespie and Galstaun (1936), Wicke and Nernst (1964), Frieske and Wicke (1973) and more recently by Latyshev and Gur’yanov (1998) to construct the isotherms and isobars of the Pd-H system over a wide range of temperature and pressures. The Pd-H phase diagram shown in Figure 2-1 describes the equilibrium pressure and temperature for bulk Pd as a function of hydrogen content. As can be depicted in Figure 2-1, the Pd-H phase diagram separates into two distinct regions of low and high hydrogen concentrations, which are defined as the α- and β-phases of the Pd hydride, respectively.

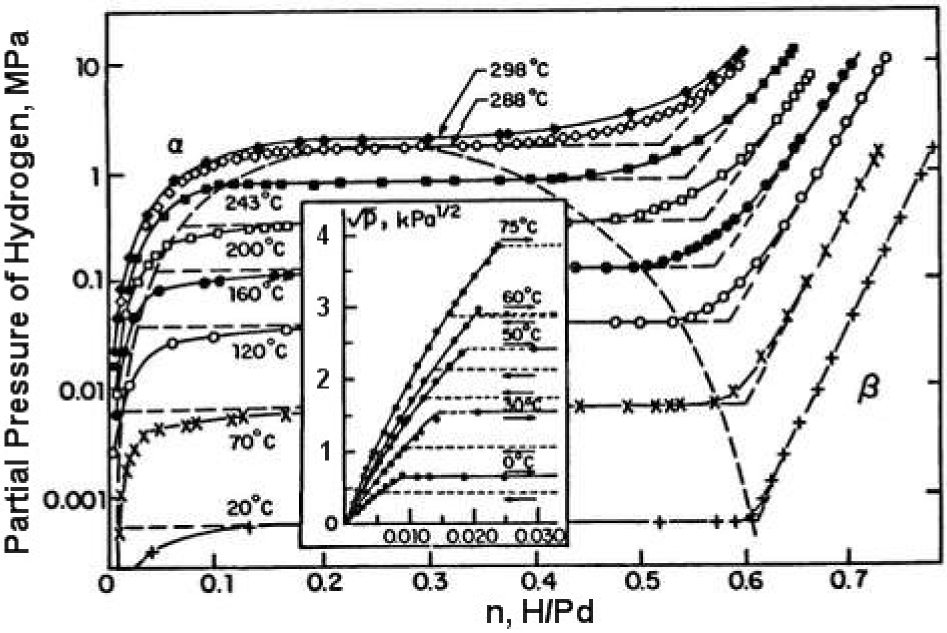

Figure 2-1: P-n-T phase diagram for the Pd-H system

At low hydrogen concentrations, the equilibrium pressure shows a continuous increase in the α-phase of the Pd-H system. The hydrogen concentration at and above the region of invariant pressure in Figure 2-1 corresponds to the maximum solubility of hydrogen in the α-phase and has been termed as α_{max} by Flanagan and Lewis (1959) and Wicke and Nernst (1964). α_{max} also represents the hydrogen concentration above which a new hydride phase, β-phase, begins to nucleate. The subsequent region of invariant pressure, or plateau region, in Figure 2-1 corresponds to ranges of hydrogen concentration where α- and β-phase hydrides of Pd co-exist. As the hydrogen concentration increases over the region exhibiting a miscibility gap between the α- and β-phase hydrides of Pd, there is a continuous transformation from α- to β-phase (Lewis, 1967). Both the α- and β-phase hydrides of Pd exhibit a face-centered cubic (fcc) crystal structure and only differ in their lattice constants, where the lattice parameter increases by about ~3% in the β-phase (Lewis, 1967). The transitions between α- and β-phase usually do not correspond to a change in the lattice structure, rather given as the lattice dilatation, in which the lattice constant of Pd, 3.891 Å, changes to 3.894 Å and 4.018 Å for hydrogen loadings of $PdH_{0.03}$ and $PdH_{0.6}$ respectively. Finally, the equilibrium pressure in Figure 2-1 begins to increase with the solution of additional hydrogen in the β-hydride phase. The composition at the end of the region of invariant pressure corresponds to the composition of the β-phase region, which was termed as β_{min} by Wicke and Nernst (1964).

The region corresponding to the miscibility gap in Figure 2-1 is subject to both a gradual increase in α_{max} and a decrease of β_{min} up to a critical temperature, which coincides at a complementary critical hydrogen concentration and a critical pressure. The existence of such a critical isotherm at ~300°C was first reported by Bruning and Sieverts (1933). As confirmed by the measurements of Gillespie and Galstaun (1936), the α- and β-phase hydrides co-exist below a critical temperature, T_c, of 295.3°C with values of 19.8 atm and n=H/Pd=0.27 for the critical pressure, P_c and corresponding hydrogen concentration, respectively. Similarly, Latyshev and Gur'yanov (1998) have reported the values of 300°C, 2 MPa and n=H/Pd=0.25 for the critical temperature, pressure and hydrogen concentration, respectively. The accurate determination of the critical isotherm and maximum attainable hydrogen concentration, α_{max}, of the α-hydride phase of Pd is of great importance with regard to the practical applications of Pd membranes for the hydrogen separation and purification technologies. Below the critical parameters reported by Gillespie and Galstaun (1936), the nucleation of the β-hydride phase of Pd from the α-phase introduces severe lattice strains, in which $\alpha \leftrightarrow \beta$ phase transformations due to the hydrogen loading/un-loading and temperature cycles causes pure Pd membranes to become brittle. The continuous phase transformations between the α- and β- phase hydrides of Pd below ~300°C give rise to a very well known phenomenon, deemed as the "hydrogen embrittlement" (Lewis, 1967). The hydrogen embrittlement is one of the main issues that severely affect the chemical stability and the durability of the pure Pd membranes due to the formation of micro-cracks caused by the β-phase nucleation, which ultimately may lead to a complete loss of hydrogen permselectivity. The occurrence of the hydrogen embrittlement has been related to the formation of micro-cracks by various mechanisms such as the pressure theory, the reduced surface energy theory, the de-cohesion theory, the H_2 phase change theory and H_2 enhanced local plasticity theory (Shu *et al.*, 1997)

The pressure theory assumes that, dissolved hydrogen in the Pd lattice forms molecules in cavities and micro-cracks which generate high pressure at local stress points and result in cracking of the membrane. The reduced surface energy theorem attributes the crack propagation to the decreasing surface free energy of metals due to hydrogen absorption. The de-cohesion theory relates hydrogen embrittlement with a decreased metal bond strength in the presence of hydrogen. On the other hand, according to the hydrogen related phase change theory, embrittlement is due to the stabilization of a brittle hydride phase both by the presence of hydrogen and the stress fields around the crack tips. Finally, hydrogen enhanced local plasticity mechanism associates the initiation and propagation of fractures and the hydrogen embrittlement to an enhancement of ductility at the crack tips.

One way to overcome the hydrogen embrittlement is to carefully control the operating pressure and temperature. On the other hand, phase transformations between the α- and β-hydride phases of Pd and the associated hydrogen embrittlement can be overcome by alloying Pd with other metals such as Ag, Cu, Au, Y, Ce and etc.

2.2. The Pd-Alloy-H Systems

In comparison to pure Pd, Pd/alloys are attractive due to several reasons such as being less prone to hydrogen embrittlement, less expensive and desired due to their cost reduction benefits which are as high as ~50% for Pd/Ag alloys (~23%) and 57% for Pd/Cu alloys (~40% Cu), providing improved resistance to H_2S poisoning in the case of Pd/Au and Pd/Cu alloys and enhanced hydrogen permeability at certain alloy compositions (Lewis, 1967; Knapton, 1977; Kikuchi and Uemiya, 1991; Shu *et al.*, 1991a; Uemiya *et al.*, 1991a; Mardilovich *et al.*, 1998a; Gryaznov, 2000; Ma *et al.*, 2003).

The region corresponding to the miscibility gap of α- and β-hydride phases of Pd narrows with the addition of an alloying metal. In particular, the critical temperature for certain compositions of Pd/alloys is known to decrease and therefore, suppress the adverse effects of hydrogen embrittlement that lead to severe deformations in the shape and microstructure of pure Pd films as discussed by Lewis, 1967. A specific example is demonstrated in Figure 2-2 by a comparison between pure Pd and Pd/Ag alloy (25% Ag) after 30 cycles of heating and cooling in hydrogen atmosphere (Hunter, 1960).

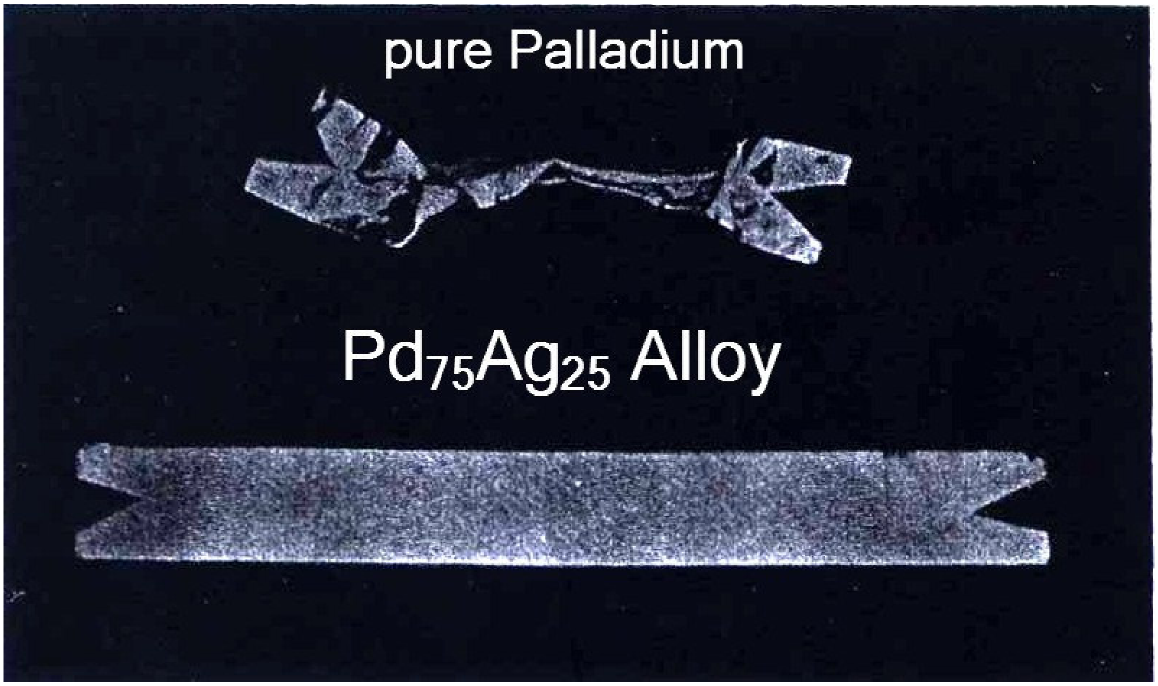

Figure 2-2: Comparison of the appearance of pure Pd and a Pd/Ag alloy (25% Ag) after 30 cycles of heating and cooling in hydrogen at atmospheric pressure(Hunter, 1960)

The stability of the Pd/Ag alloy (25% Ag) film shown in Figure 2-2 was also in good agreement with the early observations of Graham (1869b) on the resistance of certain Pd/Ag alloys against deformations that occur during the cycles of hydrogen absorption and desorption.

2.2.1. Pd/Ag Alloys

The role of Ag in the Pd-Ag-H system is analogous to that of hydrogen atom in Pd, where both hydrogen and silver give up only one electron per atom (Holleck, 1970). Due to its electron donating nature similar to the hydrogen atom, both Ag and hydrogen atoms compete for the filling of the electron holes in the 4d band of palladium (Shu *et al.*, 1991a). From a thermodynamic point of view, the changes in the chemical potential of the system, are associated with both proton and the electron components of the Pd-Ag-H system (Latyshev and Gur'yanov, 1998). Although the proton contribution is believed to associate with the lattice deformation that leads to an attractive interaction between the dissolved hydrogen, the electron contribution, on the other hand, simply reflects the rise of the Fermi level[*] of the Pd-Ag-H system due to the electrons of the dissolved hydrogen atoms. Once the 4d band of Pd is filled and the filling of 5s band starts, the Fermi level of the Pd-Ag-H system increases, which has been associated with the increase in equilibrium pressure (or the chemical potential for hydrogen absorption) due to the nucleation of β-hydride phase. According to Brodowsky and Poeschel (1965), the isotherms of the Pd/Ag alloys in the 10-20% Ag range are comparable to that of the Pd-H system due to the presence of the regions of pressure invariance where α- and β-phase hydrides co-exist. However, with the increasing Ag content, both the partial pressure of hydrogen over the plateau (invariant pressure) regions and the hydrogen content of the β-phase (β_{min} in Figure 2-1) decrease to lower values of H/Me as shown in Figure 2-3[a]. As depicted from Figure 2-3[a], the transition region follows a smoother path above 20% Ag and finally disappears after 30% Ag. These results were also in excellent agreement with the observations of Axelrod and Makrides (1964) and Carson and Lewis (1967).

---

[*] In physics, the Fermi energy is defined as the smallest possible increase in the ground state energy when exactly one particle is added to the system, which is equivalent to the chemical potential of a system in its ground state at absolute zero. In this respect, the Fermi level corresponds to the collection of lowest possible energy states of electrons at absolute zero (http://en.wikipedia.org/).

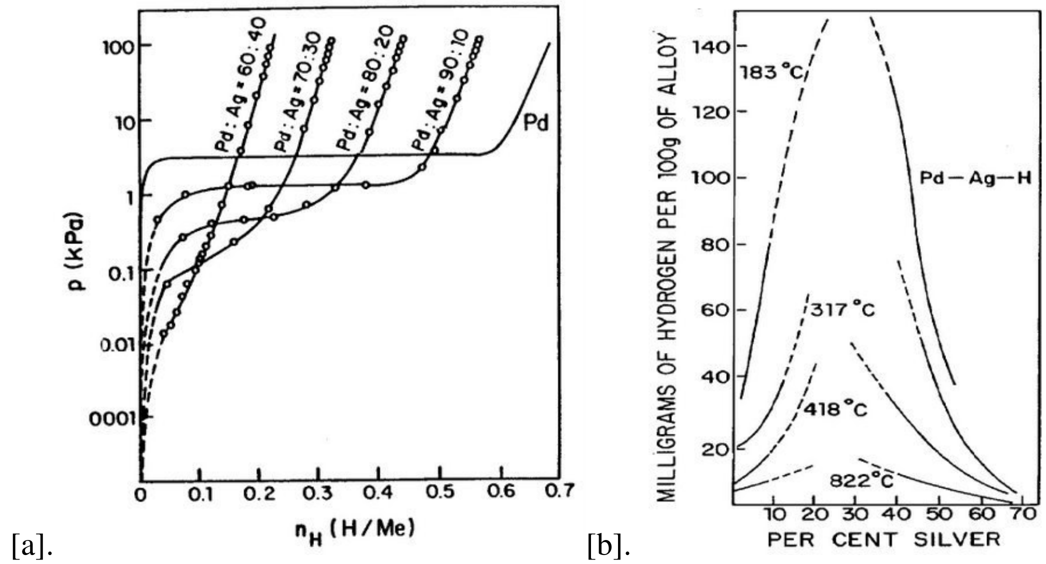

[a]. [b].

Figure 2-3: [a]. Equilibrium solubility isotherms of hydrogen in Pd and Pd/Ag alloys at 50 ℃ by (Brodowsky and Poeschel, 1965) and [b]. The solubility of hydrogen in Pd/Ag alloys at 1 atm (Sieverts et al., 1915)

For Pd/Ag alloys, it is therefore expected that the nucleation of β-hydride phase starts at lower hydrogen concentrations, as shown in Figure 2-3[a]. Hence, the net alloying effect for the Pd/Ag alloys is a significant decrease in the critical temperature and pressure for the α- to β- phase transition and a sharp increase in hydrogen solubility as shown in Figure 2-3[b]. According to Makrides (1964), Pd/Ag alloy produces two distinct effects in solubility: (a) The solubility of hydrogen at low pressures (below the critical pressure for the α-β phase transition) increases up to a Ag content of 25 at%, as a result of an interaction between an interstitial hydrogen and a silver ion, (b) Then, the maximum solubility as shown in Figure 2-3[b] decreases with the increasing Ag content above 30 at% Ag which is most probably caused by the changes of the electronic structure of the solid solution associated with the introduction of the Ag into the Pd lattice.

Pd/Ag alloys are also attractive from the standpoint of providing high hydrogen permeability with respect to pure Pd. The permeability, Q_H, is the product of hydrogen diffusivity, D_H, and solubility coefficients, S_H. In general, hydrogen diffusivity in different metals varies only by a small factor whereas the changes in solubility are reaslized by several orders of magnitude. In the case of Pd/Ag alloys, the increase in hydrogen solubility with the subsequent decrease in diffusivity as a function of the Ag content of the alloy, result in a maximum in hydrogen permeability between 20-30 wt% Ag, corresponding to 1.7-2.0 times the permeability of pure Pd (Hunter, 1960; McKinley, 1969; Holleck, 1970; Gryaznov, 2000).

2.2.2. Pd/Cu, Pd/Au and Other Pd/Metal Alloys

Pd/Cu alloys are also attractive for low temperature hydrogen separation applications, which do not undergo $\alpha \leftrightarrow \beta$ phase transformation since the critical temperature for the β-hydride phase for a Pd/Cu alloy with 40 wt% Cu is below the room temperature (Karpova and Tverdovskii, 1959). The hydrogen diffusivity for a Pd/Cu alloy (53 wt% Cu) with a body centered cubic (bcc) phase ($\sim 10^{-8}$ m^2/s at 250°C) is estimated to be ~2 orders of magnitude higher than the disordered fcc phase of the same Pd/Cu alloy (53 wt% Cu) ($\sim 10^{-8}$ m^2/s at 250°C) and also an order of magnitude higher than the hydrogen diffusivity of pure Pd ($\sim 10^{-9}$ m^2/s at 250°C) (Shu *et al.*, 1991a). Unlike Pd/Ag alloys, the maxima in hydrogen permeability in bcc Pd/Cu alloys are mainly attributed to the changes in diffusivity despite the reduced solubility of hydrogen in bcc phase (Subramanian and Laughlin, 1991; Kamakoti and Sholl, 2003). Indeed, hydrogen permeability of bcc Pd/Cu alloys reaches a maximum at a Cu content of 40 wt%, showing an only 10% improvement with respect to the hydrogen permeability of pure Pd (McKinley, 1967).

Pd/Cu alloys are also known to be highly resistant to sulfur compounds such as H_2S depending on the crystal structure (Gao *et al.*, 2004; Morreale *et al.*, 2004; Kamakoti *et al.*, 2005). The chemical stability of Pd/Cu alloys against sulfur poisoning is essentially favorable for the coal gasification applications and has attracted a wide range of research interest in membrane synthesis, characterization and modeling (Uemiya *et al.*, 1991b; Nam and Lee, 2001; Howard *et al.*, 2002; Roa *et al.*, 2002; Kamakoti and Sholl, 2003; Roa and Way, 2003a; Roa *et al.*, 2003; Hoang *et al.*, 2004; Howard *et al.*, 2004; Gao *et al.*, 2005; Kamakoti *et al.*, 2005; Kulprathipanja *et al.*, 2005; Roa and Way, 2005).

In addition, Pd/Au alloys are also known to be one of the most robust systems in environments where poisoning of pure Pd membranes by chemical contaminants such as H_2S is problematic. Similar to Pd/Ag alloys, the solubility of hydrogen in Pd/Au alloys possesses a maximum between 20-40% Au, however, the maxima becomes less marked with the increasing temperature above 400°C (Sieverts *et al.*, 1915; Lewis, 1967; Sonwane *et al.*, 2006b). In conjunction with their enhanced sulfur resistance, Rodina *et al.* (1971) have reported that the addition of a small amounts of Au increased the permeability of Pd/Ag alloys significantly and helped to improve the long-term stability of membranes during temperature cycling. However, the effect of Au content on the performance of Pd/Au alloys compared to that of pure Pd appears to be contradictory between different researchers. According to McKinley (1967) and Knapton (1977), the hydrogen permeability of Pd/Au alloys within 5-20 wt% Au was comparable to that of pure Pd and only differed by a factor of 1.1 at 350°C. On the other hand, Gryaznov (2000) have reported that the hydrogen permeability of Pd/Au alloys (5-20 wt% Au) at 500°C were 2 times higher than that of pure Pd. Since very few studies have been conducted for Pd/Au alloys regarding membrane applications, the uncertainty of the role of Au content on hydrogen permeability needs further examination. The maximum hydrogen permeability for the Pd/Ag alloys at 350°C reported by Knapton (1977) was in the range of 20-25 wt% Ag while Gryaznov (2000) reported a broader range of 30-40 wt% Ag at 500°C.

Figure 2-4 summarizes the trends exhibited by the maximum hydrogen permeability for various other metals with respect to pure palladium (McKinley, 1967; Knapton, 1977; Shu *et al.*, 1991a; Gryaznov, 2000). For instance, Yttrium (Fort *et al.*, 1975) and Cerium (Farr and Harris, 1973) exhibit superior permeability with a smaller amount of alloying metal (5-12 wt%). Although the Y content of the Pd/Y alloys is limited to a maximum value of 12 at% by the phase equilibrium, both Y and Ce alloys of Pd can withstand high pressure differences compared to Pd/Ag alloys (23 wt%) (Shu *et al.*, 1991a). Among various other metals studied for alloying purposes, such as Fe, Ru, Rh, Ni, Cr and V, no significant improvement in the hydrogen permeability has been observed compared to the binary alloys of Pd, such as Pd/Ag, Pd/Au, Pd/Cu, etc. (Shu *et al.*, 1991a). Furthermore, Gryaznov (2000) have studied the ternary Pd/alloys including Pd/Ag/Rh and Pd/Ru/In systems. The normalized permeability data for the binary and tertiary Pd/alloy systems are summarized in Table 2-1 (McKinley, 1967; Knapton, 1977; Shu *et al.*, 1991a; Gryaznov, 2000; Ma *et al.*, 2003).

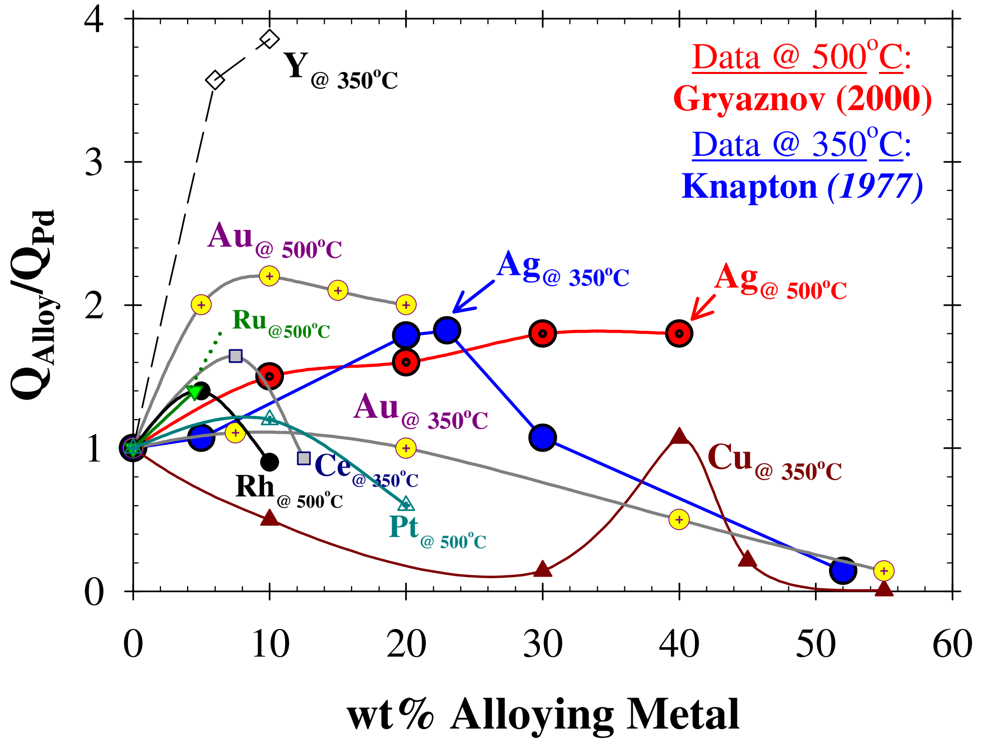

Figure 2-4: Hydrogen Permeability Benchmarking for Pd/Alloy membranes at 350℃ and 2.2 MPa (Knapton, 1977) and 500℃ (Gryaznov, 2000)

Table 2-1. Improvement in hydrogen permeability for the binary and ternary Pd alloys at 350℃ (McKinley, 1967; Knapton, 1977; Shu et al., 1991a; Gryaznov, 2000; Ma et al., 2003)

Alloy Metal	wt% for Maximum Permeability	Normalized Permeability (Q_{alloy}/Q_{Pd})
Y	10	3.8
Ag	23	1.7
Ce	7.7	1.6
Cu	40	1.1
Au	5	1.1
Ru, In	0.5, 0.6	2.8
Ag, Ru	30, 2	2.2
Ag, Rh	19, 1	2.6
Pure Pd	-	1.0

2.3. Support Characteristics for the Synthesis of Composite Pd and Pd/Alloy Membranes

According to IUPAC, 2005 terminology index, a composite membrane is defined as the membrane having chemically or structurally distinct layers. For hydrogen separation applications, a composite membrane constitutes a dense and hydrogen selective metal layer (i.e., Pd and/or Pd/alloys) supported on a porous substrate. Depending on the choice of application and process conditions, the synthesis of Pd and Pd/alloy layers have been carried out over a wide range of support materials including, porous glass (Uemiya *et al.*, 1991b; Yeung *et al.*, 1995), ceramics (Uemiya *et al.*, 1991a; Collins and Way, 1993; Kikuchi, 1995; Zhao *et al.*, 1998; Li *et al.*, 1999; Li *et al.*, 2000; Zhao *et al.*, 2000; Cheng *et al.*, 2002; Hou and Hughes, 2002; Roa *et al.*, 2002; Hou and Hughes, 2003; Huang *et al.*, 2003; Roa *et al.*, 2003), porous sintered metals (Shu *et al.*, 1994; Jeema *et al.*, 1996; Li, 1998; Mardilovich *et al.*, 1998a; Jarosch and de Lasa, 1999; Ma *et al.*, 2000; Nam and Lee, 2001; She *et al.*, 2001; Mardilovich *et al.*, 2002; Ma *et al.*, 2004a; Rothenberger *et al.*, 2004; Tong and Matsumura, 2004; Tong *et al.*, 2004b; Wang *et al.*, 2004; Tong *et al.*, 2005a; Tong *et al.*, 2005d; Tong *et al.*, 2005e; Yepes *et al.*, 2006), Tantalum (Peachey *et al.*, 1996; Rothenberger *et al.*, 2003), Vanadium (Edlund and McCarthy, 1995), V-15Ni (Ozaki *et al.*, 2003), nickel and brass (Hasler and Allmendinger, 1993), ceramic hollow fibers (Pan *et al.*, 2003; Tong *et al.*, 2006b).

Among various types of porous substrates, ceramics (i.e., Al_2O_3, TiO_2, SiO_2) and sintered metals (i.e., porous stainless steel 316L (PSS), Hastelloy (PHST), Inconel) are the most commonly studied support materials for the synthesis of composite Pd and Pd/alloy membranes. Ceramic supports are usually attractive due to their high temperature resistivity, small pore size and narrow pore size distribution, which are of great importance for the formation of thin and uniform membrane layers. However, ceramic supports are disadvantageous due to their fragility and difficulty in handling, sealing at high temperatures and integration into reactor modules with various metal parts and more importantly, the mismatch of the coefficient of thermal expansion between the metal membrane layers (i.e., α_{Pd} $[K^{-1}] = 1.20\text{x}10^{-5}$ and α_{Ag} $[K^{-1}] = 1.95\text{x}10^{-5}$) and the ceramic support (i.e., $\alpha_{Alumina}$ [K^{-1}] = $0.65x10^{-5}$). A detailed list of coefficients of thermal expansion for various metals is given in Table 2-2.

Table 2-2. Coefficients of thermal expansion for various metals[†]

Metal	Coefficient of Thermal Expansion $\alpha=(L- L_0)/L_0$, K^{-1} at 20°C
316L Stainless Steel	$1.73x10^{-5}$
Hastelloy-c22	$1.24x10^{-5}$
Inconel-625	$1.31\ x10^{-5}$
Palladium, Pd	$1.17x10^{-5}$
	$1.28x10^{-5}$ (*)
Silver, Ag	$1.95x10^{-5}$
$Pd_{90}Ag_{10}$	$1.20x10^{-5}$
	$1.36x10^{-5}$ (*)
$Pd_{80}Ag_{20}$	$1.28x10^{-5}$
	$1.43x10^{-5}$ (*)
$Pd_{50}Ag_{50}$	$1.54x10^{-5}$
	$1.68x10^{-5}$ (*)
Copper, Cu	$1.70x10^{-5}$
Iron, Fe	$1.20x10^{-5}$
Nickel, Ni	$1.30x10^{-5}$
Chromium, Cr	$0.41x10^{-5}$
ZrO_2	$1.0x10^{-5}$
Alumina Ceramics	$0.65x10^{-5}$

(*) at 500°C

The mismatch of the coefficients of thermal expansion is an important factor affecting the long-term stability of the composite Pd and Pd/alloy ceramic membranes. Many researchers have reported that the hydrogen selective Pd and Pd/alloy films have suffered from either cracking or peeling off the substrate surface during thermal cycling and/or hydrogen loading/un-loading (Tosti *et al.*, 2002).

On the other hand, similar thermal expansion coefficients between the membrane metals (i.e., Pd, Ag and Cu) and the porous sintered metal supports (i.e., $\alpha_{PSS\text{-}316L}$ [K^{-1}] = $1.73x10^{-5}$ and $\alpha_{Hastelloy}$ [K^{-1}] = $1.20x10^{-5}$ also given in Table 2-2), provide better mechanical stability. Therefore, Pd and Pd/Alloy membranes supported on porous sintered metal supports (i.e., PSS-316L, Hastelloy, Inconel) are well-suited for the high purity hydrogen production in steam reforming reactors, as well as in hydrogen purification. In particular, PSS supports are promising candidates due to their various

---

[†] www.hightempmetals.com

advantages such as: good mechanical strength, less fragility and resistantance to cracking, operation at high pressures and temperatures, and industry's familiarity with the stainless steel material results in ease of module fabrication, maintenance and repair. Pd/PSS and/or Pd/Alloy/PSS composite membranes, welded from both ends with non-porous stainless steel tubes, can therefore be assembled and integrated into a process stream very easily.

The performance of the composite Pd and Pd/alloy membranes is strongly depended upon the properties of the support. In particular, three key parameters, namely, porosity, pore size distribution and the type and the chemical composition of the support are of great importance.

2.3.1. Porosity, Pore Size Distribution and Surface Modification of the Macroporous Supports

The porosity of the support determines the effective area for hydrogen permeation and it is desired to have supports with high porosity in order to achieve high hydrogen flux. On the other hand, the pore size distribution, specifically the maximum pore size on the surface of the porous support, has a strong influence on the thickness of the deposited film.

As reported by Ma *et al.* (2001), minimum Pd thickness required to form a dense layer is approximately three times the largest pore diameter present on the support surface. Figure 2-5 shows the pore size distribution data obtained by the mercury intrusion analysis (Mardilovich *et al.*, 2002).

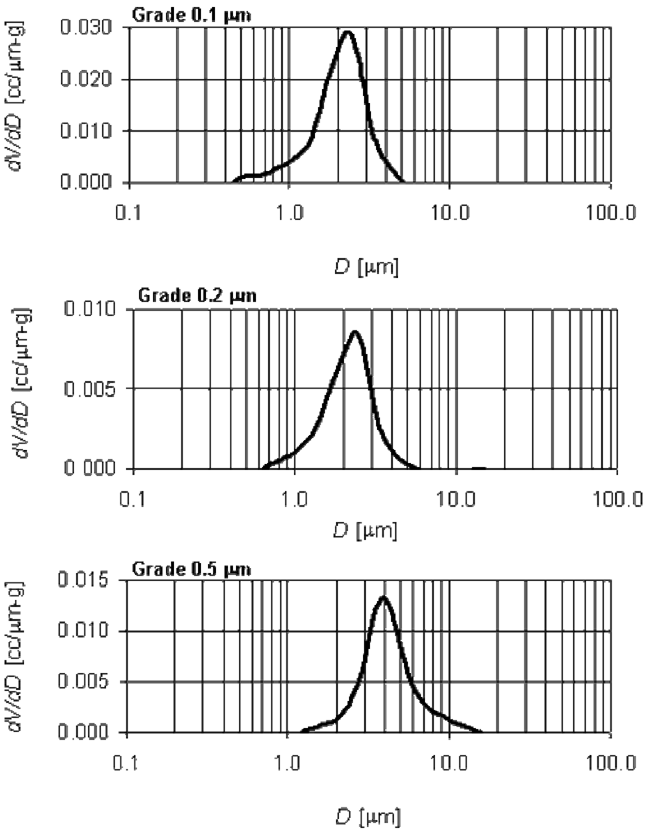

Figure 2-5: Pore size distribution for 0.1, 0.2 and 0.5 µm grade PSS supports (Mardilovich et al.*, 2002)*

According to Mardilovich *et al.* (2002), the maximum pore size for the nominal 0.1, 0.2 and 0.5 µm grade PSS supports, shown in Figure 2-5, ranges between ~4-5 µm, ~6-7 µm and ~11-12 µm, respectively. They have also reported that the dense Pd layers on 0.1, 0.2 and 0.5 µm grade PSS supports were achieved at a gravimetrically estimated thickness of 11.7 µm, 18.1 µm and 33.8 µm, respectively. The actual Pd layer thickness ranges for each support were in good agreement with the predictions made by the previous work of Ma *et al.* (2001).

A porous support characterized with a larger average pore size and a broader pore size distribution would ultimately result in the formation of a thicker layer of Pd and Pd/alloy film. Thick layers of Pd and Pd/alloy film would eventually lead to a lower hydrogen permeance and higher manufacturing cost. In order to narrow the pore size distribution and to eliminate the largest pore on the surface of the porous supports, the modification of the substrate surface, which resulted in the formation of an asymmetric support, has been widely practiced by numerous researchers.

In the case of ceramic supports, thin top layers were obtained by a sol-gel derived γ-Al_2O_3 layer on top of a α-Al_2O_3 substrate (Jayaraman and Lin, 1995; Jun and Lee, 2000; Zhao *et al.*, 2000). Zirconia coating also resulted in the formation of asymmetric ceramic (ZrO_2/α-Al_2O_3) supports with an average pore size range of 5-50 nm (Roa *et al.*, 2002; Roa and Way, 2003a; Roa and Way, 2003b; Roa *et al.*, 2003). In order to eliminate the macro- and meso-pores of the α–alumina substrate, So *et al.* (1998) have first used an *in-situ* silica sol-gel method, followed by a silica sol-dip coating technique to further decrease the pore size of the modified support. However, the thickness of the deposit formed by the soaking and vapor deposition (SVD) method on SiO_2/Alumina supports was as high as 100µm (So *et al.*, 1998).

Surface modification has been a greater challenge in the case of macroporous supports. Early works on the surface modification of porous sintered metal supports have included the use of mechanical methods such as, the shot peening of the 0.5 µm media grade PSS surface via Fe particles (100 µm in diameter) by Jeema *et al.* (1996) and the use of a metallic brush to smoothen the surface roughness of the nominal 0.5 µm media grade PSS substrate by She (2000). For a 6 µm thick Pd film formed by the electroless deposition on a nominal 0.5 µm media grade PSS support modified by the shot peening of Fe particles, Jeema *et al.* (1996) have reported a hydrogen permeance of 11.3 m^3/m^2-h-$atm^{0.5}$ at 400°C.

Surface modification of the PSS supports have also been carried out by the use of submicron Ni powder, which was sintered for 5 hours under high vacuum at 800°C (Nam *et al.*, 1999; Jun and Lee, 2000; Nam and Lee, 2000, 2001). A Cu layer was occasionally electrodeposited on the modified Ni-PSS substrates in order to improve the smoothness and the adhesion of the surface prior to formation of the Pd and Pd/alloy layer. Pd and Pd/alloy layers formed on the modified Ni-PSS supports were as thin as 0.8 µm for a Pd/Ni alloy (22% Ni) (Nam *et al.*, 1999), ~2 µm for a Pd/Ni alloy (20-30% Ni) (Nam and Lee, 2000), 1 µm for a Pd layer (Jun and Lee, 2000) and 2 µm for a Pd/Cu alloy (37 %

Cu) (Nam and Lee, 2001) with hydrogen permeance and H_2/N_2 selectivity[‡] as high as , 155.9 m^3/m^2-h-atm at 550°C (~4500), 54.7 m^3/m^2-h-atm at 450°C (3000), 136.8 m^3/m^2-h-atm 450°C (1600) and 68.4 m^3/m^2-h-atm at 450°C (70000), respectively.

Wang *et al.* (2004) have used ZrO_2 particles to modify the surface of the PSS support. ZrO_2 particles were deposited by vacuum suction from a colloidal ZrO_2 solution in an ultrasonic bath at room temperature. The pH of the colloidal ZrO_2 solution, thus the ZrO_2 particle size, was controlled by the addition of ammonia. Excess ZrO_2 particles on the surface of the PSS support were removed by rinsing water prior to heat treatment at 300°C for 2 hours. The procedure has been repeated several times by varying the pH of the colloidal ZrO_2 solution until all the small pores on the surface of the PSS support have been effectively covered. The thickness of the Pd layer formed on a PSS support modified with ZrO_2 particles was reported as 10 μm with a hydrogen permeance of 14.9 m^3/m^2-h-$atm^{0.5}$ at 500°C and a H_2/Ar selectivity of 140.

Su *et al.* (2005) have used SiO_2 particles to modify the surface of the PSS support. SiO_2 colloid suspensions with different particles sizes (70-100 nm and 20-50 nm) were mixed with ethanol at a weight ratio of 1:5 and coated over the outer surface of the support in a clean room for four consecutive times at a dipping and withdrawal rate of 1 mm/s, followed by a drying at 300°C. At 500°C, Su *et al.* (2005) have reported that the composite Pd/SiO_2-PSS membrane layer with an estimated Pd thickness of 2-3 μm, had an hydrogen permeance of 18.8 m^3/m^2-h-atm and a H_2/N_2 selectivity ranging between 300-450. However, the membrane formed micro-cracks after 10 heating/cooling cycles conducted between room temperature and 500°C under nitrogen atmosphere. For a 5-6 μm thick Pd/SiO_2-PSS membrane, Su *et al.* (2005) have measured a hydrogen permeance of 21.2 m^3/m^2-h-atm at 500°C with a H_2/N_2 selectivity of 300 , which was stable up to 28 heating/cooling cycles.

Furthermore, Tong *et al.* (2004b) have used CeO_2 particles to modify the PSS surface by applying vacuum suction to the suspension of cerium hydroxide through the porous tube for 3 hours at room temperature. For an 8 μm thick composite Pd/CeO_2-PSS membrane, they have reported a hydrogen permeance of 38.6 m^3/m^2-h-$atm^{0.5}$ at 500°C

[‡] Shown in parenthesis

with H_2/Ar selectivity of 800. Similarly, for a 13 μm thick composite Pd/CeO_2-PSS membrane, Tong *et al.* (2005c) have reported a hydrogen permeance of 27.5 m^3/m^2-h-$atm^{0.5}$ at 500°C with an infinite H_2/N_2 selectivity.

Tong and Matsumura (2004) have applied the $Al(OH)_3$ gel to modify the big surface pores of the PSS support. Aluminum hydroxide sol of controlled particle size, which was prepared from aluminum nitrate and ammonium carbonate, was applied by the combination of vacuum suction and mixing in an ultrasonic bath until the water flux through the tube was measured as zero under a pressure difference of 1 atm. The Pd layer formed by the $Al(OH)_3$ grading of the PSS substrate was as thin as 6 μm and had a hydrogen permeance of 21.2 m^3/m^2-h-atm and an infinite selectivity at 500°C (Tong and Matsumura, 2004; Tong *et al.*, 2005b; Tong *et al.*, 2005e). Similarly for a 6 μm thick composite Pd/$Al(OH)_3$-PSS, Tong *et al.* (2005e) have reported a hydrogen permeance of 26.1 m^3/m^2-h-atm and an infinite selectivity at 500°C, which was measured over a period of 260 hours including 40 cycles between hydrogen and argon atmospheres. The surface modification of the porous metal tubes with $Al(OH)_3$ was essentially preferred over ZrO_2, SiO_2, CeO_2 particles since the $Al(OH)_3$ gel provided less mass transfer resistance due to its low residual volume at high temperatures (Tong *et al.*, 2005e).

Furthermore, Tong *et al.* (2005d) have modified a nominal 0.5 μm media grade PSS substrate by sintering short stainless steel fibers (2-3 μm in diameter) prior to pore filling with $Al(OH)_3$ gel. By the use of the modified PSS support, Tong *et al.* (2005d) have achieved a dense Pd layer as thin as 3 μm. At 500°C, the composite Pd/$Al(OH)_3$-PSS membrane had a hydrogen permeance of 29.8 m^3/m^2-h-atm and reported an infinite selectivity. However, the long-term testing of the 3 μm thick membranes consisted of only 70 hours. Further application of the use of γ-Al_2O_3, ZrO_2, SiO_2 or CeO_2 particles for the modification of the porous substrate surface as the pore-filler material have also been reported by Tong and Matsumura (2005), Hou *et al.* (2005), and Tong *et al.* (2006a).

Ma and Guazzone (2006) have achieved gas tight Pd layers as thin as 5.6 μm, by using several layers of pre-activated alumina particles of different sizes (coarse, fine and ultra-fine) for the gradual smoothing of the PSS support surface. Composite Pd membranes prepared on graded supports showed H_2 permeance as high as 50 m^3/m^2-h-

$atm^{0.5}$ at 500°C and ideal selectivities (H_2/He) as high as 27000 that were stable over 1100 hr (Guazzone, 2005).

The synthesis of composite Pd/Ag membranes on porous sintered metal supports have been carried out by the use of surface modification techniques reported by Tong and Matsumura (2004) and Guazzone (2005) and will be discussed in Chapter 6 in greater detail.

2.3.2. Intermetallic Diffusion Barriers

The effective long-term stability of Pd and Pd/alloy membranes is strongly dependent upon the chemical composition of the support. Unlike ceramic and/or porous glass substrates, the utilization of the porous sintered metal tubes for high temperature applications (≥ 500°C) may be limited by the intermetallic diffusion of support metals (Fe, Cr and Ni) into the dense Pd and Pd/alloy separation layer, which ultimately causes the deterioration of the hydrogen permeation flux. The rate of diffusion of the support metals is greatest when the substrate is at or above its “Tamman” temperature. A metal lattice at its Tamman temperature is subjected to considerable thermal (atomic) vibration (Mardilovich *et al.*, 1998a). If there is an interface between two metals, such thermal vibration significantly increases the mobility of the metal atoms and consequently, their capability for diffusion. The Tamman temperature of a material is equal to one-half of its melting temperature (in Kelvin) as given by the following semi-empirical relation in Equation (2-1).

$$T_{Tamman} = \frac{1}{2} T_{melting} (K) \tag{2-1}$$

Melting point and Tamman temperatures for the porous sintered supports and Pd/alloy metals are listed in Table 2-3.

Table 2-3. Thermal and physical properties of porous sintered supports and Pd/Alloy metals

Element	Melting Temperature		Tamman Temperature		Density $[g/cm^3]$
	[K]	[°C]	[K]	[°C]	
Pd	1828	1555	914	641	12.0
Ag	1235	962	618	344	10.5
Cu	1358	1085	679	406	8.92
Au	1337	1064	669	396	19.3
Fe	1811	1538	906	633	7.87
Ni	1728	1455	864	591	8.91
Cr	2180	1907	1090	817	7.14
Mo	2896	2623	1448	1175	10.3
W	3695	3422	1848	1575	19.3
Rh	2237	1964	1119	846	12.5
Ir	2739	2466	1370	1097	22.7
Ru	2607	2334	1304	1031	12.4
Pt	2041	1768	1021	748	21.1
Al	934	661	467	194	2.7

For instance, palladium and stainless steel (316L) with melting points of 1552°C (1825 K) and 1375-1400°C (1648-1673 K) have the corresponding Tamman temperatures are about 640°C (913 K) and 550-560°C (823-833 K), respectively. The lowest Tamman temperature of the metal-metal pair determines the temperature where a significant increase in intermetallic diffusion occurs. Accordingly, at temperatures around 550°C, considerable thermal vibration and diffusion of stainless steel components into the palladium is expected. The undesired alloys formed by the diffusion of porous sintered metal components into the dense and hydrogen selective Pd and Pd/alloy layer will have a reduced hydrogen permeability due to the shrinkage of the Pd lattice and associated decrease in hydrogen solubility and diffusivity (Flanagan *et al.*, 1977; Gryaznov *et al.*, 1993; Jun and Lee, 2000; Bryden and Ying, 2002). The microstructure analysis of the intermetallic diffusion induced alloy phases and their effects on hydrogen permeation flux for the Pd/Ag membranes supported on porous sintered metal supports will be discussed in greater detail in Chapter 7.

In order to prevent the intermetallic diffusion, different approaches based on generating an additional oxide layer between the metal support and Pd and/or Pd/alloy layer, have been studied by various researchers. Gryaznov *et al.* (1993) have reported that the application of an intermediate high temperature melting metal (i.e. Tungsten with a Tamman temperature of 1570°C) or an oxide layer such as tantalum oxide has increased the life of membranes. Gryaznov *et al.* (1993) have modified a porous stainless steel sheet with a 0.8 μm thick intermediate tungsten layer as the intermetallic diffusion barrier and reported a stable hydrogen flux of 120 m^3/m^2-h at a trans-membrane pressure difference of 20 atm for a 10 μm thick Pd/Ru alloy (6% Ru), which was tested at 800°C over a period of 1000 hours.

Edlund and McCarthy (1995) have reported the existence of a significant intermetallic diffusion and a rapid flux decline for a 25 μm thick Pd foil coated on a vanadium support at 700°C. They have suggested the use of an intermediate layer of 250 μm thick porous aluminum oxide as a metal-diffusion barrier between the 25 μm thick Pd foil and the vanadium support and reported an improved stability over a period of 80 hours at 700°C. Shu *et al.* (1996) have also suggested the use of a diffusion barrier layer between the ~16 μm thick Pd/Ag alloy (26% Ag) film and the PSS substrate, which consisted of an ultrathin (0.1 μm) intermediate layer of titanium nitride (TiN). Auger electron depth analysis have revealed that the TiN diffusion barrier was effective to prevent Fe segregation into the Pd/Ag alloy layer and led to the formation of a thermally stable membrane at an operating temperature as high as 700°C.

Nam and Lee (2001) have applied sol-gel techniques to form a colloidal silica sol layer, which was used as an intermetallic diffusion barrier between a 2 μm thick Pd/Cu layer (37 % Cu) and the PSS support modified with a submicron Ni powder. Nam and Lee (2001) have reported a hydrogen permeance of 68.4 m^3/m^2-h-atm at 450°C with a H_2/N_2 selectivity as high as 70000. However, there were no data on the long-term stability of the composite Pd-Cu/Silica/Ni-PSS membrane. In a subsequent paper, Lee *et al.* (2003) have reported that the composite Pd/Silica/Ni-PSS membranes prepared according to the methodology given by Nam and Lee (2001) have resulted in the formation of extensive pinholes and cracks during the long-term testing (7-30 days) under mixed gas atmosphere (99% H_2 and 1% N_2) at 450°C. More recently, for a submicron thick Pd membrane prepared on a PSS substrate coated with a TiN layer, Nam and Lee

(2005) have reported a stable hydrogen permeance of 52 m^3/m^2-h-$atm^{0.5}$ with a H_2/N_2 selectivity as high as 4600 tested over a period of 40 days.

Yepes *et al.* (2006) have modified the PSS surface by wash-coating with a thin layer of γ-Al_2O_3. According to the to Auger and EPMA depth profiles from Pd/Ag layers annealed at 650°C, they have reported that the γ-Al_2O_3 have served as an effective barrier against the intermetallic diffusion.

In order to address the problem of structural stability of electrolessly plated Pd/PSS and/or Pd/Alloy/PSS membranes, Ma *et al.* (2000) have introduced an oxide-layer diffusion barrier by controlled *in-situ* oxidation of the porous stainless steel supports prior to Pd and/or Pd/Ag metal deposition. Mardilovich *et al.* (1998a) have reported that the membranes prepared on oxidized supports were stable at 350°C over a period of 1100 hours with no significant changes in the steady-state hydrogen flux. Indeed, several other membranes prepared on porous sintered metal supports with an intermetallic diffusion layer formed by the *in-situ* oxidation method have been shown to be stable for over 6,000 hours in the temperature range of 350-450°C (Mardilovich *et al.*, 1998a; Mardilovich *et al.*, 1998b). Akis *et al.* (2003) have studied the effect of oxidation temperature on the properties of the nominal 0.5 μm grade PSS supports by monitoring the He flux for the support at various temperatures, weight gain from the oxide layer and the changes in the mean pore diameter of the support using Hg porosimetry. They have found that the weight gains of the samples increased with the oxidation temperature indicating the formation of a thicker oxide layer at higher temperatures. In addition they have also reported that the oxidation had little effect on the mean pore size, indicating that oxidation did not constrict the internal pore system even at 800°C. Engwall *et al.* (2003) have carried out an experimental study to determine the contribution to the transport resistance of the supports with oxide diffusion barriers using a simple model based on the Darcy's law. They have reported that the oxidation temperature of 600°C resulted in a 40% reduction of the room temperature helium permeability of the support indicating a partial blockage of the pore system. They also reported that the contribution of the support to the total membrane pressure drop was only 1.9%, revealing that even high oxidation temperatures would not cause a significant increase in support resistance relative to the total resistance of the membrane and would not impact the membrane performance. The mass transfer resistance exerted by the support and its effect on hydrogen permeance is further discussed in Chapter 4. Ma *et al.* (2004a) have shown by the use of EDX line scan analysis that the intermetallic diffusion between the substrate metals and Pd layer has been minimized with the presence of the oxide barrier layer. Recently, Guazzone *et al.* (2004) studied the relation between the hydrogen permeation data and the oxide layers formed at various temperatures on PSS supports. The hydrogen permeation data reported by them showed that the oxide layers formed at temperatures equal or higher than 500°C was effective in terms of preventing the adverse effects of intermetallic diffusion on hydrogen permeance. Membranes deposited on oxide layers formed at 500°C or above were stable for about 100 hours at 500°C. They also showed that the structure of the oxide layer formed at 600°C in air (with an iron oxide rich layer on top of a chromium oxide layer) was similar to the structure of the oxide formed at 800°C as reported by Ma *et al.* (2004a).

Tong *et al.* (2005d) have reported that a 0.3 μm thick electroplated Ag on a PSS support functioned as a diffusion barrier upon a relatively short period (70 hours) of hydrogen permeation test conducted at 500°C. A comprehensive discussion on the long-term thermal stability of the pure-Ag layer as an effective intermetallic diffusion barrier is given in Chapters 7 and 8.

Ma *et al.* (2004b) have developed a method to produce a porous Pd/Ag intermetallic diffusion barrier layer on the surface of the support by the bi-metal multi-layer (BMML) deposition technique prior to the application of the dense hydrogen selective layer. The unique morphology of the porous Pd/Ag barrier formed an extremely effective layer against intermetallic diffusion, which was stable at temperatures 500°C and above for several hundreds of hours as reported by Ayturk *et al.* (2004b; 2006). Furthermore, the stability of the Pd/Ag barrier layer against the intermetallic diffusion was clearly demonstrated by Mardilovich *et al.* (2006) for a BMML membrane with a 7.9 μm thick hydrogen selective layer and a permeable surface area of 114.5 cm^2. An extended life test over a period of 1388 hours, showed a hydrogen permeance of 68.5 m^3/m^2-h-$atm^{0.5}$ at 500°C with no evidence of the intermetallic diffusion of the support metals into the 7.9

μm thick gas selective layer. A detailed discussion on the microstructure resulting from the bi-metal multi-layer (BMML) deposition of Pd/Ag layers on PSS supports and their effectiveness as a barrier layer for intermetallic diffusion is given in Chapter 5.

2.4. Methods for the Synthesis of Composite Pd and Pd/Alloy Membranes

Traditionally, Pd-based membranes made of thin-walled tubes or free standing foils were formed by arc-melting and cold-rolling techniques (Graham, 1869a, 1869b; Knapton, 1977; Gryaznov, 2000). Composite Pd ad Pd/alloy membranes were also prepared by diffusion welding and/or cold rolling of thick Pd and Pd/Ag foils onto porous ceramic and porous stainless steel supports (Tosti *et al.*, 2000; Tosti *et al.*, 2002; Tosti, 2003; Tosti *et al.*, 2003a; Tosti *et al.*, 2003b). More recently, micro-fabrication techniques were used to form sub-micron thick Pd/Ag alloy layers to be integrated in small scale membrane reactor modules and purification units (Keurentjes *et al.*, 2004; Tong *et al.*, 2004a). Nonetheless, thin layers of Pd and Pd/alloy layers (< 20 μm) can be prepared on porous substrates by the use of several different film deposition techniques. In this respect, the most commonly applied methods for the synthesis of composite Pd and Pd/alloy membranes include electroplating, magnetron sputtering, e-beam evaporation, chemical vapor deposition, spray pyrolysis, and electroless plating.

2.4.1. Electroplating

Electroplating is conducted in an electrolyte solution, which is a specially designed chemical plating bath that has the desired metal (i.e. silver, gold) dissolved as microscopic particles (positive charged ions) suspended in the solution (Kirk-Othmer, 2004). The object that is to be plated is submerged into the plating bath, generally located at the center of the plating medium, acts as a negatively charged cathode. The positively charged anodes that will complete the DC circuit are carefully positioned at the edges of the plating tank and a low voltage DC current is applied to the bath, where the plating bath solution serves as a conductive medium. A power source known as a rectifier is used to convert AC power to a carefully regulated low voltage DC current. The resulting circuit channels the electrons into a path from the rectifier to the cathode (object being plated), through the plating bath to the anode (positively charged) and back to the rectifier. Since electrical current flows from positive to negative, the positively charged ions at the anodes flow through the plating bath's metal electrolyte toward the negatively charged cathode. This movement causes the metal ions in the bath to migrate toward the extra electrons located at the outer layer of the cathode surface. By means of electrolysis, the metal ions are taken out of solution and are deposited as a thin layer on the surface of the object, which is called electrodeposition. Electroplating process is widely used and preferred for applications involving decorative finishes. The metals typically used by the jewelry and decorative metals industry (i.e. auto parts) for electroplating are gold, silver, nickel, palladium, platinum, ruthenium and rhodium. For engineering finishes, the most commonly plated metals are brass, cadmium, stainless steel, copper, gold, nickel, silver, tin, and zinc. Moreover, electroplating has also been widely used for the deposition of Pd and Pd/alloy layers on porous substrates.

Hasler and Allmendinger (1993) have studied the electrodeposition of Pd/Ag films on copper, brass ($Cu_{63}Zn_{37}$) and nickel foils at 25°C using a two-compartment cell separated by an anion exchange membrane. They carried out the experiments over a working potential range of -200 mV to +800 mV. At a working potential range between 0 and 50 mV and even in the absence of a brightener sodium benzaldehyde-2,4-disulphonate (BDS) used to improve the quality of the deposits, they have reported that 1.2 μm thick Pd/Ag films were pinhole free and in the form of bright deposits. They have also noted that the use of negative potentials (i.e., -100 mV) resulted in hydrogen evolution during plating, which ultimately lead to the formation of black and powdery deposits.

Nam *et al.* (1999) have used the vacuum electrodeposition technique to prepare Pd/Ni alloy membranes on porous stainless steel disks. PSS supports have been modified with submicron Ni powder and a CuCN solution to improve the surface smoothness and adhesion. The membranes were characterized over a temperature and pressure range of 350°C-550°C and 0.1-0.7 atm, respectively. For a 0.8 μm thick Pd/Ni layer (22% Ni), Nam *et al.* (1999) have reported a hydrogen permeance of 155.9 m^3/m^2-h-atm at 550°C with a H_2/N_2 selectivity of ~4500. For a ~2 μm thick Pd/Ni layer (20-30 % Ni) formed by the vacuum electrodeposition on a modified PSS support, Nam and Lee (2000) have reported a hydrogen permeance of 54.7 m^3/m^2-h-atm at 450°C with a H_2/N_2 selectivity of 3000. Furthermore, for a 2 μm thick Pd/Cu layer (37 % Cu) deposited on a modified PSS support with an additional silica sol-gel layer as the intermetallic diffusion barrier, Nam and Lee (2001) have reported a hydrogen permeance of 68.4 m^3/m^2-h-atm at 450°C with a H_2/N_2 selectivity as high as 70000. However, there were no data on the long-term stability of the composite Pd/Ag/Ni-PSS, Pd/Ni/Ni-PSS and Pd/Cu/Silica/Ni-PSS membranes reported by the authors. More recently, Lee *et al.* (2003) have reported that the composite Pd/Silica/Ni-PSS membranes prepared according to the methodology proposed by Nam and Lee (2001) have resulted in the formation of extensive pinholes and cracks during the long-term testing (7-30 days) under mixed gas atmosphere (99% H_2 and 1% N_2) at 450°C. The failure of the composite Pd/Silica/Ni-PSS membranes were attributed to the formation of reducible metal oxides between the membrane layers such as nickel, iron and palladium oxides (Lee *et al.*, 2003).

2.4.2. Magnetron Sputtering

Sputtering is a vacuum process used to deposit very thin films on various substrates by applying a high voltage (typically -300V or more) across a low-pressure gas (usually argon at about 5 millitorr) to generate a plasma, consisting of electrons and gas ions in a high-energy state (Kirk-Othmer, 2004). During sputtering, energized plasma ions strike the target (composed of the desired coating material), at high speeds and cause atoms from the target to be ejected with enough energy to travel to, and bond with, the substrate. The collision at the surface leads to two important processes. First, atoms are knocked out of the target surface with mean kinetic energies of 4 to 6 eV, which is called sputtering. These sputtered atoms, which are neutrally charged, collide with the substrates to be coated and form an extremely adherent coating by building a virtually unbreakable bond between the film and its substrate, since the bonding between the neutrally charged sputter atoms and the substrate atom takes place at the molecular level. Generally, the formation of uniform coatings is a four stage process, consisting of nucleation, island growth, coalescence and finally continuous growth.

Although the sputtering process has long been studied, controlling the flow direction of atoms in the process is still problematic and makes sputtering impractical for mass production and large-scale industrial applications. On the other hand, improvements achieved by the utilization of powerful magnets which lead to the development of “magnetron sputtering”, which also suffers in regards to economical feasibility. However, magnetron sputtering technique has been used for the synthesis of Pd and Pd/alloy membranes.

Gryaznov *et al.* (1993) have used the magnetron sputtering for the deposition of Pd and Pd/alloys (Mn, Co, Ru, Sn) on asymmetric polymer membranes, porous metal sheets and oxide plates. At 800°C and a trans-membrane pressure difference of 20 atm, Gryaznov *et al.* (1993) have reported a stable hydrogen flux of 120 m^3/m^2-h over a testing period of 1000 hours for a 10 μm thick Pd/Ru alloy (6% Ru) sputtered on a porous stainless steel sheet, which was modified with an intermediate tungsten layer (0.8 μm thick) as the intermetallic diffusion barrier. Same composite sputtered on a porous oxide plate made of magnesia and 15% yttria had a stable hydrogen flux of 108 m^3/m^2-h at 700°C and a trans-membrane pressure difference of 10 atm after 1000 hours.

Jayaraman and Lin (1995) have used the RF magnetron sputtering technique for the synthesis of ultra-thin (200-500 nm) Pd/Ag alloy layers (25% Ag) on α-alumina supports modified with a γ-alumina sol-gel layer. The hydrogen permeance for the composite Pd/Ag/Ceramic membrane at 250^{o}C was reported as 2.9-5.5 m^3/m^2-h-atm with an extremely low H_2/N_2 separation factor of only 5.7. O’Brien *et al.* (2001) have also studied the deposition of Pd/Ag alloy (23% Ag) layers on porous α- and γ- alumina substrates using RF magnetron sputtering over a wide experimental range of parameters to determine the structure, pinhole density, composition, N_2 gas-tightness and H_2 permeability of the coatings. However, all the samples studied by O’Brien *et al.* (2001) were found to contain pinholes and resulted in very poor H_2/N_2 selectivity between 4 and slightly above 80. The imperfections and defects on the deposited films were due to the difficulty in optimizing the sputter deposition conditions and the initial condition of the substrate surface.

Moss *et al.* (1998) have reported a stable hydrogen permeation rate of 86.8 m^3/m^2-h-$atm^{0.5}$ measured over a period of 775 hours at 300°C for a 0.5 μm thick Pd film formed by the sputter deposition on both sides of a 40 μm thick vanadium foil, which was ionmilled prior to the Pd deposition. Under the same testing conditions at 300°C, Moss *et al.* (1998) have measured a hydrogen permeance of 4.96 m^3/m^2-h-$atm^{0.5}$ for a 40 μm thick sheet of pure Pd foil.

Zhao *et al.* (1999) have also applied the magnetron sputtering technique to prepare 1 μm thick Pd/Ag alloy (24% Ag) on a γ-Al_2O_3 substrate. Although the composite Pd/Ag/ γ-Al_2O_3 membrane had a hydrogen permeance of 42.7 m^3/m^2-h-$atm^{0.5}$ at 411°C with a H_2/N_2 selectivity of 1000, Zhao *et al.* (1999) have reported the loss of hydrogen permselectivity at 462°C due to the formation of hillocks and microcracks in the 1 μm thick Pd/Ag alloy (24% Ag) film.

The difficulty in controlling the experimental parameters of the sputtering technique has been studied by Thomann *et al.* (2000). According to them, the conventional sputtering techniques, which have a lower energy around 12 eV, resulted in no significant film growth. They have suggested increasing the energetic species flux to metal atom flux ratio and accelerate the coalescence process, which might result in more compact and packed aggregates due to the increased mobility of metal atoms under bombardment.

McCool *et al.* (1999) have used the sputter deposition to form submicron thick Pd/Ag alloy films (5-18% Ag) on γ-alumina substrates. At 300°C, the Pd/Ag alloy (18% Ag) film with a thickness of 177 nm had an extremely low hydrogen permeance of 0.6 m^3/m^2-h-atm and a H_2/N_2 selectivity of 3845. McCool *et al.* (1999) have reported that all the other Pd/Ag alloy films formed by sputter deposition on γ-alumina supports suffered from either cracking or peeling away from the substrate surface. On the other hand, Gielens *et al.* (2002) have successfully deposited a 750 nm thick Pd/Ag alloy (23% Ag) layer on a 1 mm thick non-porous silicon nitrile substrate, which was modified to have 5 μm openings after the sputtering. At a feed side hydrogen partial pressure of 0.2 bar, the hydrogen permeation rates reported by Gielens *et al.* (2002) were 1.6 and 76.6 m^3/m^2-h at 350°C and 450°C, respectively, with H_2/He selectivity over 1500. Finally, Rothenberger *et al.* (2003) have studied the hydrogen transport through the tantalum and tantalum coated Pd membranes prepared by the cold-plasma discharge sputtering, over a temperature and hydrogen partial pressure range of 350-900°C and 1-26 atm, respectively. They have observed oxidation, distortion and cracking on the tantalum surface due to the tantalum hydride formation for all the samples tested. Furthermore, a 1.2 μm thick sputter coated pure Pd film was observed to be peeling off of the tantalum surface only after 49 hours of testing at 500°C.

2.4.3. Electron/Ion Beam Evaporation

In the e-beam evaporation technique, the substrate is placed in a high vacuum chamber (10^{-7} Torr) at room temperature with a crucible containing the material to be deposited (Kirk-Othmer, 2004). An electron emitter such as tungsten filament held at a high negative potential, emits electrons in all directions. The cathode assembly together with the beam former and deflection plate, form a beam in a defined direction. The beam of electrons is then accelerated through the steep potential gradient formed between the cathode and anode assembly, where the culminated beam of high energy electrons is injected into a permanent magnetic field. The magnetic field deflects and focuses the beam on the crucible containing the material to be evaporated. The impinging electrons' kinetic energy is transformed into thermal energy at the impact surface of the source charge, which is supported in a water-cooled copper crucible. The overall energy released is quite high, which is usually more than several million watts per square centimeter. However, the e-beam evaporation proved inappropriate for depositing materials such as insulators, and for use with substrates that have a low melting point, such as plastics, since the heat radiated from the source and carried by the atoms of the deposited material was simply too high. In addition to its limited applications, the confined space within the high vacuum chambers makes the e-beam evaporation technique impractical for the synthesis of Pd and Pd/alloy layers on large scale metal supports.

Nevertheless, one specific example of the application of the e-beam evaporation technique has been carried out by Peachey *et al.* (1996) for the synthesis of 1μm thick Pd layer on each sides of a 13 μm thick Ta foil with a surface area of only 2 cm^2. For the 1μm thick Pd layer, they have reported a hydrogen permeance of 11.9 m^3/m^2-h-atm and 17.6 m^3/m^2-h-atm at 300°C and 365°C, respectively.

2.4.4. Chemical Vapor Deposition (CVD)

CVD is a chemical process for depositing thin films of various materials (Kirk-Othmer, 2004). In a typical CVD process the substrate is exposed to one or more volatile precursors that react and/or decompose on the substrate surface to produce the desired deposit in the presence of a gas flow through the reaction chamber, which is used to remove the volatile by-products formed during the reaction. CVD is widely used in the semiconductor industry to deposit various films including: polycrystalline, amorphous, and epitaxial silicon, SiO_2, silicon germanium, tungsten, silicon nitride, silicon oxynitride, titanium nitride, and various high-k dielectrics. A number of different forms of CVD based processes are, metal-organic, plasma-enhanced, rapid-thermal, atmospheric pressure, low pressure, ultra-high vacuum, and atomic layer CVD (Kirk-Othmer, 2004). CVD can give very uniform films even on rough surfaces provided that the process is controlled by surface kinetics. However, the complexity of the technique makes it impractical for large-scale industrial applications.

Jun and Lee (2000) have used the cold-wall metal-organic chemical vapor deposition (MOCVD) method for the synthesis of Pd and Pd/Ni alloy membranes on mesoporous-nickel-stainless steel (Ni-SS) and γ-Al_2O_3/α-Al_2O_3 supports by decomposing $Pd(C_3H_5)(C_5H_5)$ and $Ni(C_3H_5)(C_5H_5)$ into densely aggregated metal crystallites via the layer by layer deposition technique. Jun and Lee (2000) have reported a hydrogen permeance of 136.8 m^3/m^2-h-atm at 450°C for a 1 μm thick Pd/Ni-SS membrane with a H_2/N_2 selectivity of 1600. However, the membrane lost 50% of its initial hydrogen permeance over a period of 160 hours due to the intermetallic diffusion of Ni into the pure Pd layer formed by the CVD method. For a 1 μm thick Pd/Alumina membrane, Jun and Lee (2000) have reported an intial hydrogen permeance of 16.6 m^3/m^2-h-atm at 450°C with H_2/N_2 selectivity of 780. They have also reported that the long-term testing (> 1 week) of the Pd/Alumina membranes failed due to the sealing problems or thermal instability of the membranes. Kikuchi *et al.* (2000) have studied the steam reforming of methane at 500°C using composite membranes prepared by both CVD and electroless plating techniques on alumina tubes. At 500°C, an 8 μm thick Pd membrane formed by the electroless plating have shown a hydrogen permeance of 28.2 m^3/m^2-h-atm (86.4%

methane conversion) and an infinite H_2/N_2 selectivity while the poor performance of the Pd membrane prepared by the CVD technique was poor. Similarly, Kajiwarea *et al.* (2000) have used the CVD technique for the synthesis of rhodium and iridium layers on porous Al_2O_3 supports. At 500°C, the hydrogen permeance for the 17.3 μm thick Rh and 8.3 μm thick Ir membranes were reported as 30.2 m^3/m^2-h-$atm^{0.5}$ and 34.8 m^3/m^2-h-$atm^{0.5}$ with H_2/N_2 selectivities 80 and 93, respectively.

2.4.5. Spray Pyrolysis

Spray pyrolysis, which allows to control the film morphology and powder particle size in the nm range, have been used to deposit metal oxides, chalcogenide and even metal films (Kirk-Othmer, 2004). However, the morphology, texture, crystallinity, and other physical properties of the deposited film are strongly dependent upon the substrate surface temperature, deposition temperature, precursor solution chemistry and the presence of the additives in the precursor solution chemistry (Pluym *et al.*, 1996). Li *et al.* (1993) have prepared a 1.5-2 μm thick Pd/Ag alloy membrane supported on the outer surface of a porous alumina hollow-fiber support by the spray pyrolysis of $Pd(NO_3)_2$ and $AgNO_3$ solutions in H_2-O_2 flame. However, the Pd/Ag alloy layer had only a H_2/N_2 separation factor of 24 at 500°C.

Similar to CVD, the complexity and the difficulty in controlling the experimental parameters of the spray pyrolysis technique limits its applications to the membrane based separation technologies.

Hydrogen permeation characteristics of composite Pd and Pd/alloy membranes formed by the use of vacuum electrodeposition (VED), magnetron sputtering (MS), e-beam evaporation (e-BE), chemical vapor deposition (CVD) and spray pyrolysis (SP) are summarized in Table 2-4.

Table 2-4. Summary of the Pd and Pd/Alloy membranes formed by different methods

Reference	Dep$^{\underline{n}}$ Method[*]	Membrane Layer	Support	Thickness (μm)	Temp. (°C)	H_2 Permeance (m^3/m^2-h-atm^n)	n-value	Selectivity H_2/N_2	Duration (hours)
Nam *et al.* (1999)	VED	Pd/Ni$_{22\%}$	Ni-PSS$_{\text{Disk}}$	0.8	350	16.4	1	500	n/a
		Pd/Ni$_{22\%}$	Ni-PSS$_{\text{Disk}}$	0.8	450	41.0	1	1000	n/a
		Pd/Ni$_{22\%}$	Ni-PSS$_{\text{Disk}}$	0.8	550	155.9	1	4500	n/a
Nam and Lee (2000)	VED	Pd/Ni$_{20\text{-}30\%}$	Ni-PSS$_{\text{Disk}}$	2.0	450	54.7	1	3000	n/a
Nam and Lee (2001)	VED	Pd/Cu$_{37\%}$	Silica/Ni-PSS$_{\text{Disk}}$	2	450	68.4	1	70000	n/a
Nam and Lee (2005)	VED	Pd/Ni$_{18\%}$	TiN/Ni-PSS$_{\text{Disk}}$	3	450	26.0	1	4600	1440
Gryaznov *et al.* (1993)[†]	MS	Pd/Ru$_{6\%}$	0.8 μm W/PSS$_{\text{Sheet}}$	10	800	6.0	1	∞	1000
Jayaraman and Lin (1995)	RF[‡] MS	Pd/Ag$_{25\%}$	γ-Al_2O_3-Sol/α-Al_2O_3 $_{\text{Disk}}$	0.350	250	2.90	1	5.7	n/a
		Pd/Ag$_{25\%}$	γ-Al_2O_3-Sol/α-Al_2O_3 $_{\text{Disk}}$	0.350	250	5.50	1	5.7	n/a
Moss *et al.* (1998)	RF MS	Pd	40 μm V foil	0.5	300	86.8	0.5	n/a	775
Zhao *et al.* (1999)	MS	Pd/Ag$_{24\%}$	γ-Al_2O_3	1	411	42.7	1	1000	n/a
McCool *et al.* (1999)	MS	Pd/Ag$_{18\%}$	γ-Al_2O_3	0.18	300	0.60	1	3845	n/a
O'Brien *et al.* (2001)	MS	Pd/Ag$_{23\%}$	γ-Al_2O_3	1	350	0.5	1	4	1
		Pd/Ag$_{23\%}$	α-Al_2O_3	1	350	5.1	1	20	1
Gielens *et al.* (2002)	MS	Pd/Ag$_{23\%}$	Silicon Nitrile	0.75	350	40.6	0.5	1500	n/a
		Pd/Ag$_{23\%}$	Silicon Nitrile	0.75	400	77.1	0.5	1500	n/a
		Pd/Ag$_{23\%}$	Silicon Nitrile	0.75	450	162.3	0.5	1500	n/a
Peachey *et al.* (1996)	e-BE	Pd	13 μm Ta foil	1	300	11.9	1	n/a	n/a
		Pd	13 μm Ta foil	1	365	17.6	1	n/a	n/a
Jun and Lee (2000)	CVD	Pd	Ni-PSS$_{\text{Disk}}$	1	450	141.1	1	1600	160
		Pd	Ni-PSS$_{\text{Disk}}$	1	450	105.8	1	100	160
		Pd	γ-Al_2O_3/α-Al_2O_3 $_{\text{Disk}}$	1	450	16.6	1	780	160
Kajiwara *et al.* (2000)	CVD	Rh	Al_2O_3	17.3	500	30.2	0.5	80	n/a
		Ir	Al_2O_3	8.3	500	34.8	0.5	93	n/a
Uemiya *et al.* (2001)	CVD	Pd	Al_2O_3	3.2	500	25.1	1	240	n/a
	CVD	Pt	Al_2O_3	5.8	500	8.4	1	210	n/a
	CVD	Rh	Al_2O_3	17.3	500	4.6	1	80	n/a
	CVD	Ir	Al_2O_3	8.3	500	9.2	1	93	n/a
	CVD	Ru	Al_2O_3	3.3	500	12.5	1	120	n/a
Kikuchi *et al.* (2000)	CVD	Pd	Al_2O_3	n/a	500	28.2	1	13	n/a
Li *et al.* (1993)	SP	Pd/Ag	Ceramic Hollow Fiber	1.5-2	500	n/a	n/a	24	n/a

---

[*] VED: Vacuum Electro-Deposition, MS: Magnetron Sputtering, e-BE: e-Beam Evaporation, CVD: Chemical Vapor Deposition and SP: Spray Pyrolysis

[†] Hydrogen flux reported as 120 m^3/m^2-h at a trans-membrane pressure difference of 20 atm

[‡] RF: radio frequency

2.4.6. Electroless Plating

Electroless plating is defined as the controlled autocatalytic deposition of a continuous film at a catalytic interface by the reaction in solution of a metal salt and a chemical reducing agent (Mallory and Hajdu, 1990). Since electroless deposition can produce films of metals, alloys, compounds, and composites on both conductive and nonconductive surfaces, key application areas are multilayer and surface mount printed circuit boards, radio frequency interference shielding for computers, corrosion- and wear-resistant metal surfaces, lightweight plated plastics and membrane fabrication processes. The ability to produce metal deposits in controlled patterns makes electroless plating of primary importance to modern electronics technology and many others.

2.4.6.1. Historical Overview

In early 1800s, Wurtz (1844) observed that nickel cations were reduced by hypophosphite anions. However, Wurtz (1844) only obtained a black powder. The first bright metallic deposits of nickel-phosphorus alloys were obtained by Bretau (1911), followed by the first issued patent on an electroless nickel plating bath by Roux (1916). However, these baths decomposed spontaneously and formed deposits on any surface that was in contact with the solution, even the walls of the container. Many other investigators studied the process, but their interest was in the chemical reaction and not the plating process. Following the first patent on commercially usable electroless nickel solutions (Roux, 1916), Brenner and Riddell (1946) published a paper that described the proper conditions for obtaining electroless deposition, which was taken as the beginning of the modern electroless plating. The first large-scale electroless process was the “Kanigen” electroless nickel process from General American Transportation Corp., which used hypophosphite as the reducing agent (Mallory and Hajdu, 1990). This was followed by the introduction of the first electroless nickel solution widely used on plastics in 1966, in which the solution was usable at room temperature and was extremely stable. Interests in electroless plating grew as it was shown that the uniformity of the deposition was very high. The growth of electroless plating and its importance is directly traceable to the followings:

i. Discovery of the possibility to produce metal alloys by electroless deposition

ii. Growth of the electronics industry (especially the development of printed circuits)

iii. Large-scale introduction of plastics into everyday life.

Although the most common electroless plating method is electroless nickel plating, the patent literature contains a large number of commercial electroless metal plating baths and their applications including copper, gold, chrome, rhodium, zinc, tin, palladium, and silver.

For instance, electroless plated copper was introduced in the mid-1950s and is now available commercially in a great variety (Mallory and Hajdu, 1990). Electroless plated gold is commercially used on printed circuit boards, flex circuits, ceramics, three-dimensional circuits, metals, and highly specialized substrates. Rhodium is occasionally used on white gold, silver, copper and its alloys. Chrome plating is a finishing treatment used for the decorative purposes in metal furniture frames and automotive trimming industry or to reduce friction and wear in industrial parts. Zinc coatings are mainly used to prevent oxidation on metal surfaces whereas tin is extensively used to protect ferrous and nonferrous surfaces. Electroless plated palladium is mainly used in specialty applications in the electronics industry where the need for continuous coatings justified the high price. Pd is also widely used in dentistry, watch making, aircraft spark plugs, production of surgical instruments, electrical contacts, jewelry, photography and most importantly in hydrogen purification and separation. On the other hand, silver was the first metal used for metallizing nonconductive surfaces. Most electroless plated silver applications are for silvering glass or metallizing record masters. Mirror production is the principal usage for electroless silver. Silver-plated nylon cloth is used as a bacteriostatic wound dressing, where silver acts as a bactericide. Silver is also used in the jewelry and button industry.

2.4.6.2. Synthesis of Composite Pd and Pd/Alloy Membranes via Electroless Plating Technique

Main advantages of using electroless plating technique for the synthesis of composite Pd and Pd/alloy membranes on porous substrates include the uniform deposition on complex geometries and large surface areas, hardness of the deposited film, good adhesion to the substrate, simple equipment and ease of scale-up (Mardilovich *et al.*, 1998a; Ma *et al.*, 2004a).

A typical bath chemistry for the electroless plating of Pd consists of a metal ion source ($PdCl_2$, $Pd(NH_3)_4Cl_2$, $Pd(NH_3)(NO_3)_2$, $Pd(NH_3)_4Br_2$), a complexing agent (ethylene-di-amine tetra-acetic acid (EDTA), ethylene-di-amine (EDA), NH_4OH), a reducing agent (NH_2NH_2, $NaH_2PO_2.H_2O$, tri-methyl-amine borane), stabilizers and accelerators. Indeed, the metal ion sources for the electroless plating of Ag and Cu metals include $AgNO_3$ and $CuSO_4.5H_2O$, respectively.

$NaH_2PO_2.H_2O$ based plating baths with the use of EDA as the complexant have been frequently used, however, the microstructure of the deposited films were significantly altered with the formation of cracks due to the evolving hydrogen gas during reaction.

Rhoda (1959) was the first to develop the hydrazine based electroless palladium plating bath by using the Pd in the form of tetra-amine di-chloride, $Pd(NH_3)_4Cl_2$. Rhoda (1959) has observed a linear increase in the plating rate with temperature between 40 and 80°C from 3.8 to 14.7 μm/hr and a spontaneous precipitation of the bath above 70°C in the absence of EDTA salt, which was added as a stabilizer. Another observation reported by Rhoda (1959) was the rapid decrease in plating rate with time, which was attributed to catalytic decomposition of hydrazine by palladium. The Pd deposits prepared on rack and barrel samples were reported to be at least 99.4% pure with a density of 11.96 g/cm^3 and an average Knoop hardness of 257, with a range of 150 to 350 at a 25 g load. In addition, good deposits were also obtained on Al, Cr, Co, Au, Fe, Mo, Ni, Pd, Pt, Rh, Ru, Ag, steel, Sn, W, graphite, carbon and properly activated glass and ceramics. However, bath instability was a serious drawback of the original Rhoda (1959) formulation.

Over the years, from Rhoda (1959) onwards, hydrazine based electroless plating baths and plating conditions were well established (Table 3-4) and successfully utilized for the synthesis of dense and hydrogen selective Pd and Pd/alloy layers on various substrates as discussed previously in Section 2.3.

However, there are only few studies in the literature regarding the electroless plating kinetics of Pd and Ag from hydrazine based plating baths (Cheng and Yeung, 1999;

Yeung *et al.*, 1999). The electroless plating kinetics of Pd and Ag (Yeung *et al.*, 1999) and the electroless co-deposition kinetics of Pd and Ag from a mixed plating bath (Cheng and Yeung, 1999) included the used of porous Vycor tubes with a total plating area of 20 cm^2. The amount of metal deposited over time was monitored by using a quartz crystal microbalance under the assumption that the plating on the pre-plated quartz probe and the porous Vycor tube occurred at the same rate. It was interesting to note that the electroless plating kinetics reported by Yeung *et al.* (1999) and Cheng and Yeung (1999) were obtained from the initial rate data from an un-stirred plating bath, where no indication was given on why the effect of external mass transfer was assumed to be negligible. The effect of external mass transfer on the electroless plating rates of Pd and Ag has not been quantified yet.

The formation of Pd/alloy films (i.e., Ag and Cu) on porous supports via the electroless plating is typically accomplished by the sequential deposition of the metal of choice, followed by high temperature annealing treatment under inert (i.e, He, N_2, Ar, etc.) or reactive (i.e., H_2) atmospheres. Sequential plating and annealing of the metal layers is usually referred to as the “coating and diffusion” method (Uemiya *et al.*, 1991a; Uemiya *et al.*, 1991b; Shu *et al.*, 1993; Jeema *et al.*, 1995; Keuler and Lorenzen, 2002; Ma *et al.*, 2004a). In this respect, electroless plating has been used to form Pd/Ag alloy films onto various substrates such as porous glass (Uemiya *et al.*, 1991b; Cheng and Yeung, 1999),ceramic supports of type α-Al_2O_3 and/or γ-Al_2O_3/α-Al_2O_3 (Uemiya *et al.*, 1991a; Uemiya *et al.*, 1991b; Cheng *et al.*, 2002; Hou and Hughes, 2002; Keuler and Lorenzen, 2002; Hou and Hughes, 2003; Huang *et al.*, 2003) and porous sintered metals (Shu *et al.*, 1994; Shu *et al.*, 1995; Ayturk *et al.*, 2004a; Ma *et al.*, 2004a; Tong *et al.*, 2005d; Ayturk *et al.*, 2006; Yepes *et al.*, 2006). Moreover, the formation of Pd/Cu films by electroless plating has been carried out on porous glass (Uemiya *et al.*, 1991b), α-Al_2O_3 (Roa *et al.*, 2002; Roa and Way, 2003a; Howard *et al.*, 2004) and α-Al_2O_3 and/or ZrO_2 coated α-Al_2O_3 supports (Roa *et al.*, 2002; Roa and Way, 2003a; Roa and Way, 2003b; Roa *et al.*, 2003). A detailed literature summary of the hydrogen permeation characteristics of composite Pd and Pd/alloy membranes formed by the electroless plating on Ta, V-15Ni, ceramic hollow fibers, porous glass, ceramic and porous sintered metal supports are given in Table 2-5, Table 2-6, Table 2-7and Table 2-8, respectively.

Table 2-5. Summary of the Pd and Pd/Alloy membranes formed by the electroless plating on Ta, V-15Ni and ceramic hollow fibersupports

Reference	Dep$^{\underline{n}}$ Method	Membrane Layer	Support	Thickness (µm)	Temp. (°C)	H_2 Permeance (m^3/m^2-h-atm^n)	n-value	Selectivity H_2/N_2	Duration (hours)
Ozaki *et al.* (2003)	ELP	Pd	V-15Ni	0.2	350	4364[*]	0.5	∞	315
Pan *et al.* (2003)	ELP	Pd	Ceramic Hollow Fibers	3	430	14.9	1	1000	800
Tong *et al.* (2006b)	ELP	Pd	α-Al_2O_3 Hollow Fiber	5	500	33.5	1	∞	170
Rothenberger *et al.* (2003)	ELP	Pd	Ta	2	350	243.9	0.5	n/a	192
		Pd	Ta	2	650	74.4	0.5	n/a	144
		Pd	Ta	2	900	48.8	0.5	n/a	72

Table 2-6. Summary of the Pd and Pd/Alloy membranes formed by the electroless plating on porous glass supports

Reference	Dep$^{\underline{n}}$ Method	Membrane Layer	Support	Thickness (µm)	Temp. (°C)	H_2 Permeance (m^3/m^2-h-atm^n)	n-value	Selectivity H_2/N_2	Duration (hours)
Yeung *et al.* (1999)	ELP	Pd	Porous Vycor	1.6	350	1.1	0.5	10^4	n/a
Uemiya *et al.* (1991b)	ELP	Pd	Porous Glass	20	400	16.7	0.5	n/a	n/a
		Pd	Porous Glass	20	500	21.3	0.5	n/a	n/a
Uemiya *et al.* (1991b)	ELP	$Pd/Ag_{7.0\%}$	Porous Glass	21.6	400	8.4	0.5	n/a	n/a
Uemiya *et al.* (1991b)	ELP	$Pd/Cu_{6.2\%}$	Porous Glass	18.9	400	5.9	0.5	n/a	n/a
		$Pd/Cu_{6.2\%}$	Porous Glass	18.9	500	9.4	0.5	n/a	n/a
Cheng and Yeung (1999)	Co-ELP	$Pd/Ag_{12\%}$	Porous Vycor	1.2	400	2.2	0.5	76[†]	n/a

---

[*] Original permeability for a 0.2 µm thick Pd/V-15Ni membrane was reported as 3.4×10^{-8} mol/m-s-$Pa^{0.5}$ at 350°C, which is equivalent to a value of 4364 m^3/m^2-h-$atm^{0.5}$!!!

[†] H_2/He

Table 2-7. Summary of the Pd and Pd/Alloy membranes formed by the electroless plating on ceramic supports

Reference	Dep$^{\underline{n}}$ Method	Membrane Layer	Support	Thickness (µm)	Temp. (°C)	H_2 Permeance (m^3/m^2-h-atm^n)	n-value	Selectivity H_2/N_2	Duration (hours)
Kikuchi *et al.* (2000)	ELP	Pd	Al_2O_3	8	500	28.2	1	∞	n/a
Uemiya *et al.* (1991a)	ELP	Pd	Alumina	4.5	400	36.8	0.5	n/a	n/a
Cheng *et al.* (2002)	ELP	Pd	α-Al_2O_3	3.0	450	12.0	0.5	890[†]	n/a
Li *et al.* (1999; 2000)	ELP	Pd	α-Al_2O_3	7.6	467	34.6	0.5	10.3	n/a
	ELPO[*]	Pd[†]	α-Al_2O_3	9.2	467	27.1	0.5	96.5	n/a
		Pd[‡]	α-Al_2O_3	10.3	467	24.2	0.5	970	n/a
Zhao *et al.* (1998)	ELP	Pd	γ-Al_2O_3	1	450	87	1	23	n/a
Zhao *et al.* (2000)	ELP	Pd	γ-Al_2O_3/α-Al_2O_3	1	314	1.3	1	65	n/a
Uemiya *et al.* (1991a)	ELP	Pd/$Ag_{11\%}$	Alumina	5.0	400	47.0	0.5	n/a	n/a
		Pd/$Ag_{18\%}$	Alumina	5.3	400	52.7	0.5	n/a	n/a
		Pd/$Ag_{23\%}$	Alumina	5.8	400	53.4	0.5	n/a	n/a
		Pd/$Ag_{26\%}$	Alumina	5.9	400	43.1	0.5	n/a	n/a
		Pd/$Ag_{31\%}$	Alumina	6.4	400	34.7	0.5	n/a	n/a
Cheng *et al.* (2002)	ELP	Pd/$Ag_{3.3\%}$	α-Al_2O_3	1.6	450	11.1	0.5	750[†]	n/a
		Pd/$Ag_{16.5\%}$	α-Al_2O_3	1.8	450	25.3	0.5	850[†]	n/a
Hou and Hughes (2002)	ELP	Pd/Ag	α-Al_2O_3	5.5	400	30.6	1	1000	500
Hou and Hughes (2003)	ELP	Pd/Ag	α-Al_2O_3	5.5	325	14.2	0.614	4500	960
		Pd/Ag	α-Al_2O_3	5.5	500	30.2	0.614	n/a	960
Keuler and Lorenzen (2002)[§]	ELP	Pd/$Ag_{24\%}$	α-Al_2O_3	2.14	410	53.4	1	381	n/a
		Pd/$Ag_{20\%}$	α-Al_2O_3	2.13	410	37.7	1	189	n/a
		Pd/$Ag_{23\%}$	α-Al_2O_3	2.16	410	49.3	1	329	n/a
Huang *et al.* (2003)	Co-ELP	Pd/$Ag_{10\%}$	α-Al_2O_3	20	343	1.2	0.968	178	n/a
Roa *et al.* (2002)	ELP	Pd/$Cu_{19\%}$	α-Al_2O_3	11.6	450	16.8	0.5	105	n/a
		Pd/$Cu_{22\%}$	α-Al_2O_3	12.5	450	11.9	0.5	206	n/a
Roa *et al.* (2002)	ELP	Pd/$Cu_{12\%}$	ZrO_2/α-Al_2O_3	12.0	450	28.7	0.5	860	n/a
		Pd/$Cu_{10\%}$	ZrO_2/α-Al_2O_3	1.0	350	38.5	0.5	1390	n/a
		Pd/$Cu_{40\%}$	ZrO_2/α-Al_2O_3	1.5	450	139.9	0.5	90	n/a

---

[*] Electroless plating combined with Osmosis

[†] Modified electroless plating with osmosis: 1st repair

[‡] Modified electroless plating with osmosis: 2nd Repair

[§] Hydrogen permeance after oxidation at 310-350°C for 1-3 hours

(Table 2-7 Cont'd) Reference	Dep$^{\underline{n}}$ Method	Membrane Layer	Support	Thickness (µm)	Temp. (°C)	H_2 Permeance (m^3/m^2-h-atm^n)	n-value	Selectivity H_2/N_2	Duration (hours)
Roa and Way (2003a; 2003b)	ELP	Pd/$Cu_{9\%}$	$ZrO_2/\alpha\text{-}Al_2O_3$	11	350	3.3	0.5	1100	n/a
		Pd/$Cu_{10\%}$	$ZrO_2/\alpha\text{-}Al_2O_3$	1.0	350	19.2	0.5	2000	n/a
		Pd/$Cu_{30\%}$	$ZrO_2/\alpha\text{-}Al_2O_3$	1.5	350	43.5	0.5	48	n/a
		Pd/$Cu_{28\%}$	$ZrO_2/\alpha\text{-}Al_2O_3$	1.0	350	31.6	0.5	20	n/a
		Pd/$Cu_{40\%}$	$ZrO_2/\alpha\text{-}Al_2O_3$	1.5	350	97.9	0.5	93	n/a
		Pd/$Cu_{10\%}$	$ZrO_2/\alpha\text{-}Al_2O_3$	3.5	350	10.9	0.5	7000	1680
		Pd/$Cu_{90\%}$	$ZrO_2/\alpha\text{-}Al_2O_3$	2.5	350	0.08	0.5	100	n/a
Roa and Way (2003)	ELP	Pd/$Cu_{28\%}$	$\alpha\text{-}Al_2O_3$	27.6	500	2.1	0.5	14	360
		Pd/$Cu_{20\%}$	$\alpha\text{-}Al_2O_3$	11.0	500	24.5	0.5	70	n/a
		Pd/$Cu_{19\%}$	$\alpha\text{-}Al_2O_3$	11.6	500	36.4	0.5	170	480
		Pd/$Cu_{22\%}$	$\alpha\text{-}Al_2O_3$	12.5	450	12.6	0.5	270	n/a
Roa and Way (2003)	ELP	Pd/$Cu_{9\%}$	$ZrO_2/\alpha\text{-}Al_2O_3$	12.0	500	55.9	0.5	1400	624
		Pd/$Cu_{30\%}$	$ZrO_2/\alpha\text{-}Al_2O_3$	1.5	350	46.2	0.5	47	144

Table 2-8. Summary of the Pd and Pd/Alloy membranes formed by the electroless plating on porous sintered metal supports

Reference	Dep$^{\underline{n}}$ Method	Membrane Layer	Support	Thickness (μm)	Temp. (°C)	H_2 Permeance (m^3/m^2-h-atm^n)	n-value	Selectivity H_2/N_2	Duration (hours)
Jarosch and de Lasa (1999)	ELP	Pd	Inconel Disk	78.4	500	2.1	0.5	n/a	n/a
Jeema *et al.* (1996)	ELP	Pd	Fe-PSS[*]	6	400	11.3	0.5	n/a	n/a
Wang *et al.* (2004)	ELP	Pd	ZrO_2-PSS	10	500	14.9	0.5	140[†]	n/a
Su *et al.* (2005)	ELP[‡]	Pd	SiO_2-PSS	3	500	18.8	1	300-400	n/a
		Pd	SiO_2-PSS	6	500	21.2	1	300	n/a
		Pd	SiO_2-PSS	11	500	10.5	1	n/a	n/a
Tong *et al.* (2004b)	ELP	Pd	CeO_2-PSS	8	500	38.6	0.5	800[†]	n/a
Tong *et al.* (2005c)	ELP	Pd	CeO_2-PSS	13	500	27.5	0.5	∞	n/a
Tong and Matsumura (2005)	ELP	Pd	CeO_2-PSS	11	500	28	0.5	2000[†]	n/a
Tong *et al.* (2006a)	ELP	Pd	CeO_2-PSS	6	500	24	0.85	14[†]	n/a
	ELP	Pd[§]	CeO_2-PSS	6.4	500	28	0.73	565[†]	
Tong *et al.* (2006a) Tong and Matsumura (2004)	ELP	Pd	CeO_2-PSS	10	500	25.1	0.62	108[†]	n/a
Tong *et al.* (2005b) Tong *et al.* (2005e)	ELP	Pd	$Al(OH)_3$-PSS	6	500	21.2	1	∞	n/a
		Pd	$Al(OH)_3$-PSS	6	550	24.5	1	∞	n/a
Tong *et al.* (2005e)	ELP	Pd	$Al(OH)_3$-PSS[**]	6	500	26.1	1	∞	260
Tong *et al.* (2005d)	ELP	Pd	$Al(OH)_3$-PSS	3	500	29.8	1	∞	n/a
Mardilovich *et al.* (1998a)	ELP	Pd	PSS	20	350	8	0.5	5000	1100
Mardilovich *et al.* (2002)	ELP	Pd	PSS	11.7	350	20	0.5	1000	200
		Pd	PSS	33.8	350	5.1	0.5	n/a	30
Shu *et al.* (1994)	ELP	Pd	PSS	20	500	9.6	0.5	n/a	n/a
Li (1998)	ELPO	Pd[††]	PSS	10	380	7.3	0.5	1000	250
		Pd	PSS	10	427	10.9	0.5	1000	250
		Pd	PSS	10	480	17.3	0.5	1000	250
Mardilovich *et al.* (2006)	ELP	Pd	Pd/Ag[‡‡]+PSS	7.9	500	68.5	0.5	n/a	1388

---

[*] PSS modified with the shot peening of Fe particles

[†] H_2/Ar

[‡] Activation of the support was achieved by CVD

[§] After CVD repair

[**] Plating was accomplished without support activation

[††] Modified electroless plating with Osmosis

[‡‡] Pd/Ag intermetallic diffusion barrier was formed by the BMML deposition technique

(Table 2-8 Cont'd) Reference	Dep^n Method	Membrane Layer	Support	Thickness (μm)	Temp. (°C)	H_2 Permeance (m^3/m^2-h-atm^n)	n-value	Selectivity H_2/N_2	Duration (hours)
Guazzone (2005)	ELP	Pd	Al_2O_3-PHST	5.6	500	38.8	0.5	818	185
		Pd	Al_2O_3-PHST	7.7	500	50	0.5	42	52
		Pd	Al_2O_3-PHST	10	500	41	0.5	280	1100
		Pd-Cu	Al_2O_3-PHST	10	450	30	0.5	857	800
Yepes *et al.* (2006)	ELP	Pd-Ag	α-Fe_2O_3-PSS	16	400	5.3	0.52	3000	n/a
		Pd-Ag	α-Fe_2O_3-PSS	16	500	10.7	0.46	n/a	n/a
Yepes *et al.* (2006)	ELP	Pd-Ag	γ-Al_2O_3-PSS	16	400	8.4	0.59	300	n/a
		Pd-Ag	γ-Al_2O_3-PSS	16	500	7.7	0.59	n/a	n/a
Yepes *et al.* (2006)	ELP	Pd-Ag	(Pd) γ-Al_2O_3-PSS	16	400	13.9	0.71	200	n/a
		Pd-Ag	(Pd) γ-Al_2O_3-PSS	16	500	21.1	0.70	n/a	n/a
Tong *et al.* (2005d)	ELP	Pd + $Pd_{0.8}Ag_{0.2}$[§§]	$Al(OH)_3$-PSS	5	500	25.5	1	∞	n/a

---

[§§] $Pd_{0.8}Ag_{0.2}$ alloy was deposited via electroplating

2.4.6.3. *Microstructure Analysis of the Electroless Plating Deposits*

The morphology resulting from the electroless plating of Pd on porous substrates (porous, glass, ceramics and porous sintered metal supports) has been studied in detail and well characterized (Shu *et al.*, 1991a; Uemiya *et al.*, 1991a; Uemiya *et al.*, 1991b; Shu *et al.*, 1993; Mardilovich *et al.*, 1998a; Keuler *et al.*, 1999b, 1999a; Ma *et al.*, 2004a; Ayturk *et al.*, 2006; Ayturk *et al.*, 2007). The electroless plating of Pd forms a uniform coverage over the entire support surface in the form of tightly knit clusters (1 µm or smaller), which penetrates into every valley and crevasse of the bottom surface or walls of the substrate. Indeed, the uniformity of Pd deposits is effective in covering welded areas and macroscopic defects such as dents, tool marks and abrasions (Mardilovich *et al.*, 2002; Ma *et al.*, 2004a). Similar observations were also reported for the Cu deposits formed by the electroless plating (Ma *et al.*, 2004a). Unlike Pd and/or Cu, electroless plating of Ag usually takes place on easily accessible surface sites of the porous substrate and results in the formation of clusters that grow perpendicular to the surface and leads to a heterogeneous rough surface coverage, as well as poor penetration at the pore mouths and valleys on the porous surface (Shu *et al.*, 1993; Cheng and Yeung, 1999; Keuler *et al.*, 1999b, 1999a; Ma *et al.*, 2004a; Ayturk *et al.*, 2006; Ayturk *et al.*, 2007). The topological features of the electroless Ag deposits on porous substrates often manifest itself with the formation of concentration gradients across the entire film, which may present additional difficulty in forming uniform alloys during high temperature annealing.

In an effort to control the concentration profiles of the Pd/Ag layers formed by the electroless plating and to form Pd/Ag alloys at lower annealing temperatures, the electroless co-plating of Pd and Ag metals from the same plating bath has been proposed as an alternate synthesis route (Shu *et al.*, 1993; Cheng and Yeung, 1999; Huang *et al.*, 2003). Shu *et al.* (1993) have succeeded to form Pd/Ag layers (53-56 wt% Ag) on porous stainless steel supports via electroless co-deposition. However, the co-deposition of Pd an Ag metals was passivated by the preferential deposition of Ag due to its favorable oxidation-reduction potential of $\Delta E^\circ_{Ag} = 1.73$ V over Pd ($\Delta E^\circ_{Pd} = 1.12$ V) (Shu *et al.*, 1993; Cheng and Yeung, 1999). Nonetheless, the heat treatment of the as-deposited

Pd/Ag film under hydrogen at 400°C for 150 minutes showed the formation of an Ag-rich Pd/Ag alloys phase. In order to avoid preferential deposition of Ag, Shu *et al.* (1993) have suggested the use of a thin Pd layer deposited prior to electroless co-deposition. Furthermore, Cheng and Yeung (1999) have investigated the factors affecting the co-deposition by varying the hydrazine and ammonium hydroxide concentrations and reported that the co-deposition of Pd and Ag was improved at elevated temperatures with the use of low ammonium hydroxide concentration, a moderate hydrazine to metal ratio. For a 1.2 μm Pd/Ag film (12 wt% Ag) formed on a porous Vycor tube, Cheng and Yeung (1999) have reported an extremely low hydrogen permeance of 2.2 m^3/m^2-h-$atm^{0.5}$ with a H_2/He selectivity of 76 at 400°C. Similarly, Huang *et al.* (2003) have reported a hydrogen permeance of only 1.2 m^3/m^2-h-$atm^{0.5}$ with a H_2/N_2 selectivity of 178 at 343°C for a 20 μm Pd/Ag film (10 wt% Ag) formed on a porous α-Al_2O_3 support via electroless co-deposition. The limited number of permeation data suggests that the synthesis of composite Pd/Ag membranes by the use of electroless co-deposition necessitate further investigation.

2.4.6.4. Modifications to the Conventional Electroless Plating Technique

In order to improve the deposition characteristics, film density and surface morphology of the Pd and Pd/alloy layers, many researchers have re-evaluated different aspects of the synthesis routes and suggested modifications to the conventional electroless plating technique.

Yeung *et al.* (1995) have reported that the addition of formaldehyde (1 mL/L) to a hydrazine-based plating bath increased the induction period for the plating reaction but resulted in a smooter and more uniform morphology with high surface luster and relatively smaller grain size. Furthermore, Yeung *et al.* (1995) have used the osmosis in combination with electroless plating for the preparation of composite Pd/Vycor membranes. The use of osmosis in combination with electroless plating was achieved by immersing the porous Vycor glass in the plating bath while pumping a concentrated $CaCl_2$ solution (3M) through the tube-side. The concentration difference between the solutes across the membrane gave rise to osmotic pressure and resulted in a net water flux across the membrane from dilute to concentrated solution. Compared to the conventional plating baths, Yeung *et al.* (1995) have noted that the Pd film formed by the combined use of the electroless plating and osmosis has produced smaller grain size and a denser Pd film. The changes in the Pd microstructure have been verified by the AFM analysis conducted by Souleimanova *et al.* (1999). Indeed, the average grain size for the Pd film formed by the combined use of electroless plating with osmosis was measured as 150 nm with respect to a value of 350 nm in the case of conventional plating bath (Souleimanova *et al.*, 2000; Souleimanova *et al.*, 2001). Mardilovich *et al.* (1998a) and Zheng and Wu (2000) have also reported grain size values in the order of 380 nm and 800 to 360 nm, respectively. An improvement in the density of the deposited Pd film have also been reported by Zheng and Wu (2000) with the use of a hydrothermal method.

For a 10 µm thick composite Pd/PSS membrane prepared by the use of electroless plating and osmosis, Li (1998) have reported hydrogen permeance of 17.3 m^3/m^2-h-$atm^{0.5}$ with H_2/N_2 selectivity over 1000 at 480°C. Li *et al.* (1999; 2000) have used the osmosis to repair defects in a 7.6 µm thick composite Pd/α-Al_2O_3 membrane with an initial hydrogen permeance and H_2/N_2 selectivity of 34.6 m^3/m^2-h-$atm^{0.5}$ and 10 at 467°C, respectively. After two sets of electroless plating and osmosis treatment, the membrane thickness, hydrogen permeance at 467°C and H_2/N_2 selectivity was reported as 10.3 µm, 24.2 m^3/m^2-h-$atm^{0.5}$ and 970, respectively.

Recently, Tong *et al.* (2006a) have used a combined method of electroless plating and chemical vapor deposition to repair the surface defects of a 6 µm thick Pd membrane formed on a PSS support modified with CeO_2 particles. At 500°C, the hydrogen permeance and H_2/Ar selectivity of the defected membrane was 24 m^3/m^2-h-$atm^{0.85}$ and 14, respectively. CVD modification was achieved by the use of Pd(II) hexafluoaacetylacetonate ($Pd(F_6acac)_2$), which was sublimated in a reactor cell at 50°C and decomposed at a temperature range of 200-250°C. After three rounds of CVD repair, the weight gain corresponded to a thickness of only 0.4 µm. At 500°C, the hydrogen permeance and H_2/Ar selectivity of the repaired membrane was 28 m^3/m^2-h-$atm^{0.85}$ and 565, respectively (Tong *et al.*, 2006a).

Zhao *et al.* (1998) have modified the surface activation step by replacing the conventional $SnCl_2$-$PdCl_2$ cycle with a sol-gel process by the use of a Pd(II)-modified boehmite sol. For a 1 μm thick Pd/γ-Al_2O_3 membrane formed by the modified activation process, Zhao *et al.* (1998) have reported a hydrogen permeance of 87 m^3/m^2-h-atm at 450°C, but with an extremely low H_2/N_2 selectivity of only 23.

Uemiya *et al.* (2003) have suggested minor modifications for the conventional synthesis steps such as increasing the temperature of the activation from room temperature to 35^{o}C, decreasing the number of repeated loops for activation, immersing the support in distilled water prior to activation, decreasing the ratio of surface area to plating volume and finally immersing the activated ceramic support in an aqueous hydrazine solution prior to electroless plating. Similarly, Tong *et al.* (2005e) have treated the $Al(OH)_3$ modified PSS supports by immersing in the commercial activation and hydrazine solutions (Okuno Industries) prior to the electroless plating of Pd. Mardilovich *et al.* (1998a) have suggested the immersion of the support in DI water and dilute HCl solutions (0.1 M) prior to activation in order to avoid any surface contaminants which might lead to the formation of blisters on the porous surface during electroless plating.

3. Experimental

3.1. Membrane Synthesis

3.1.1. Porous and Non-porous Metal Supports

The types and the geometries of the metal supports used in this study include non-porous stainless steel (SS) plates, porous 316L stainless steel plates (PSS), porous Hastelloy plates (PHST), PSS cylindrical cups, and PSS, PHST and porous Inconel tube assemblies as shown in Figure 3-1. All support metals were purchased from Mott Metallurgical Corporation (Farmington, CT).

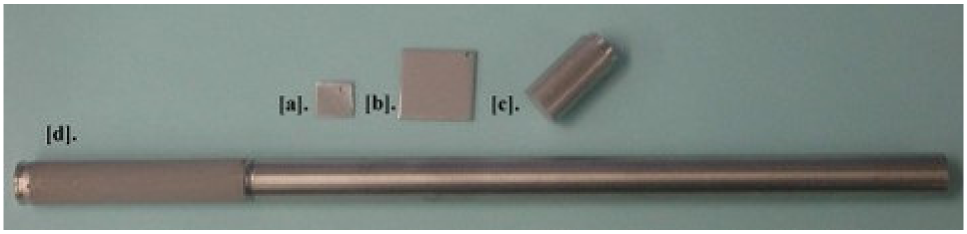

Figure 3-1: Membrane supports: [a]. Non-porous plates, [b]. Porous plates, [c]. Porous cups and [d]. Membrane tube assembly (porous cup welded to non-porous tube)

PSS and PHST plates were prepared by cutting 1 dm^2 media grade (0.1 µm, 0.2 µm and 0.5 µm) sheets into 1x1 cm^2 or 1x1.5 cm^2 pieces. The support grades were determined by Mott using the ASTM E-128 standard procedure. As described by Rubow and Stange (2002), the procedure related the capillary size to the pressure drop required to expel a liquid from the pore using air flow as the test gas. The support grades are specified according to the percentage of particles that are rejected during filtration with a diameter greater or equal to that specified grade such as 0.1, 0.2 and 0.5 μm. For instance, 95% of the particles with diameters larger than 0.5 μm are rejected for a 0.5 μm grade support. However, previous work in this has shown that the pore sizes for PSS supports obtained by the Hg porosimetry were considerably larger than the support grade based on ASTM E-128 (Mardilovich *et al.*, 2002). The mercury porosimetry analysis of a 0.5 μm grade cup resulted in a distribution of pores ranging from 1 to 12 μm in diameter. Also, large pores (10 to 20 μm) could be found on the surface of the porous supports.

The dimensions of the 0.5 μm grade PSS cylindrical cups were 1.27 cm in OD and 2.54 cm long with a wall thickness of 0.16 cm. Membrane tube assemblies were prepared by sealing at one end with a blind end cap and welding to a non-porous metal tube on the other end. The dimension of the membrane tube assemblies of variable media grades (0.1, 0.2 and 0.5 μm) and different types (PSS-316L, PHST and Inconel) were either 1.27 cm or 5.08 cm in OD and variable length (2.54, 5.08 and 15.24 cm). Typical compositions for the support metals PSS-316L, PHST and Inconel are given in Table 3-1.

Table 3-1. Chemical composition of porous sintered metal supports (wt%)

Component	PSS-316L (min-max wt%)	Hastelloy (min-max wt%)	Inconel (min-max wt%)
Fe	65-74	2-6	0-5
Cr	16-18	20-22.5	20-23
Ni	10-14	50-63	54.9-68.9
Mo	-	12.5-14.5	8-10
W	-	2.5-3.5	-
Co	-	0-2.5	0-1
C	0-0.03	0-0.01	0-0.1
Si	0-0.75	0-0.08	0-0.5
Mn	0-2	0-0.5	0-0.5
V	-	0-0.35	-
P	0-0.045	0-0.025	0-0.015
S	0-0.03	0-0.01	0-0.015
N_2	0-0.10	-	-
Ti	-	-	0-0.40
Nb+Ta	-	-	3.15-4.15
Al	-	-	0-0.40

3.1.2. Pre-Treatment of the Metal Supports

Prior to oxidation, activation and electroless plating, all the support metals were cleaned for the effective removal of grease, oil, dirt, corrosion products and other surface contaminants. This was achieved by initial mechanical treatment of the welded regions by the use of either a 600 grid sand paper or a stainless steel brush and by cleaning the supports in an ultrasonic bath with an alkaline solution for about 30-60 minute at 60°C. Chemicals used for the preparation of the alkaline solution are summarized in Table 3-2.

Table 3-2. Chemical composition of the alkaline solution

Component	Amount	Vendor
$Na_3PO_4.12H_2O$, 98% min., ACS	45 g/L	Alfa Aesar
Na_2CO_3, 99.5% min., ACS	65 g/L	Alfa Aesar
NaOH, 97% min., ACS	45 g/L	Alfa Aesar
Detergent	5 mL/L	-

Following the immersion in the alkaline solution, supports were washed and rinsed thoroughly first with pressurized tap water for 1 hour or until the pH of the surface reached a value of 7, and then, for 3 loops of 15 minutes of DI H_2O and 15 minutes of iso-propanol in ultrasonic bath to hasten the drying of the supports. Finally, supports were dried at 120°C overnight in a VWR Scientific (Model 1350 FM) forced air oven.

An intermediate metal-oxide layer is used to protect membranes from the intermetallic diffusion of support elements (Fe, Cr and Ni) during high temperature H_2 permeation tests. Prior to activation step, supports were oxidized in stagnant air at different temperatures between 400°C-800°C for a period of 6 to 12 hours using Lindberg (Blue M732) oven operated at a heating and cooling rate of 2-5°C/min.

3.1.3. Activation and Electroless Plating

In order to shorten the induction period for the autocatalytic decomposition reaction of the metastable complexes of Pd and Ag salts on the target surface and to initiate the electroless plating process, the surface of the metal supports were activated by seeding with the Pd nuclei according to the following reaction:

$$Pd^{2+} + Sn^{2+} \rightarrow Pd^{0} + Sn^{4+} \tag{3-1}$$

The solutions for the activation were prepared by using a 1 g/L of tin (II) chloride dihydrate (Aldrich, 98%, ACS reagent grade) and 0.1 g/L of palladium (II) chloride (Alfa

Aesar, 99.9%) mixed with a 1 mL/L of HCl (~37%). The chemicals used for the preparation of the activation solutions are listed in Table 3-3.

Table 3-3. Chemicals used for support activation

Chemical	Amount	Vendor
$SnCl_2.2H_2O$, 98% ACS	1.0 g/L	Aldrich
$PdCl_2$, 99.9% (metal basis)	0.1 g/L	Alfa Aesar
HCl (~37%)	1.0 mL/L	Merck
Temperature, °C	Room Temp.	-

The activation procedure consisted of first dipping the substrate in the $SnCl_2$ (sensitizing) solution and then in $PdCl_2$ (activation) solution with intermediate rinsing in DI H_2O between the solutions and also rinsing with a 0.01 M HCl solution after immersion in the $PdCl_2$ solution in order to prevent the hydrolysis of Pd^{2+} ions. The rinsing with DI H_2O is of great importance in order to avoid the attachment of by-products of Sn^{2+} hydrolysis such as $Sn(OH)_{1.5}Cl_{0.5}$ and other hydroxy-chlorides on the surface of the support metal. An excess of Sn^{2+} on the target surface may result in a loose (crumbly), easy-to-peel layer, while a deficiency of Sn^{2+} can lead to non-uniform seeding of the palladium nuclei. The sensitizing/activation cycle was typically repeated 3-6 times until a completely activated surface, typically in a uniform dark-brown color, was reached.

After activation, Pd and/or Ag were deposited at 60°C usually for durations of 90 minutes by using the electroless plating bath compositions shown in Table 3-4. It is also important to let the freshly prepared Pd and/or Ag plating solutions rest overnight in order to form stable complexes.

Table 3-4. Chemical compositions of the plating solutions

Chemical	Pd Bath	Ag Bath	Cu Bath
$Pd(NH_3)_4Cl_2\cdot H_2O$ (g/L)	4.0	-	-
$AgNO_3$ (g/L)	-	0.519	
$CuSO_4\cdot 5H_2O$ (g/L)	-	-	20
$Na_2EDTA\ 2H_2O$ (g/L)	40.1	40.1	30
NH_4OH (28%) (mL/L)	198	198	-
H_2NNH_2 (1 M) (mL/L)	5.6	5.6	-
HCHO (37%) (mL/L)	-	-	14
EDA (ppm)	-	-	100
$K4Fe(CN)_6\cdot 3H_2O$ (ppm)	-	-	35
$(C_2H_5)_2NCS_2Na\cdot 3H_2O$ (ppm)	-	-	5
pH	10-11	10-11	12-13
Temperature (°C)	60	60	20-25

Hydrazine was added to the plating solution prior to the immersion of the activated support metal in a constant temperature plating bath operated at 60°C. Depending on the type of the support metal (i.e., plates, cups or tube assemblies), plating cells used for the electroless deposition were modified by the use of varying size of beakers and graduated cylinders in order to maintain a constant volume to area ratio of ~3.5-4 cm^3/cm^2.

Between each platings, the coated substrate was rinsed with pre-heated DI H_2O and placed in a fresh plating solution for further deposition. Since the activity of the plating bath decreases due to the depletion of Pd and/or Ag ions and the reducing agent hydrazine, the plating solution has to be replaced with a fresh one in order to maintain the plating rate. No further plating was performed after 3-4 rounds of plating due to the deactivation of the support. The membrane was cooled-down to room temperature, washed with DI H_2O and finally dried at 120°C overnight. The formation of a dense membrane layer required the repetition of the above-described procedure and the membrane was deemed as dense when the helium flux was not detectable at a trans-membrane pressure difference of 1 atm at room temperature.

The weight gain resulting from all the synthesis steps was determined gravimetrically by using a Mettler AJ100 type microbalance (max. 110 g) and a Sartorius LP8200S type balance (max. 8.2 kg). The average thickness of the deposited film was calculated by dividing the weight gain of the sample by the product of the total (porous + non-porous) surface area and the density of the metal as shown in Equation (3-2):

$$L = \frac{\Delta m x 1000}{A_t x \rho_{metal}} \qquad (3\text{-}2)$$

Where L is the thickness in μm, Δm is the weight gain in mg, A_t is the total plating area in cm^2 and ρ_{metal} is the density of the metal in g/cm^3.

The characteristics of all the composite Pd and Pd/Ag membranes prepared throughout this dissertation are summarized in Table 3-5.

Table 3-5. Characteristics of the composite Pd and Pd/Ag membranes prepared in this study

Membrane Label	Support Type$_{Grade}$	Surface Area [cm^2]	Oxidation T(°C)/t(h)	Grading[*]	Dep$^{\underline{n}}$ Method[†]	Membrane Layer	Ag [wt%]	Thickness -Weight- [μm]	Thickness -SEM- [μm]
Et001[‡]	PSS$_{0.1\mu m}$	20-25	Un-Ox$^{\underline{d}}$	n/a	HBT$_{Ag}$	Pd/Ag	n/a	5.6	10
Et002	PSS$_{0.5\mu m}$	20-25	Un-Ox$^{\underline{d}}$	n/a	HBT$_{Ag}$	Pd/Ag	2.7	24.4	30-32
Et003	PSS$_{0.1\mu m}$	20-25	600°C/6h	n/a	HBT$_{Ag}$	Pd/Ag	5.1	30.9	33
Et004‡	PSS$_{0.1\mu m}$	20-25	600°C/12h	n/a	HBT$_{Pd}$	Pd/Ag	n/a	19.7	20-40
Et005	PSS$_{0.2\mu m}$	20-25	600°C/12h	n/a	HBT$_{Ag}$	Pd/Ag	2.1	27.8	35
001	PSS$_{0.5\mu m}$	20-25	400°C/6h	n/a	ELP	Pd	-	22.3	n/a
002	PSS$_{0.1\mu m}$	10-15	400°C/6h	n/a	BMML	Pd/Ag	1	80.7	n/a
003‡	PSS$_{0.1\mu m}$	10-15	400°C/6h	n/a	BMML	Pd/Ag	n/a	106	n/a
004	PSS$_{0.1\mu m}$	10-15	600°C/12h	n/a	HBT$_{Ag}$	Pd/Ag	12	15.6	30
007 (Ma-33)	PHST$_{0.1\mu m}$ 1E-15M-21	110-130	700°C/12h	n/a	HBT$_{Pd}$	Pd/Ag	4.7	15.7	n/a
008	PSS$_{0.1\mu m}$	20-25	Un-Ox$^{\underline{d}}$	n/a	ELP	Pd	-	43.5	n/a
010	PSS$_{0.2\mu m}$	20-25	700°C/6h	n/a	HBT$_{Co\text{-}Dep\underline{n}}$	Pd/Ag	n/a	36.8	n/a
011	PSS$_{0.2\mu m}$	20-25	600°C/6h	n/a	ELP	Pd	-	72.2	n/a
012	PSS$_{0.2\mu m}$	20-25	Un-Ox$^{\underline{d}}$	n/a	ELP	Pd/Ag	16.4	19.9	n/a
013 (Ma-46)	PHST$_{0.1\mu m}$ 1E-MF-21	110-130	Un-Ox$^{\underline{d}}$	α-Al$_2$O$_3$	ELP	Pd/Ag	16.9	10.9	n/a
014	Inconel$_{0.1\mu m}$	25-30	Un-Ox$^{\underline{d}}$	Al(OH)$_3$	ELP	Pd/Ag	30.6	10	8-12
015	Inconel$_{0.1\mu m}$	25-30	800°C/12h	Al(OH)$_3$	ELP	Pd/Ag	31.7	11.6	8.5-12
016	Inconel$_{0.1\mu m}$	25-30	800°C/12h	Al(OH)$_3$[§]	ELP	Pd/Ag	4.6	35	48
017	Inconel$_{0.1\mu m}$	25-30	800°C/12h	Al(OH)$_{3\S}$	ELP	Pd/Ag	31.3	4.6	5-7
018	Inconel$_{0.1\mu m}$	25-30	Un-Ox$^{\underline{d}}$	Al(OH)$_3$	ELP	Pd/Ag	16.7	12.5	25
019a	Inconel$_{0.1\mu m}$	25-30	Un-Ox$^{\underline{d}}$	Al(OH)$_3$	ELP	Pd/Ag	33.3	8.5	9
019b							26	10	12
020a	Inconel$_{0.1\mu m}$	25-30	Un-Ox$^{\underline{d}}$	Al(OH)$_3$	ELP	Pd/Ag	40	7.4	9
020b							30.3	9.7	15
021 (Ma-64)	Inconel$_{0.1\mu m}$	110-130	Un-Ox$^{\underline{d}}$	Al(OH)$_3$	ELP	Pd/Ag	31.3	14.6	n/a
022	Inconel$_{0.1\mu m}$	25-30	800°C/12h	Al(OH)$_3$	ELP w/ rpm	Pd/Ag	10.2	20.2	n/a
023	Inconel$_{0.1\mu m}$	25-30	800°C/12h	Al(OH)$_3$	ELP w/ rpm	Pd/Ag	11.8	16.3	n/a
025	Inconel$_{0.1\mu m}$	25-30	800°C/12h	Al(OH)$_3$	ELP w/ rpm	Pd	-	4.7	n/a
026‡	Inconel$_{0.1\mu m}$	25-30	800°C/12h	Al(OH)$_3$	ELP w/ rpm	Pd/Ag	23.9	5.9	n/a

---

[*] Grading of the porous supports with the pre-activated α-Al$_2$O$_3$ and Al(OH)$_3$ particles is discussed in Chapter 6.

[†] HBT, ELP and BMML refers to Hole Blowing Technique, Electroless Plating and Bi-Metal Multi-Layer Deposition, respectively. BMML and HBT are described in Chapters 5 and 6 in greater detail.

[‡] H$_2$ permeation test was not conducted yet.

[§] NP refers to Pd/Ag alloy nanoparticles. Synthesis and dip coating of NP layers is discussed in Chapter 11.

3.2. Membrane Characterization

3.2.1. He Leak Test Set-up and Annealing Test Rig

The helium permeance of the membrane was determined at room temperature at several different pressures between 0-3.5 atm before and after each synthesis step by the use of the He permeator cell shown in Figure 3-2[d]. Volumetric flow of the He gas was measured by means of three flow meters operating at different ranges, namely, GCA Wet Test Flow Meter from Precision Scientific for high flow rates up to 16 L/min, Alltech 4068 digital flow meter for medium flow rates in the range of 0.5 to 50 mL/min and bubble flow meter for very small flow rates below 0.5 mL/min. The permeator cell and the different range of flow meters used to monitor the room temperature He leak during synthesis are shown in Figure 3-2.

Annealing of the Pd and/or Ag layers deposited on metal plates, cups and tube substrates were conducted in a Blue AA type annealing furnace equipped with a permeator cell (shown in Figure 3-3), which was operated under inert (i.e., He, N_2) or reactive (i.e., H_2) atmospheres at different temperatures between 300-800°C with a heating/cooling rate of 1°C/min.

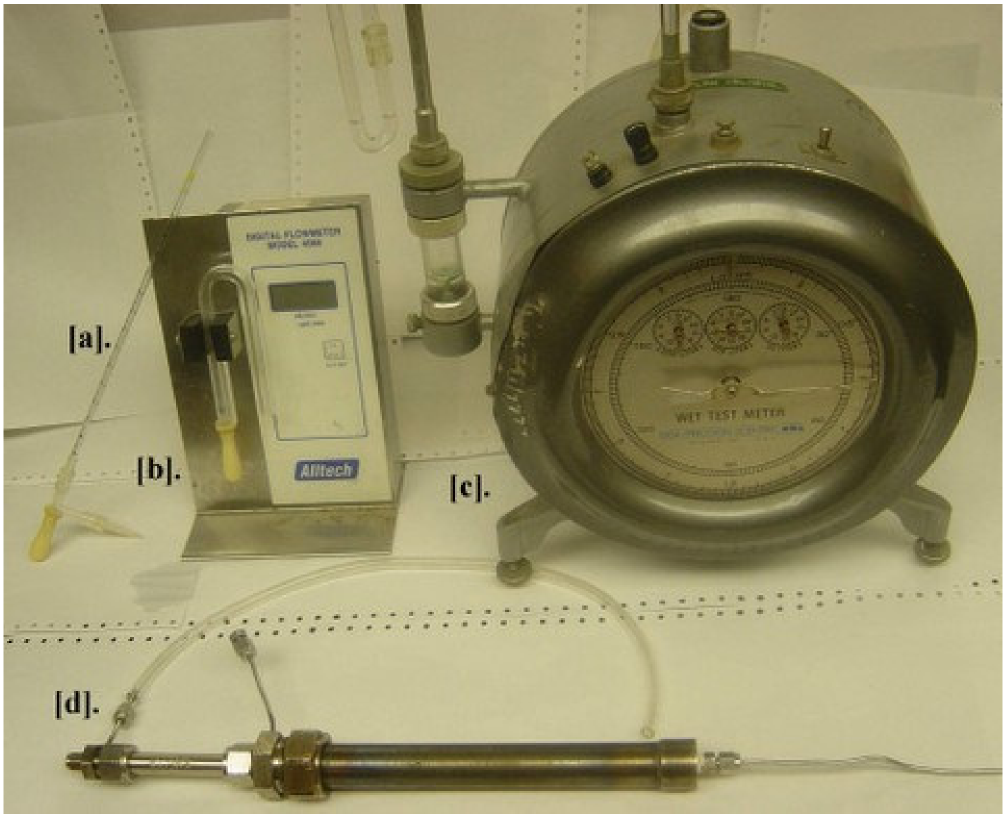

Figure 3-2: He leak test permeator cell and the volumetric flow measurement devices: [a]. Bubble-flow meter, [b]. Digital flow meter, [c]. Wet test meter, [d]. He permeator cell.

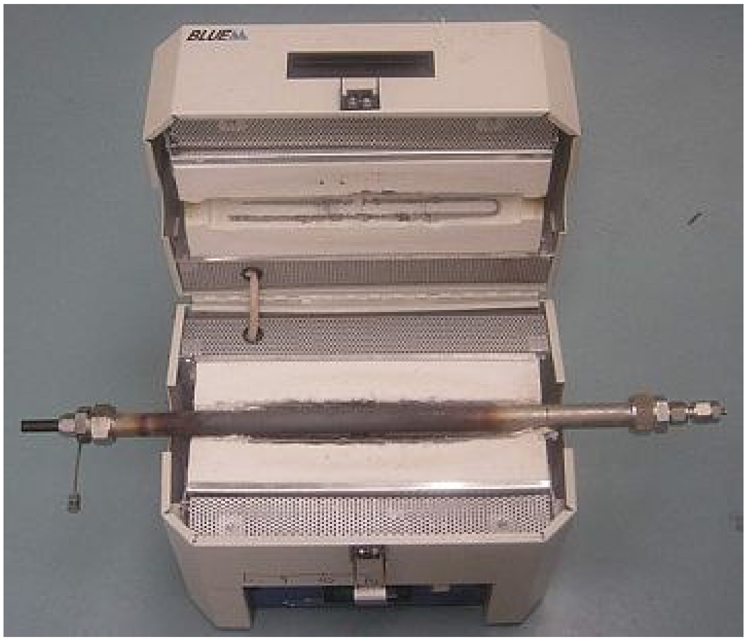

Figure 3-3: Annealing Test Rig

3.2.2. H_2 Permeator Cell and Permeation Test Rig Set-up

The schematic of the test-rig used for the H_2 permeation test is shown in Figure 3-4. The permeator cells used in the H_2 test rigs were a 1" OD, 20'' long (small test unit for ½" OD support tubes) or 2" OD, 40" long (large unit for 1" OD support tubes) 316L stainless steel tubes attached at the upper-end to the non-porous section of the membrane tube with a 1'' to ½'' or 2" to 1" Swagelok reducing unions (A), which were modified to allow the gas stream to exit from the shell-side. The lower-end of the permeator cells (B) was welded to a ¼'' stainless steel tube to allow gas stream to enter the shell-side. The upper-end was connected to the sweep (C) and tube-side exit module (D), which also contains the thermocouple connections. Helium sweep module consists of 1/16'' stainless steel tube inserted into the tube-side through ½'' Swagelok tee fitting. The temperature of the Watlow ceramic-fiber tubular heater was controlled by a Eurotherm 2116 temperature controller equipped with two J-type thermocouples. The first thermocouple was attached to the outer-side of the permeator cell by positioning over the middle of the porous membrane (E). The second thermocouple (F) was inserted into the tube by positioning against the middle of the inner wall of the porous membrane and was used to log the temperature. The permeator cell was mounted vertically/horizontally into the ceramic-fiber heater and sealed with insulation strips as needed.

The system pressure on the shell-side was measured by the use of either Swagelok PTU series UHP pressure transducers (0-7 atm) equipped with digital display indicators or Edwards pressure transducers (10000 Torr). The tube-side pressures were monitored by Edwards pressure transducers (1000 Torr). The 1/8" to ¼"stainless steel tubing was used between the pressure transducers and the permeator cells to achieve minimal pressure drop and negligible back-pressure. The flow rate of the shell-side gas was adjusted via needle valve in the range of 20-100 sccm, whereas the tube-side permeate flow was directed to the He and/or H_2 mass flow meters purchased from MKS Instruments of type M100B for He (max flow range 10/50 sccm @ 5V) and for H_2 (max flow range 200/500/1000/5000/20000 sccm @ 5V) with special calibrations. All streams were also separately connected to a vacuum line, equipped with a vacuum pump in order to adjust the zero value for the pressure transducers and mass flow meters. The temperature, pressure and the permeate flow rates of the test system were logged to a computer via data acquisition board purchased from National Instruments and monitored continuously by the use of LabView 7.1 software.

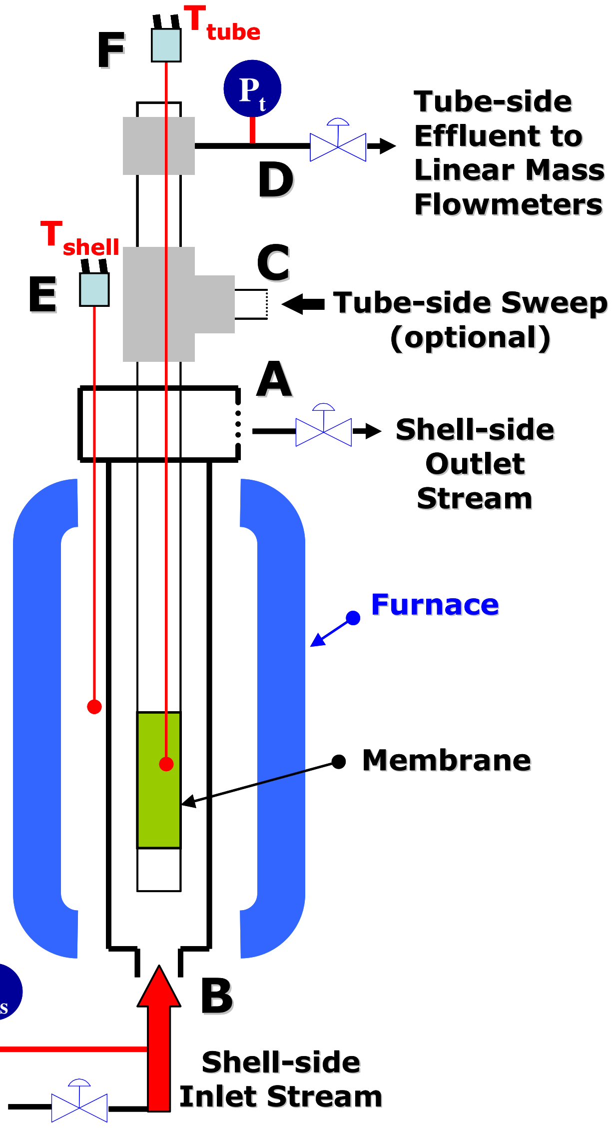

Figure 3-4: H_2 permeation test-rig

3.2.3. H_2 Permeation Test Protocol

Prior to admitting H_2 to the system, the membrane was flushed overnight with helium from both sides at a trans-membrane pressure difference of 1 atm and at room temperature. Following the overnight He flush, the membrane was heated-up to above the critical temperature for α↔β phase transition with a ramp of 0.5°C/min. The helium leak was monitored during the heat-up period. Switching to H_2 was accomplished by the use of 1L and 5L double-ended stainless steel cylinders from the shell-side (B in Figure 3-4) for small and large scale units, respectively. The slow exchange from He to H_2 by the use of mixing volumes are preferred in order to avoid cracking the membrane layer due to sudden concentration changes. Throughout the testing period, permeance data were taken at each temperature and H_2 flux was monitored continuously at various temperatures in order to determine the activation energy for the hydrogen transport. Switching back to helium at the temperature of concern was accomplished by the use of helium sweep line. After the completion of hydrogen removal from the system, temperature was reduced with a ramp of 1°C/min and the He leak was monitored during cooling-down.

3.2.4. Rising Water Test Set-up and Procedure

The rising water test was used for semi-quantitative determination of defects and the distribution of leaks on the surface of the large scale membranes (1” OD, 6” long) after completion of the H_2 permeation testing. The set-up shown in Figure 3-5 and the testing protocol were adopted from the research team at Shell International Exploration and Production Inc., Huston, TX. As can be depicted in Figure 3-5, the composite membrane was placed in a Plexiglas shell by sealing with rubber O rings in such a way that the lower and upper welds of the support assembly corresponded to the “0” and “15” marks on the scale, which was printed on the wall of the Plexiglas casing. A water reservoir connected with Tygon tubing was placed at a higher level and used to admit water through the on/off valve-A. A 3-way valve-B was used for admitting He into the test unit in positions 1 and was open to atmosphere in position 2.

The procedure consisted of gradually increasing the water level at atmospheric pressure over the printed scale while monitoring the He leak through the tube-side via bubble flow meter at a given trans-membrane pressure difference. Since the rising level of the water along the printed scale would clog the surface defects due to capillary forces, the locations of the surface defects can be easily traced by monitoring the changes in the initial He flux of the membrane (position “0”).

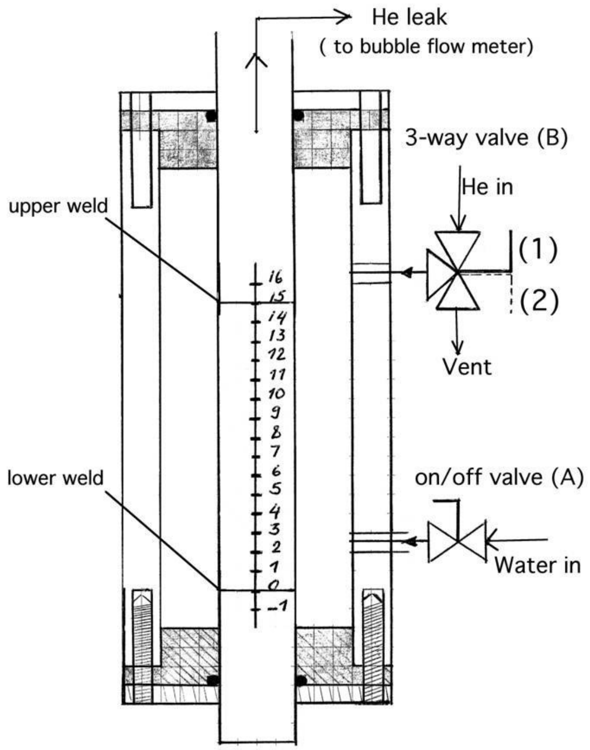

Figure 3-5: Rising H_2O Test Unit (Shell Intl. Exp. & Prod. Inc.)

3.3. Instrumental Analysis and Microstructure Characterization Methods

3.3.1. Sample Preparation for the SEM and EDX Analysis

SEM specimens of the metal deposited porous sintered metal supports were cut using a SiC saw blade and mounted with phenolic powder in a Smithells II mounting press. The resulting samples were ground with SiC papers with increasing grain fineness from 80 to 600 grit. Grinding was performed by using Metaserv 2000 grinder-polisher. Vibromet I automatic polisher was used to polish the sample to 1 μm overnight. Prior to the SEM cross-section analysis, samples were painted with carbon ink and sputter coated using a gold/palladium target to avoid charging.

3.3.2. SEM, EDX, XRD and FT-IR Analyses

Surface characterizations were performed using an Amray 1610 Turbo Scanning Electron Microscope (SEM) equipped with a Princeton Gamma-Tech Avalon EDX light element detector and a RBA-1610 5MC type Robinson Retractable backscattered electron detector for the qualitative and quantitative analysis. The spatial resolution for the EDX analysis of Pd, Ag, Fe, Cr and Ni metals lies between 0.5 to 0.7 μm at an accelerating voltage of 15 keV and between 0.8 to 1.2 μm at an accelerating voltage of 20 keV (Friel, 1998).

The phase identification analyses were carried out by a Rigaku Geigerflex X-ray diffractometer equipped with a CuK_α radiation source and a curved crystal monochromator.

A Perkin Elmer Spectrum One type Fourier transform infrared (FT-IR) spectrometer was used to characterize the structural OH groups of $Al(OH)_3$ powder samples. All the FT-IR measurements were performed in the attenuated total reflectance (ATR) mode for fast sampling and ease of sample preparation without the use of KBr pellets.

3.3.3. *In-situ* Time-Resolved High Temperature X-Ray Diffraction (HTXRD)

The *in-situ* time-resolved high-temperature X-ray diffraction experiments were performed at Oak Ridge National Laboratories (ORNL) using a Scintag PAD-X diffractometer equipped with a vertical θ/θ goniometer, a 2 kW Cu X-ray tube, a Buehler HDK 2.3 furnace, and an *m*Braun linear position sensitive detector (LPSD) as shown in Figure 3-6.

Data acquisition was performed via DMS-NT platform from Scintag Inc. and The integrated peak intensities for the Ag, Pd and Pd/Ag alloy peaks were estimated from the diffraction data using the JADE-6.5 software.

The temperature of the Pt-10%Rh strip heater was measured by an S-type thermocouple, which was welded to the lower surface of the heater. Since the actual surface temperature of the sample was not directly measured, a temperature calibration was carried out by calibrating against the known thermal expansion of silver metal based on the correlation reported by Touloukian *et al.* (1977). The difference between the thermocouple reading and the actual surface temperature investigated by the method of using thermal expansion as a temperature calibration method for HTXRD was in the range of ±1°C.

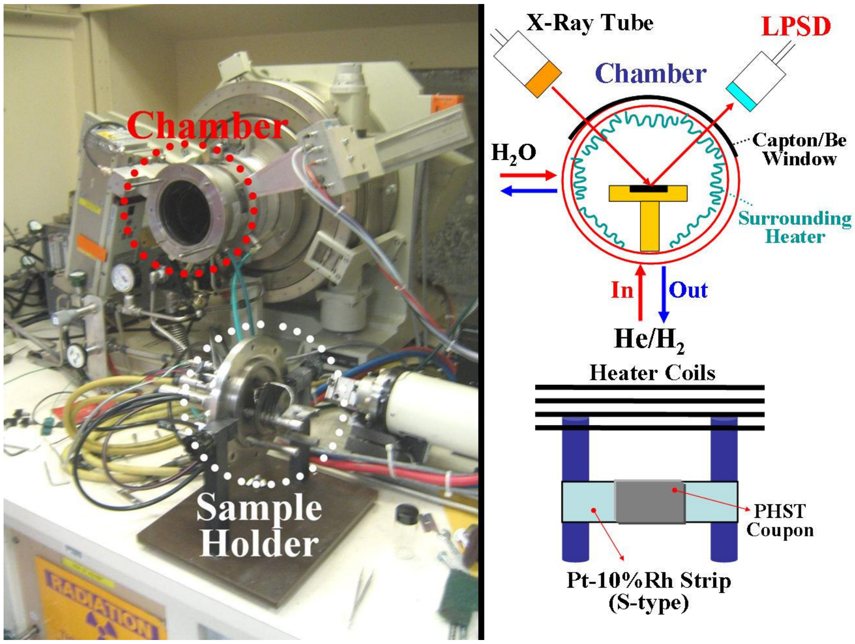

Figure 3-6: Scintag PAD-X HTXRD Set-up

3.3.4. Atomic Absorption Spectroscopy

Perkin Elmer AA3100 atomic absorption spectrometer was used to study the electroless plating kinetics of Pd and Ag metals from hydrazine based plating baths. The experimental set-up for the AA3100 is shown in Figure 3-7. The hollow cathode lamps for Pd (N3050302) and Ag (N3050358) and the single element calibration standards were purchased from Perkin Elmer. An impact bead shown in Figure 3-7[2] was also installed to increase the sensitivity of the analysis. In addition, an air/acetylene filter of type N930-1398 was used to avoid any contamination entering the nebulizer.

The operating conditions used for the measurement of electroless Pd and Ag kinetics via AAS (Perkin Elmer AA3100) are summarized in Table 3-6.

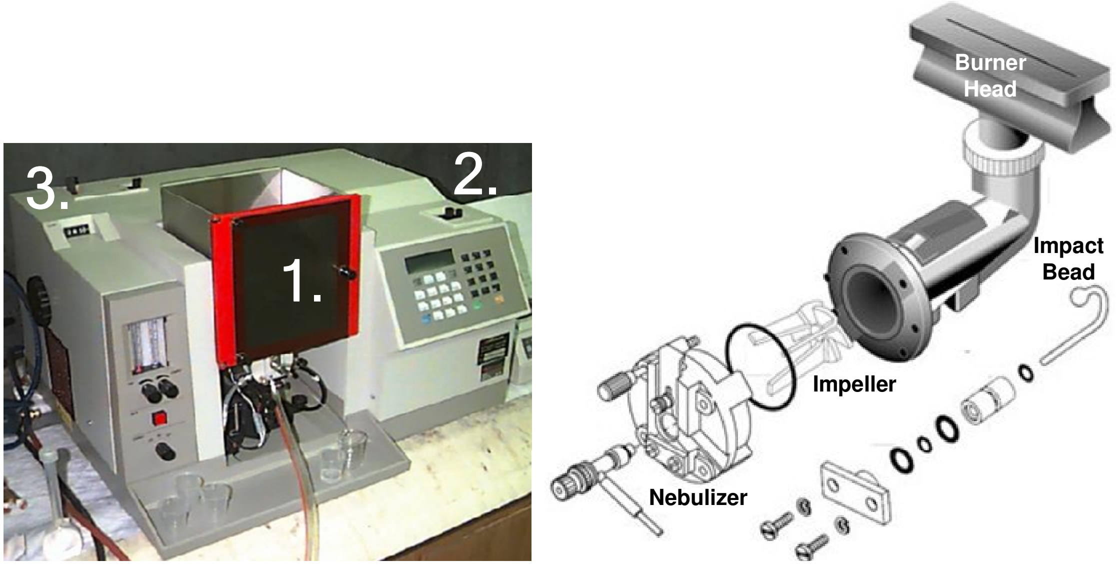

Figure 3-7: Perkin Elmer 3100 Atomic Absorption Spectrometer; [1]. Atomizer, [2]. Light source and [3]. Light separation and detection units

Table 3-6. AA3100 typical operating conditions

	Pd	**Ag**
Burner Head	10 cm	10 cm
C_2H_2-Air Tank Pressures	13-54 psig	13-54 psig
C_2H_2-Air Flowrates	2.5-4 mL/min	2.5-4 mL/min
Lamp Current [0-50 mA]	30 mA	10 mA
Wavelength/Slit Width/Height	244.6nm/0.2/High	328.1nm/0.7/High
Linear Range [mg/L]	0-10 mg/L	0-4 mg/L
Chr. Concn Check [mg/L]	10 mg/L	2.5 mg/L
Integration Time	3 sec.	3 sec.
Repetitions	5	5
Blank/Diluent	DI H_2O	HNO_3 (5% v/v)*

The details on the AA operating principles and the calibration procedures are given in Appendix A.

---

* 5% (v/v) HNO_3 was used as the diluent to keep Ag in solution.

4. Hydrogen Transport through Pd Films and Composite Pd/Alloy Membranes

4.1. Hydrogen Transport Mechanism and the Sieverts' Law

Palladium as a transition metal absorbs hydrogen extensively and forms non-stoichiometric compounds of varying compositions (Graham, 1866). Two hypotheses are postulated in an effort to describe the highly complex nature of hydrogen absorption in Pd and subsequent changes in the structure of the metal lattice. According to Makrides (1964), the Pd-H isotherms can be described either by assuming an attractive interaction between interstitial hydrogen, which exists in the lattice as atoms and/or protons by forming a solid-solution, or an interaction between hydrogen vacancies, in which the existence of vacancies causes the hydride phase of Pd to deviate from stoichiometry. The former solid-solution model for hydrogen interaction, which can be used to predict Pd-H isotherms, is formulated as follows:

$$\ln p = \ln p_0 + 2\ln\frac{\theta}{1-\theta} + \frac{z_i E_{ii}}{k_B T}(1-2\theta) \tag{4-1}$$

Where, p_0 is the pressure of the transition, θ is the fraction of sites occupied by hydrogen, z_i is the number of nearest neighbors for each of the interstitial hydrogen, E_{ii} is the interaction energy for each pair of interstitials, k_B is the Boltzmann constant and T is the temperature in Kelvin. One supportive NMR observation regarding the mobility of hydrogen in Pd at low temperatures strongly suggests that hydrogen in the Pd lattice exists in the form of protons, rather than as firmly-bounded hydride ions (Norberg, 1952). Therefore, the solution-diffusion mechanism or the solid-solution model yields a better explanation on the state of dissolved hydrogen in agreement with numerous experimental observations (Sieverts *et al.*, 1915).

As illustrated schematically in Figure 4-1, hydrogen transport through the Pd metal, based on the solution-diffusion mechanism, is a multi-step process and defined as follows (Sieverts *et al.*, 1915; Shu *et al.*, 1991a; Uemiya *et al.*, 1991a; Wijmans and Baker, 1995):

[1]. Molecular transport from the bulk gas to the gas layer adjacent to the surface

[2]. Reversible dissociative chemisorptions of hydrogen on the membrane surface

[3]. Reversible dissolution of atomic hydrogen from the surface into the bulk metal

[4]. Diffusion of atomic hydrogen through the bulk metal

[5]. Transition from the bulk metal to the surface on the low pressure side

[6]. Recombinative desorption from the surface

[7]. Molecular transport from the surface to the bulk gas

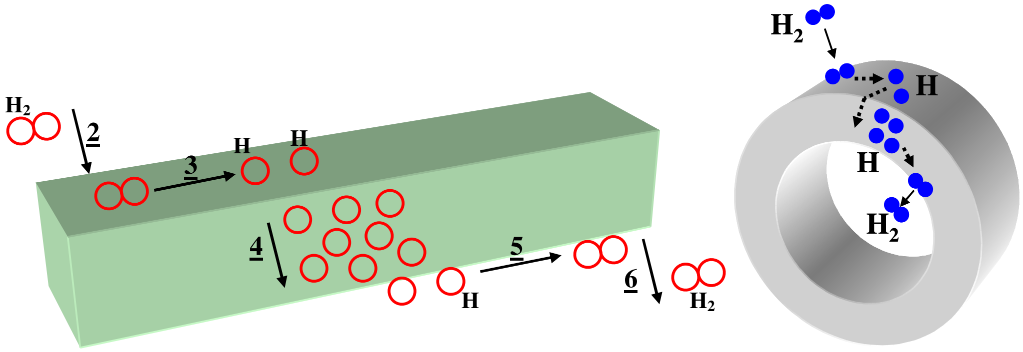

Figure 4-1: The solution-diffusion mechanism

The hydrogen permeation flux for the reversible dissociative chemisorption, $H_2 + 2\sigma \leftrightarrow 2H\sigma$[*] in step [2], is expressed as the difference between desorption and absorption rates as shown in Equation (4-2):

$$J_{H_2} = -k_a P_{H_2}(1-\theta)^2 + k_d\theta^2 \qquad \textit{(4-2)}$$

where J_{H_2} is the hydrogen permeation flux in mol/m^2-s, P_{H_2} is the partial pressure of hydrogen, θ is the surface coverage with the absorption and desorption rate constants k_a and k_d, respectively (Shu *et al.*, 1991a). For the reversible dissolution of atomic hydrogen in step [3], the flux at the dissolution interface is given by Equation (4-3):

$$J_{H_2} = k_0 n(1-\theta) - k_i(1-n)\theta \qquad \textit{(4-3)}$$

where n is the atomic H/Pd ratio, with k_0 and k_i as the rate constants of dissolution and its reverse step, respectively. Assuming steps [1] to [3] and [5] to [7] are in equilibrium, the bulk diffusion of hydrogen in Pd, step [4], becomes the rate-controlling step. Then, the hydrogen permeation flux, at steady state, is obtained via integration of Fick's first law of diffusion:

$$J_{H_2} = \frac{D_H}{L}\left(C_{H_2,h} - C_{H_2,l}\right) \qquad \textit{(4-4)}$$

where D_H is the diffusivity of hydrogen in Pd in m^2/s, L is the thickness of the Pd layer in m, and C is the concentration of hydrogen in mol/m^3, at the high and low pressure sides of the membrane and related to the concentration of the hydrogen atom in the bulk of Pd according to the following formulation:

$$C = \kappa n \qquad \textit{(4-5)}$$

where, n is the atomic H/Pd ratio and κ is the hydrogen concentration constant in mol/m^3. Since forward and reverse reaction rates are equal at equilibrium, the net flux for Equations (4-2) and (4-3) is zero and leads to the following relationship under the hypothesis $n \ll 1$:

---

[*] σ denotes the vacancy on the membrane surface

$$K_S = \frac{k_0}{k_i}\left(\frac{k_d}{k_a}\right)^{0.5} \qquad (4\text{-}6)$$

where K_S is the equilibrium constant for the dissolution of atomic hydrogen in step [3] in atm$^{0.5}$, which is also known as the Sieverts' constant as shown in Equation (4-7):

$$K_S = \frac{P_{H_2}^{0.5}}{n} \qquad (4\text{-}7)$$

Equation (4-7) is very similar to Henry's law and only valid for very low values of n, which corresponds to the α-phase in the Pd-H phase diagram, shown in Figure 2-1, at very low pressures. By substituting Equations (4-5) and (4-7) into Equation (4-4), the derivation of the so-called "Sieverts' law" is achieved, which states that the H_2 permeation flux is inversely proportional to the thickness of the Pd layer, directly proportional to the difference of the square roots of the hydrogen partial pressures.

$$J_{H_2} = \frac{D_H \kappa}{L K_S}\left(P_{H_2,h}^{0.5} - P_{H_2,l}^{0.5}\right) \qquad (4\text{-}8)$$

Since κ is constant and D_H and K_S are temperature dependent, the term $\frac{D_H \kappa}{K_S}$ in Equation (4-8) is defined as the permeability, Q_H in kmol-m/m^2-s-atm$^{0.5}$. Furthermore, $\frac{\kappa}{K_S}$ is defined as the hydrogen solubility, S_H, in kmol/m^3. Hence, Equation (4-8) can be expressed as follows:

$$J_{H_2} = \frac{D_H S_H}{L}\left(P_{H_2,h}^{0.5} - P_{H_2,l}^{0.5}\right) = \frac{Q_H}{L}\left(P_{H_2,h}^{0.5} - P_{H_2,l}^{0.5}\right) \qquad (4\text{-}9)$$

The term $\frac{Q_H}{L}$ in Equation (4-9) is also known as the hydrogen permeance in kmol/m^2-s-atm$^{0.5}$. By defining D_H and S_H in Arrhenius form, we have:

$$D_H = D_0 \exp\left(-\frac{E_d}{RT}\right) \tag{4-10}$$

$$S_H = S_0 \exp\left(-\frac{\Delta H_s}{RT}\right) \tag{4-11}$$

Similarly, permeability, Q_H, and the associated activation energy, E_a, are given as:

$$Q_H = Q_0 \exp\left(-\frac{E_a}{RT}\right) \tag{4-12}$$

$$E_a = E_d + \Delta H_s \tag{4-13}$$

where Q_0 is the pre-exponential or frequency factor, E_d is the activation energy for hydrogen diffusion in J/mol, ΔH_s is the enthalpy of absorption and/or solubility of hydrogen in Pd in J/mol, R is the universal gas constant in J/mol-K and T is the temperature in Kelvin.

4.2. H_2 Diffusivity, Solubility and Permeability in Pd and Pd/Ag Alloy Foils

Due to its pertinence to the understanding of the transport process, diffusivity, solubility and permeability of hydrogen in Pd and Pd/alloy foils have been studied in detail by volumetric gas diffusion measurements, potentiostatic techniques, dilatometric and/or electrochemical methods (Hurlbert and Konecny, 1961; Makrides, 1964; Holleck, 1970; Völkl and Alefeld, 1978; Sakamoto *et al.*, 1982; Latyshev and Gur'yanov, 1988; Bucur, 1991; Schober and Stoneham, 1991; Sakamoto *et al.*, 1995; Li and Cheng, 1996; Serra *et al.*, 1998) and theoretically via Monte Carlo and DFT calculations (Ke and Kramer, 2002; Kamakoti and Sholl, 2003; Kurokawa *et al.*, 2003; Kamakoti *et al.*, 2005; Sonwane *et al.*, 2006b, 2006a).

The solubility of hydrogen in Pd/Ag alloys has not been studied in detail compared to that of Pd (Balovnev, 1974; Latyshev and Bystritskiy, 1991; Latyshev *et al.*, 1991; Hermann *et al.*, 1997). On the other hand, the diffusivity of hydrogen in Pd has been investigated systematically over a wide temperature and pressure ranges, showing a relatively noticeable consistency as shown in Figure 4-2 (Lewis, 1967; Holleck, 1970;

Birnbaum and West, 1972; Balovnev, 1974; Völkl and Alefeld, 1978; Latyshev *et al.*, 1991; Hermann *et al.*, 1997; Mardilovich *et al.*, 1998a).

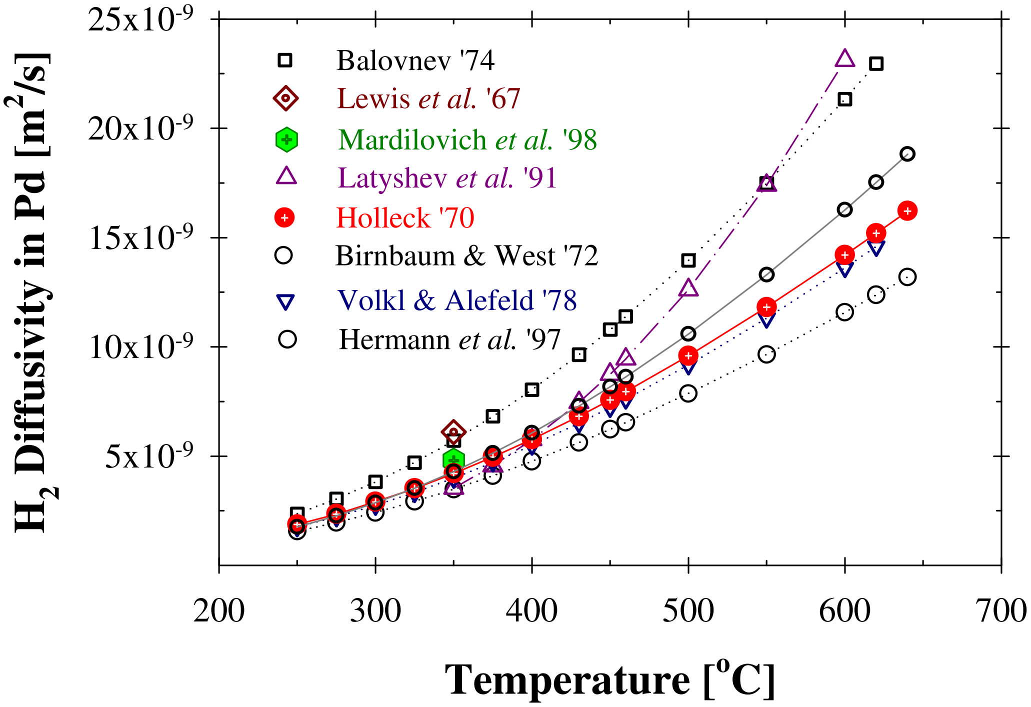

Figure 4-2: Diffusivity of hydrogen in Pd

It should be noted that the hydrogen diffusivity values reported by Birnbaum and West (1972) and Volkl and Alefeld (1978), shown in Figure 4-2, are the average values that stem from a linear regression based on the results of 11 and 25 different researchers, respectively (Shu *et al.*, 1991a).

As shown in Figure 4-3, the diffusivity of hydrogen in Pd/Ag alloys has been studied over a temperature range of 260-640°C and varying Ag content (10-50 wt% Ag) by Holleck (1970) and for a Pd/Ag alloy (25 wt% Ag) by Jeema *et al.* (1995) at a relatively lower temperature range of 100-250°C. In agreement with the discussion on the Pd-Alloy-H systems in Section 2.2, the diffusivity of hydrogen decreases with the increase in Ag content of the Pd/Ag alloy (Figure 4-3).

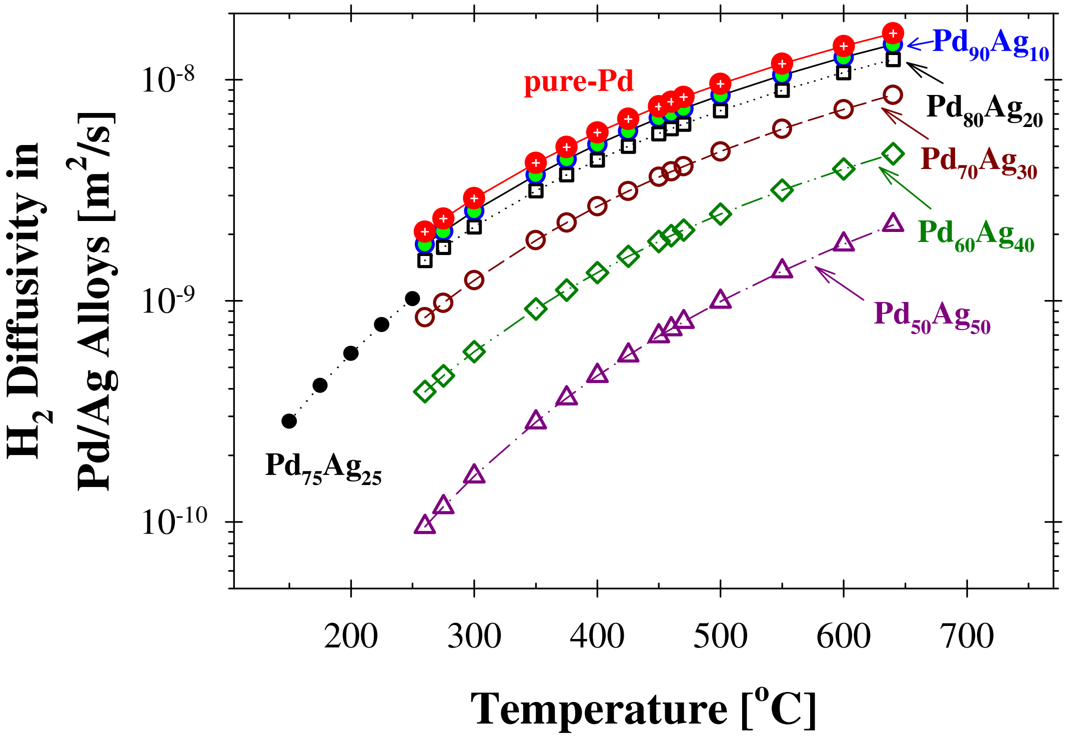

Figure 4-3: Diffusivity of hydrogen in Pd/Ag alloys (Holleck, 1970; Jeema et al., 1995)

Based on the data shown in Figure 4-3, Holleck (1970) further showed that the activation energy for the diffusion of hydrogen in the bulk of the Pd/Ag alloys increased in the order of 22.2, 22.3, 23.5, 24.7, 26.4 and 33.5 kJ/mol with the increasing Ag concentration as 10, 20, 25, 30, 40 and 50 wt% Ag, respectively. In fact, Holleck's (1970) observation is of great importance in order to reckon the effect of Ag content on the hydrogen permeability of Pd/Ag alloys.

According to Makrides (1964), the heat of absorption of hydrogen at different sites in Pd/Ag alloys would differ, since sites that had greater number of nearest neighbor Ag atoms would absorb more heat based on the existence of additive pair of attractive interaction for the Pd/Ag system. Makrides (1964) further stated that the various sites should be distributed randomly since Pd/Ag alloys were random solid solutions, which exert complete miscibility both in solid and liquid phases. Ke and Kramer (2002) have studied the vibrational-states absorption energies and diffusion of hydrogen atom in PdH_x (x=0.03125, 0.0625, 0.25, 0.5, 0.75 and 1) and $Pd_{(1-x)}Ag_x$ (x=0, 0.25, 0.5, 0.75 and 1) systems by the DFT calculations and reported that the absorption energies of H in the octahedral sites of $PdH_{0.25}$ were smaller than that of the octahedral sites of $Pd_{0.75}Ag_{0.25}H_{0.25}$, which was in excellent agreement with the hypothesis of Makrides (1964). Indeed, a significant decrease in the calculated energies when $x \geq 0.5$ indicated the fact that the solubility of H in Pd/Ag alloys was lower at high Ag concentrations. In contrary to the $PdH_{0.5}$ system, Ke and Kramer (2002) have also observed a significant deviation in the diffusion path of H atom from the [111] direction in the case of $Pd_{0.75}Ag_{0.25}H_{0.25}$ alloy and concluded that the diffusion of hydrogen through the Ag-rich regions was strongly blocked.

Avdjukhina *et al.* (2002) have studied the structural changes and phase transformation kinetics in Pd-H and Pd-Ag-H systems during relaxation processes as hydrogen was released. For the Pd-Ag-H system, they have reported that the structural phase change kinetics were relatively oscillatory due to the non-homogeneous distributions of the alloying metal and the associated non-homogeneous hydrogen distribution. Avdjukhina *et al.* (2002) have also noted that the non-homogeneous distribution have further facilitated hydrogen capture by the regions that had a high bonding energy for hydrogen and kept the system in a non-equilibrium state. Avdjukhina *et al.*'s (2002) observations were in good agreement with the findings of Kurokawa *et al.* (2003), who have simulated H_2 absorption in Pd and Pd/Ag alloys (20-30 wt%) at 1 atm and over a temperature range of 200-500°C using Monte Carlo techniques. Kurokawa *et al.* (2003) have shown that the distribution of hydrogen in Pd/Ag alloys was disordered due to the presence of Ag occupying energetically higher tetrahedral sites, as opposed to the ordered distribution of hydrogen at the energetically lower octahedral sites of Pd. It was also interesting to note that the nearest distance between the Ag-H was shorter with respect to that of Pd-H, indicating that even the hydrogen atom in contact with the Ag atom might occupy the energetically higher tetrahedral sites, which might lead the system to a non-equilibrium state, as suggested by Avdjukhina *et al.* (2002).

In addition to the aforementioned research on the hydrogen diffusivity, the permeability of hydrogen has also been investigated extensively for Pd foils (Davis, 1954; Toda, 1958; Koffler *et al.*, 1969; Balovnev, 1974; Hermann *et al.*, 1997; Morreale *et al.*, 2004) and relatively in a narrow range for the Pd/Ag alloy foils (Holleck, 1970;

Ackerman and Koskinas, 1972; Latyshev and Bystritskiy, 1991; Jeema *et al.*, 1995) as listed in Table 4-1.

Table 4-1. Data for H_2 permeability in Pd and Pd/Ag alloy foils

References	Foil	Q_o [m^3-μm/m^2-h-$atm^{0.5}$]	E_a [kJ/mol]	Temp. [°C]	Pressure [atm]
Koffler *et al.* (1969)	Pd	5.69×10^{-3}	15.69	27-436	4×10^{-7}-7×10^{-5}
Toda (1958)	Pd	4.46×10^{-3}	13.49	170-290	0.05-0.85
Davis (1954)	Pd	9.95×10^{-3}	18.60	200-700	3×10^{-5}-1.0
Balovnev (1974)	Pd	6.63×10^{-3}	15.50	100-620	3×10^{-10}-7×10^{-7}
Morreale *et al.* (2003)	Pd	4.93×10^{-3}	13.81	350-900	1-27.9
Latyshev & Bystritskiy (1991)	$Pd_{85}Ag_{15}$	8.48×10^{-3}	18.27	300-700	0-0.1
Ackerman & Koskinas (1972)	$Pd_{75}Ag_{25}$	1.98×10^{-3}	794†	300-500	1.1-68.9

The hydrogen permeability of Pd foils within the temperature range listed in Table 4-1 was plotted using Equation (4-12) in the Arrhenius form as shown in Figure 4-4. The pre-exponential factor, Q_0 and the activation energy, E_a, for the average H_2 permeability were determined via linear regression analysis as 6322.7 m^3-μm/m^2-h-$atm^{0.5}$ and 15.63 kJ/mol, respectively and led to the following expression for the average H_2 permeability of hydrogen in Pd foils:

$$Q_{Pd}(T) = Q_0 e^{-\frac{E_a}{RT}} = 6322.7 e^{-\frac{15630}{RT}} \tag{4-14}$$

The average H_2 permeability for Pd in Equation (4-14) approximates the reported H_2 permeability data (Table 4-1) within an error of ±16%. Similar analysis reported by Guazzone (2005) for the estimation of an average H_2 permeability expression, gave an error margin of 30% due to the temperature interval used for the calculations.

---

† Units in Kelvin

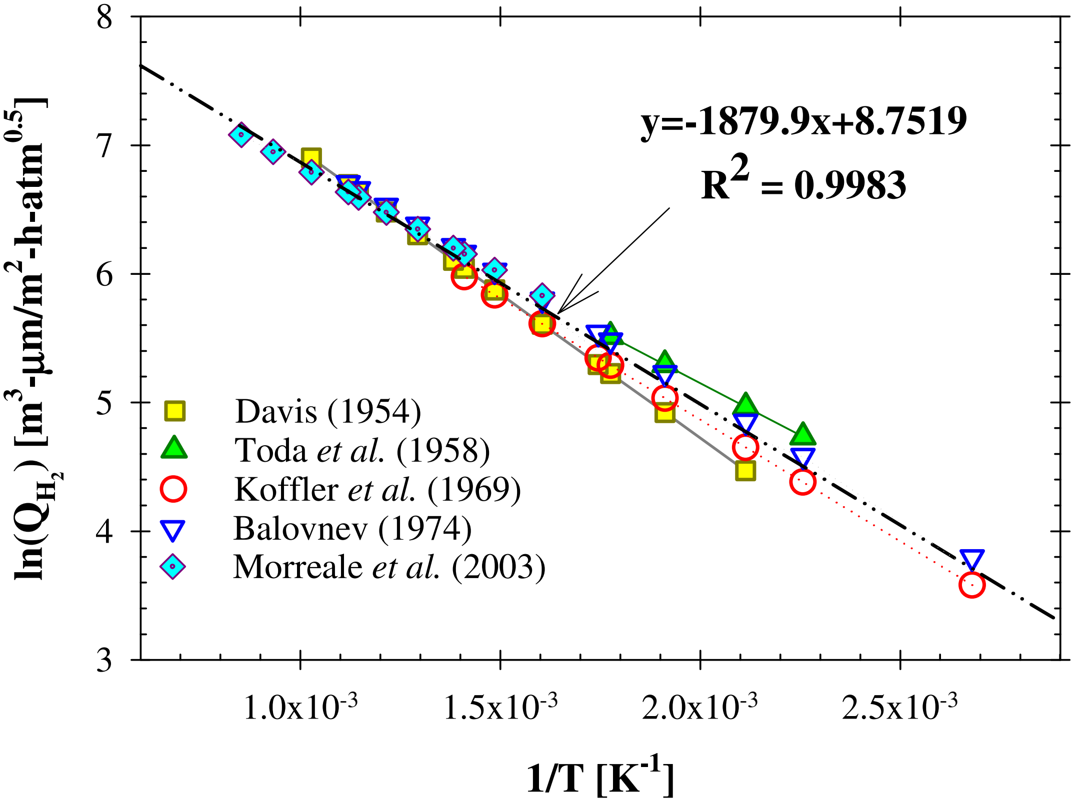

Figure 4-4: Arrhenius plot of Equation (4-12) based on the literature data listed in Table 4-1 for the estimation of an average H_2 permeability for Pd foils

The hydrogen permeability of Pd/Ag alloy foils listed in Table 4-1 were plotted using Equation (4-12) in the Arrhenius form as shown in Figure 4-5. No regression analysis were performed to estimate an average H_2 permeability expression for the Pd/Ag alloy foils due to the limited number of data points. Nonetheless, the permeability data reported by Ackerman and Koskinas (1972) and Latyshev and Bystritskiy (1991) were compared with the data from Knapton (1977) and Shu *et al.* (1991a) as shown in Figure 4-6.

The H_2 permeability for the Pd/Ag alloy (25 wt% Ag) reported by Ackerman and Koskinas (1972) was 1.8 times higher than that of pure Pd, whereas the normalized H_2 permeability for the Pd/Ag alloy (15 wt% Ag) reported by Latyshev and Bystritskiy (1991) fell well below the general trend shown in Figure 4-6. However, it should be noted that, neither Knapton (1977) nor Shu *et al.* (1991a) have previously reported permeability data for a 15 wt% Ag alloy.

The average H_2 permeability given in Equation (4-14) can be of great use for the direct comparison of the membrane performance for a Pd layer supported on a porous support to that of Pd foils at a given temperature. Please see Appendix B for further illustration.

For H_2 transport through composite Pd and Pd/alloy membranes, Appendix B also includes a brief discussion on the effect of external mass transfer resistance exerted by the supports.

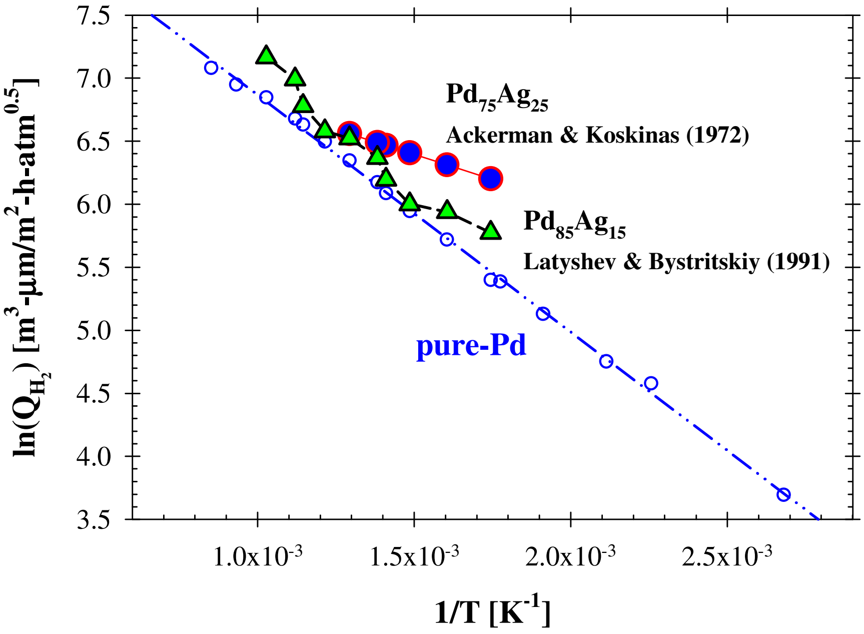

Figure 4-5: Arrhenius plot of Equation (4-12) based on the literature data listed in Table 4-1 for the estimation of an average H_2 permeability for Pd/Ag foils

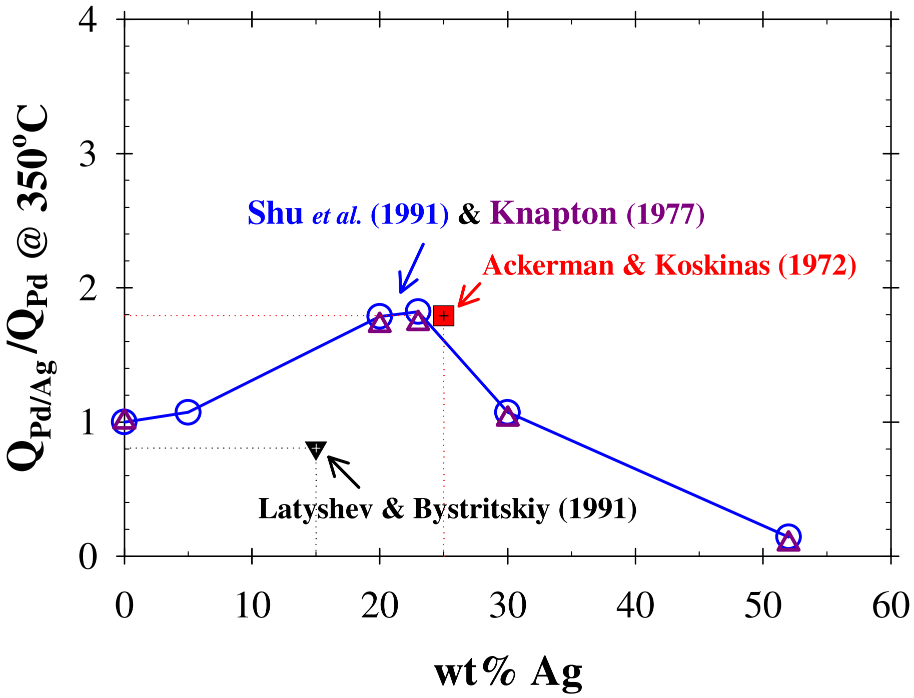

Figure 4-6: Summary of the normalized permeability for the Pd/Ag alloy foils listed in Table 4-1

5. Synthesis of the Pd/Ag Intermetallic Diffusion Barrier via Bi-Metal Multi-Layer (BMML) Deposition Technique

5.1. Introduction

The intermetallic diffusion of support elements (Fe, Cr and Ni) into the dense Pd and Pd/alloy membrane layer during high temperature hydrogen separation applications results in the deterioration of the hydrogen permeation flux, which is a key factor limiting the long-term stability of Pd and Pd/alloy membranes supported on porous sintered metals. By the use of the porous Pd/Ag barrier layer formed via the bi-metal multi-layer (BMML) deposition technique developed by Ma *et al.* (2007) in our group, the most significant improvement in membrane performance has been the increase in the safe operational temperature of the composite Pd/PSS and Pd/Alloy/PSS membranes at 500°C or above (Ma *et al.*, 2004b; Mardilovich *et al.*, 2006; Ma *et al.*, 2007).

Therefore, the main objective of this chapter is to provide a detailed microstructure characterization study and a better understanding of the fundamental principles involved in the synthesis of a novel Pd/Ag intermetallic diffusion barrier formed by the BMML and to investigate its effectiveness as a barrier layer against intermetallic diffusion.

5.2. Bi-Metal Multi-Layer (BMML) Deposition Technique

PSS plates used in this study were prepared by cutting 1 dm^2 0.5 μm media grade PSS-316L sheets into 1 cm^2 pieces. The dimensions of the 0.1 μm, 0.2 μm and 0.5 μm grade PSS-316L cylindrical cups were 2.54 cm and 5.08 cm long and 1.27 cm in OD with a wall thickness of 0.16 cm. Cups were sealed at one end with a blind end cap and welded to a non-porous stainless steel tube on the other end as shown in Figure 3-1. PSS supports were cleaned before activation and electroless deposition of metals, according to the procedure outlined in Section 3.1.2. All cleaning steps were carried out in ultrasonic bath at 60°C. The supports were finally dried at 120°C for 2 to 4 hours and then weighed. The helium flux was measured for the tube assemblies at different pressures to determine the room temperature He permeance of the bare support. Solutions for the surface activation of the supports were prepared using the chemical compositions listed in Table 3-2. The $SnCl_2$-$PdCl_2$ activation cycle was usually repeated for 3 to 6 times according to the procedure discussed in 3.1.3. After activation Pd and Ag were deposited using the bath compositions shown in Table 3-4.

The intermetallic diffusion barrier of PSS supports were prepared by the bi-metal multi-layer (BMML) deposition technique (Ma *et al.*, 2000), which involved the formation of a porous Pd/Ag composite layer by consecutive deposition of Pd and Ag layers with no intermediate surface activation, drying and sintering. While the conventional electroless plating involved intermediate drying and activating steps between Pd and Ag depositions, the BMML deposition provided continuous plating with alternating Pd and Ag baths to obtain the porous Pd/Ag/Pd/…/Ag/Pd structure (Ayturk *et al.*, 2004b; Ma *et al.*, 2004a; Mardilovich *et al.*, 2006; Ma *et al.*, 2007). The final modified support was washed and dried overnight at 120°C. The synthesis of these membranes involved a finishing step of the application of a gas tight Pd layer upon the BMML to produce a dense membrane. The BMML deposition process is graphically depicted in Figure 5-1.

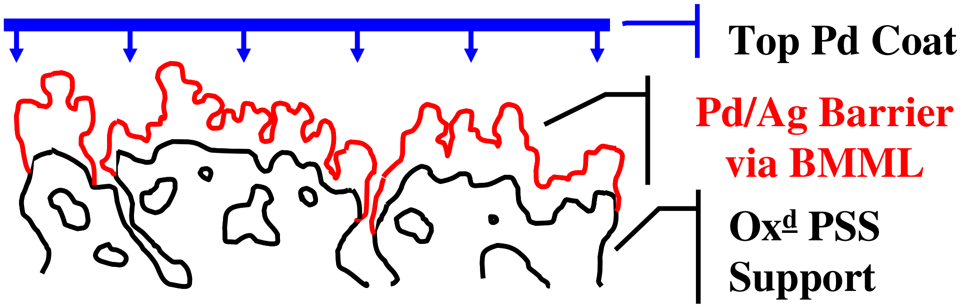

Figure 5-1: Pd/Ag barrier layer formation via BMML deposition technique

The transition between the plating of the porous layer and the plating of the dense hydrogen selective layer was facilitated by an extremely mild mechanical treatment on the surface of the porous "powder like" layer. This could be accomplished by brushing the surface with a plastic bristle brush having a tooth brush like consistency, or gentle polishing with an extremely fine emery cloth. The membranes were considered to be dense (termed He dense) when the He flux was undetectable at room temperature under a pressure difference of 1 bar. The thickness of the deposited metals was determined gravimetrically using Equation (3-2), where surface characterization, phase identification and hydrogen permeation measurements were carried out according to experimental procedures described in Sections 3.2 and 3.3.

5.3. Results and Discussion

5.3.1. Pd/Ag Intermetallic Diffusion Barrier and Membrane Stability

The rate of the intermetallic diffusion between different metal atoms becomes significant at high temperatures, in which the diffusion of components from the porous metal substrate into the Pd or Pd/Alloy hydrogen separation layer causes the deterioration of the hydrogen permeation flux. The unique concept of making an additional intermetallic protection layer on top of the protection layer produced by the controlled *in-situ* oxidation technique (Ma *et al.*, 2000), consists of the synthesis of nanosize particles of Pd and a second metal (e.g., Pd/Ag for Pd or Pd-Ag membranes) to form a porous Pd/Ag layer as the intermetallic diffusion barrier via BMML deposition technique (Ayturk *et al.*, 2004b; Ma *et al.*, 2004a; Mardilovich *et al.*, 2006; Ma *et al.*, 2007). The preparation conditions and the properties of the membranes used in this study are summarized in Table 5-1.

Table 5-1. The preparation conditions and the properties of the 1.27 cm OD cups

Membrane	001	002	011
Support	0.5 μm-PSS	0.1 μm-PSS	0.2 μm-PSS
Oxidation	400°C/Air/6h	400°C/Air/6h	600°C/Air/12h
Synthesis Type	Pure Pd (Regular)	Pd/Ag Barrier (BMML)	Pure Pd (Regular)
Thickness (μm)	23	84.6	72.2

The plot for the hydrogen permeance given in Figure 5-2 highlights the importance and necessity of intermetallic diffusion barriers for pure Pd and/or Pd/Alloy membranes.

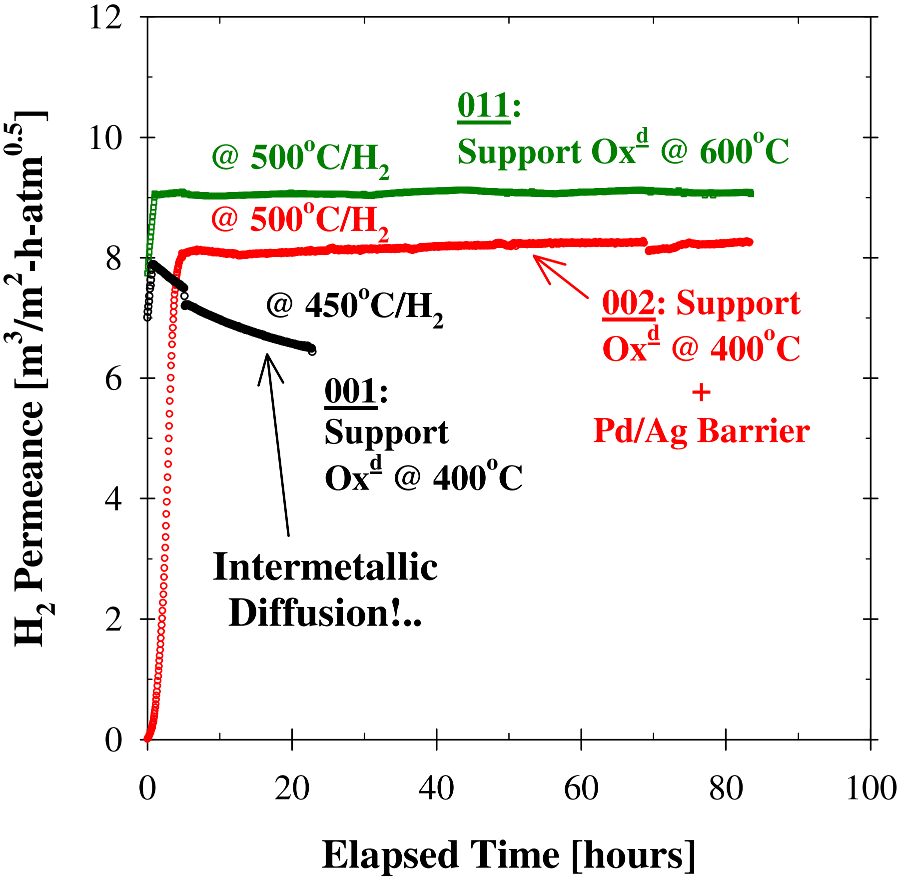

Figure 5-2: Stability benchmark for the pure Pd membranes

The membranes 001 and 011 shown in Figure 5-2 were pure Pd membranes on 0.5 μm and 0.2 μm media grade PSS supports, respectively. The PSS support used for the fabrication of membrane 002 was 0.1 μm media grade. Membrane 002 has a dense selective pure Pd coat on the top of a Pd/Ag barrier layer. In addition to the general Pd/Ag barrier synthesis routine, the Pd/Ag barrier layer for membrane 002 was annealed at 600°C under helium atmosphere for 20 hours prior to further Pd plating. The *in-situ* oxidation conditions for the PSS supports of membranes 001, 002 and 011 were 400°C/Air/6h, 400°C/Air/6h and 600°C/Air/12h, respectively.

The hydrogen permeance at 500°C for the membrane 011, which had an oxide-barrier formed at 600°C, was highly stable with a hydrogen permeance of 9 m^3/m^2-h-$atm^{0.5}$ over 80 hours. However, the hydrogen permeance taken at 450°C for the membrane 001, which had an oxide barrier formed at 400°C, showed a steady decline from 8 to 6.5 m^3/m^2-h-$atm^{0.5}$, within the first 24 hours of permeation testing. The deterioration in hydrogen permeance at 450°C, which corresponded to the ~20% of the original permeance of this membrane, was attributed to the intermetallic diffusion of the support elements (Fe, Ni and Cr) into the dense and selective Pd layer. The helium flux of membrane 001 was not detectable at 450°C.

On the other hand, membrane 002, which has a Pd/Ag barrier layer, prepared via the BMML deposition technique, between the *in-situ* oxidation layer and the dense Pd layer, produced a highly stable hydrogen permeance of ~8.2 m^3/m^2-h-$atm^{0.5}$ at 500°C for several hundreds of hours. The permeance data for membrane 002 in Figure 5-2 shows only the initial testing period of first 90 hours. The H_2/He selectivity for membrane 002 at 500°C was ~1375.

The effectiveness of the oxide layer to minimize the intermetallic diffusion is a function of its thickness and more importantly, of the nature of the oxide at the surface of the support (Guazzone *et al.*, 2004). As discussed in detail by Guazzone *et al.* (2004), oxidizing at 600°C in stagnant air led to a thin (0.5-0.8 μm) oxide layer consisted of a stable chromium oxide layer (0.1-0.2 μm) and an iron oxide layer on top (0.4-0.6 μm). Indeed, EDX analyses showed that the iron-oxide rich top layer might get reduced at temperatures above 400°C, in which the reduced Fe might readily diffuse into the Pd layer. Ma *et al.* (2004a) have reported a similar structure with a very thick iron oxide layer on the top of the chromium oxide for oxide layers formed at 800ºC. Although oxidation at high temperatures forms an effective intermetallic diffusion barrier (i.e., Membrane 011 in Figure 5-2), a significant loss of the room temperature helium permeability of the support, indicating a partial blockage of the pore system, is not preferred for practical purposes. In this respect, the Pd/Ag barrier layer formed by the BMML procedure not only provides additional thermal stability and resistance against intermetallic diffusion at high temperature hydrogen permeation conditions (Mardilovich *et al.*, 2006), but also avoids a highly energy intensive synthesis step of the oxidation of the support at high temperatures.

The Sieverts law plots for the membranes 002 and 011 are given in Figure 5-3. As can be depicted from the straight line relationship given in Figure 5-3, the diffusion of hydrogen through the dense Pd layer was the rate determining step.

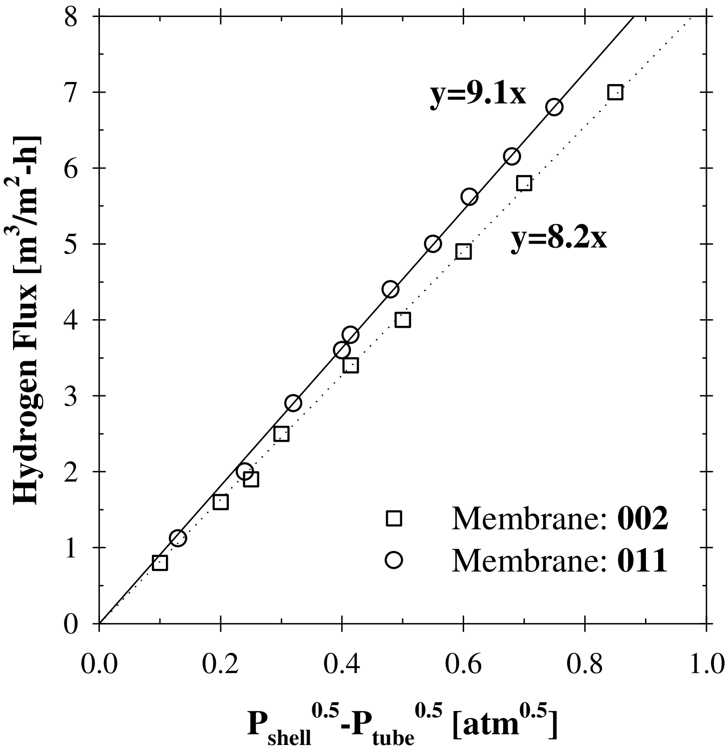

Figure 5-3: Sieverts law plot for the membranes 002 and 011 at 500°C

The thermal stability of the Pd/Ag barrier layer for membrane 002 produced via the Bi-Metal Multi-Layer (BMML) deposition technique was further tested up to a temperature of 600°C as shown in Figure 5-4.

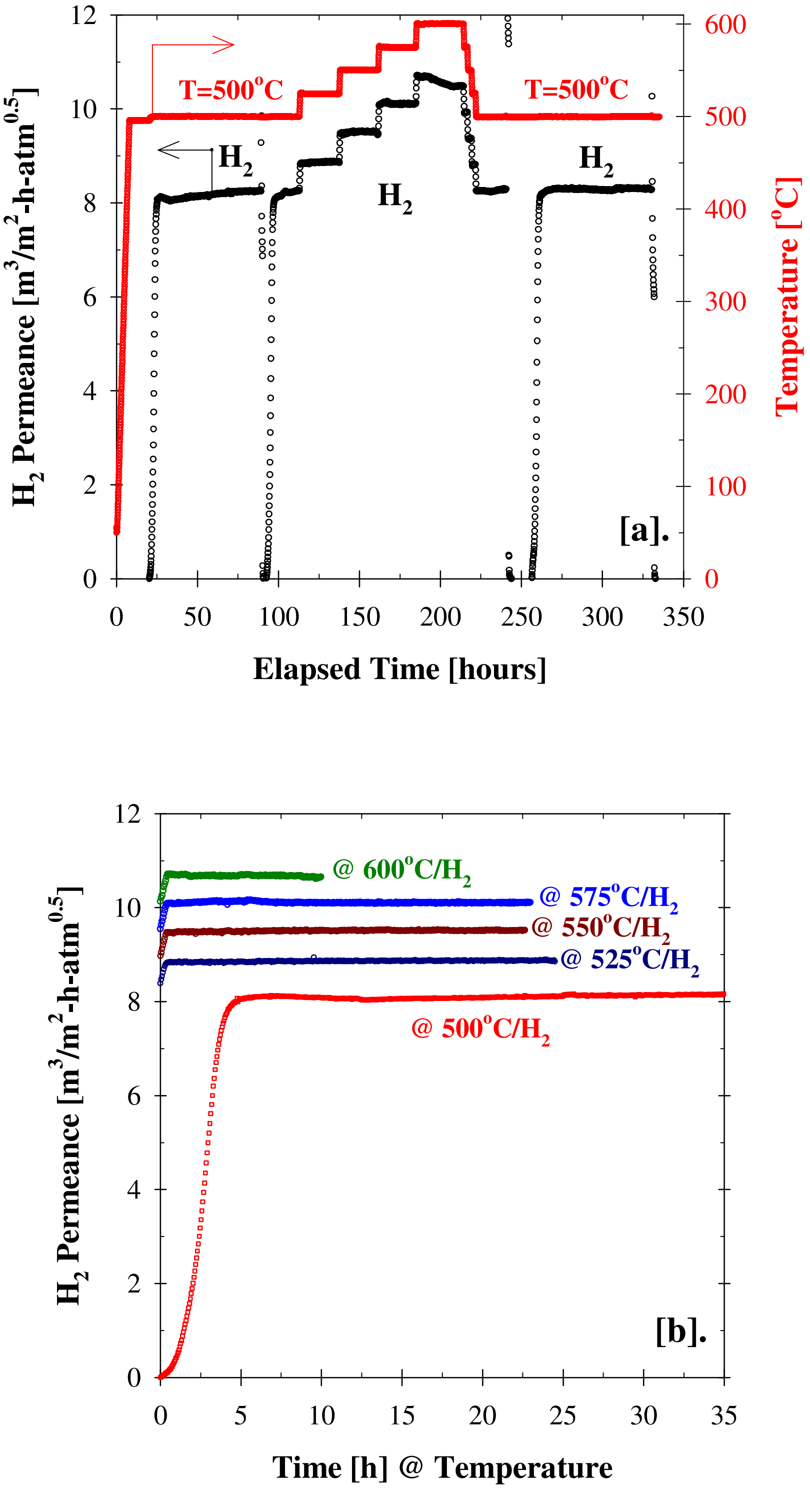

Figure 5-4: Thermal stability of the Pd/Ag intermetallic diffusion barrier [a]. H_2 permeance history, [b]. Temperature increment (25 °C/step)

As can be depicted from Figure 5-4[a], the membrane 002 showed a stable hydrogen permeance at 500°C both before and after the temperature increments between 90 and 240 hours) that was extended to a temperature of 600°C. The re-plotting of the performed heating and cooling sequence between temperatures 500°C and 600°C, which consisted of temperature increments of 25°C, is shown in Figure 5-4[b]. It should be noted that the zero-point on the x-axis of Figure 5-4[b] represents the temperature change.

The results presented in Figure 5-2 and Figure 5-3 showed that the Pd/Ag barrier layer prepared by the BMML deposition technique formed an extremely effective intermetallic diffusion barrier between the metal support and the dense and hydrogen selective Pd layer. Indeed, these results are of great importance and quite promising for the membrane reactor applications of steam reforming reactions.

5.3.2. Microstructure Analysis of the Pd/Ag Barrier Layer

A detailed microstructure analysis was performed in order to improve our understanding on the resulting stability performances of membranes having Pd/Ag barrier layers. For this purpose, the BMML deposition sequence of Pd/Ag/Pd/Ag/Pd (Each electroless Pd and Ag plating experiments consisted of 30 and 90 minutes, respectively) was carried out on 0.5 μm media grade The PSS coupons. PSS coupons were oxidized at 400°C/Air/6h prior to the activation and BMML deposition steps. The typical deposition morphology of the Pd/Ag barrier layer is given in Figure 5-5[b] and Figure 5-4[c] with Figure 5-5[a] showing the 0.5 μm media grade blank PSS support.

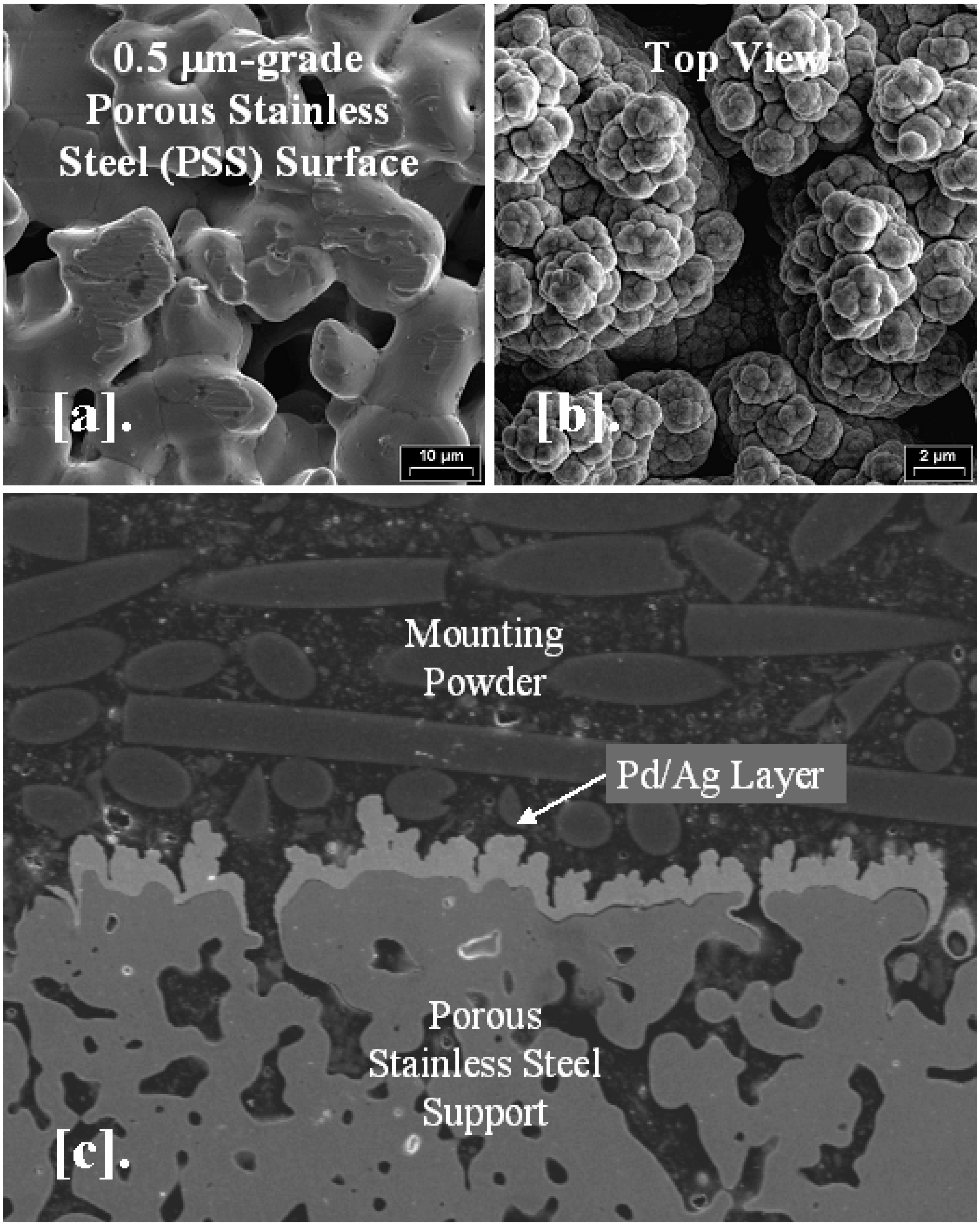

Figure 5-5: SEI Micrographs for the typical deposition morphology of the Pd/Ag Barrier Layer: [a]. 0.5 μm grade blank PSS support, [b]. Top view of the Pd/Ag Barrier Layer, [c]. Cross-section view of the Pd/Ag Barrier Layer

As can be depicted from the SEI micrograph in Figure 5-5[a], the maximum pore size on the PSS support surface can be as high as 15-20 μm. On the other hand, the largest detectable pore of the Pd/Ag barrier layer shown in Figure 5-5[b] was smaller within 2 to 4 μm range. The top-view SEI micrograph in Figure 5-5[b] also indicated that the Pd/Ag barrier layer was porous. The cross-section SEI micrograph shown in Figure 5-5[c] further showed that there was a significant narrowing at the regions closer to the pore mouths and corresponding valleys of the PSS support. Figure 5-6 shows the BMML deposition morphology of the Pd/Ag barrier layer on a non-porous stainless steel support. The high magnification SEI micrograph (10 kX) in Figure 5-6 clearly verifies the porosity of the Pd/Ag barrier layer formed by the BMML deposition. In addition to the typical Pd/Ag clusters within 2 to 4 µm range, Figure 5-6 further reveals that the porous Pd/Ag layer was comprised of nanosized grains, which were distributed uniformly over the entire surface.

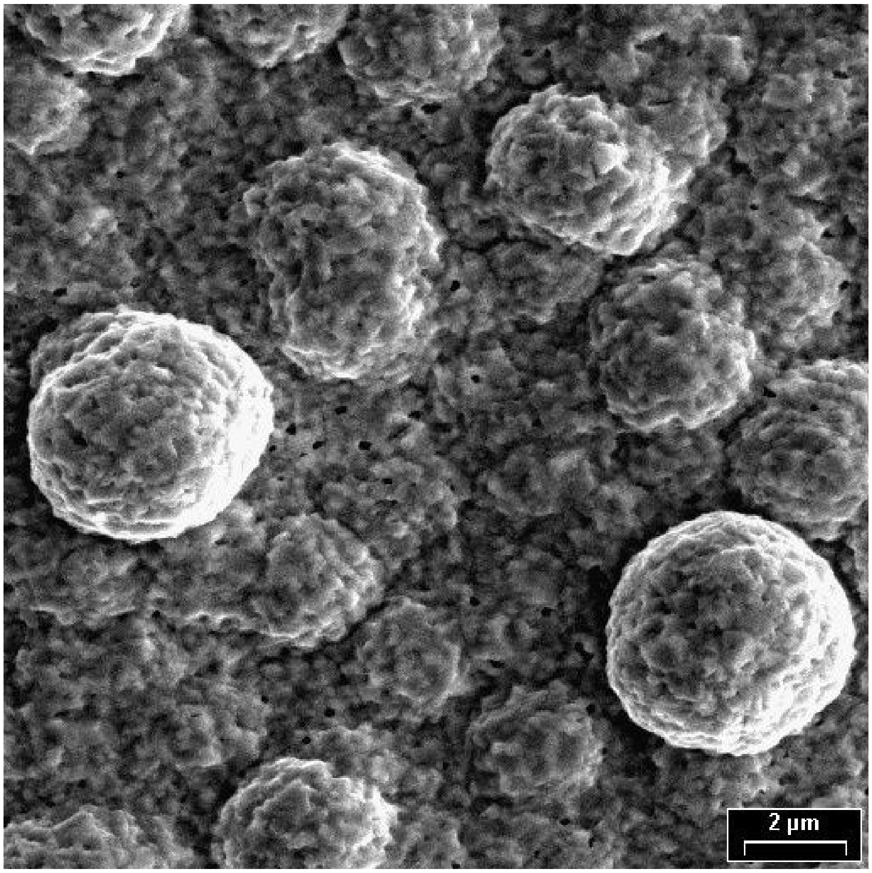

Figure 5-6: BMML deposition and the morphology of the porous Pd/Ag barrier layer on a non-porous stainless steel support

More interestingly, helium permeance data taken after the BMML deposition of the Pd/Ag layer, shown in Figure 5-7, showed no change in the bare support resistance.

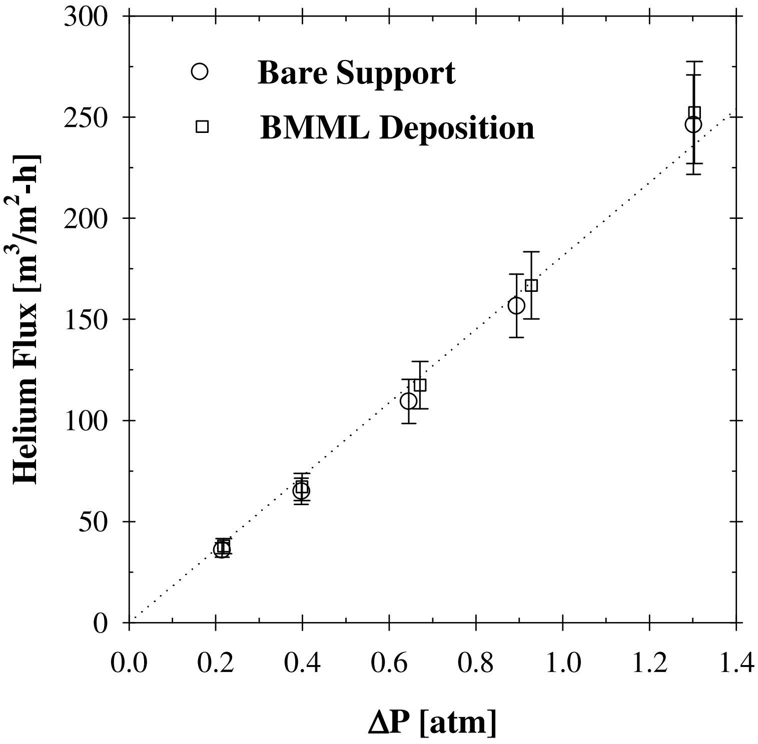

Figure 5-7: Room temperature helium permeance data for the bare PSS support before and after the BMML deposition

Furthermore, the combination of the helium permeance data in Figure 5-7 and the SEI micrographs in Figure 5-5 showed that the BMML deposition in fact generated a certain extent of grading of the PSS support without affecting its overall resistance.

The BMML deposition concept serves a dual purpose not only by producing a porous graded support, but also by forming a barrier layer for intermetallic diffusion to further improve the long-term stability of the Pd and/or Pd/Alloy membranes. The thermal stability in hydrogen permeance for membrane 002, presented in Figure 5-2 and Figure 5-4 substantiated the dual function of the BMML deposited layer.

The formation of a porous graded support by the BMML deposition would allow for the production of a membrane having a thinner hydrogen selective layer by some conventional and/or unconventional techniques such as electroless plating, electroplating and CVD related procedures. As discussed by Mardilovich *et al.*(2002), the thickness of the membranes and therefore the permeance obtained was dependent on the size of the largest pores present in the support surface. The final thickness of membrane 002 (Table 5-1) might be due to the presence of a large defect on the PSS surface.

In addition to the principal advantages stated above, a porous Pd/Ag layer should improve the adhesion between the hydrogen selective layer and the metal support. The improvement of adhesion was accomplished by the sintering of the Pd and Ag particles of the porous zone and the intermetallic diffusion at the boundaries of the porous layer with both the grains of the metal support and at the other side with the dense hydrogen selective layer.

It should also be noted that the intermetallic diffusion may still occur between the porous metal support and the porous Pd-metal barrier (Mardilovich *et al.*, 2006). However, both helium permeance data and the SEI micrographs revealed that the thermal stability of the Pd/Ag barrier layer had a direct relation with the morphology of this layer itself. The intermetallic diffusion between the metal support and porous Pd/Ag layer, therefore, was not expected to be harmful to the permeability of the hydrogen selective layer, since the layer acted as a trap and prevented further diffusion of the Fe, Ni and Cr from the PSS support into the hydrogen selective layer (Mardilovich *et al.*, 2006). The stability against intermetallic diffusion was clearly demonstrated by Mardilovich *et al.* (2006) for a BMML membrane with a 7.9 μm thick gas selective layer and a permeable surface area of 114.5 cm^2. An extended life test over a period of 1388 hours, showed a hydrogen permeance of 68.5 m^3/m^2-h-$atm^{0.5}$ at 500°C with no evidence of intermetallic diffusion of support metals into the 7.9 μm thick gas selective layer.

In addition, the porous Pd/Ag barrier layer may even enhance the permeability of this layer, if a Pd/Ag alloy is formed. To further investigate the contribution of Pd/Ag barrier layer as Pd/Ag alloy upon high temperature heat treatment, a coupon annealing study was conducted and will be discussed next.

5.3.3. Alloying of the Pd/Ag Barrier Layer

Another aspect of this study was to study the possible effects of the Pd/Ag barrier layers as Pd/Ag alloys at or above 500°C. To evaluate the morphology of the porous Pd/Ag barrier before and after annealing treatments, 0.5 μm media grade PSS plates were used as test supports. The supports were oxidized in air at 400°C for 6 hours. Then the supports were activated and plated sequentially for 30 minutes with Pd, then 90 minutes with Ag, another 30 minutes with Pd, 90 minutes with Ag and finally 30 minutes of Pd. The samples were rinsed between steps in the cycle, and at the end of each step a plate was withdrawn from the plating matrix, dried at 120°C and prepared for SEM, EDX and XRD analyses of the surface. In this way, representative samples of the surface were obtained for each stage in the cycle. Samples that were withdrawn from the plating matrix at each step in the cycle were also annealed to observe the changes in the morphology and the phases. Three different annealing conditions were used by varying the annealing temperature and annealing time. These were 500°C/He/10 hours for the 1st set of samples, 500°C/He for an additional 20 hours for the 2nd set of samples and 600°C/He/10 hours for the 3rd set of samples. Figure 5-8 shows the SEI micrographs of the specimens obtained at the end of each stage in the cycle, as well as the annealed surface after each annealing treatment of 500°C/He/10h, 500°C/He/+20h and 600°C/He/10h. After the first 30 minute Pd plating (Figure 5-8[a]-C1) the outline of sintered adjoining bare PSS particles were clearly visible having sizes in the 4-12 μm range. A large pore opening (~8 μm) was also visible in the center of Figure 5-8[a]-C1. Most of the visible surfaces appeared to be uniformly covered with Pd after the first 30 minute Pd plating. This Pd coating was comprised of small tightly knitted clusters, the majority of which were <100 nm in size. Figure 5-8[b]-C1 shows the surface after first Ag plating. The silver formed a much rougher surface layer comprised of irregular particles and clusters which did not appear to be as tightly knitted as the Pd clusters in Figure 5-8[a]-C1.

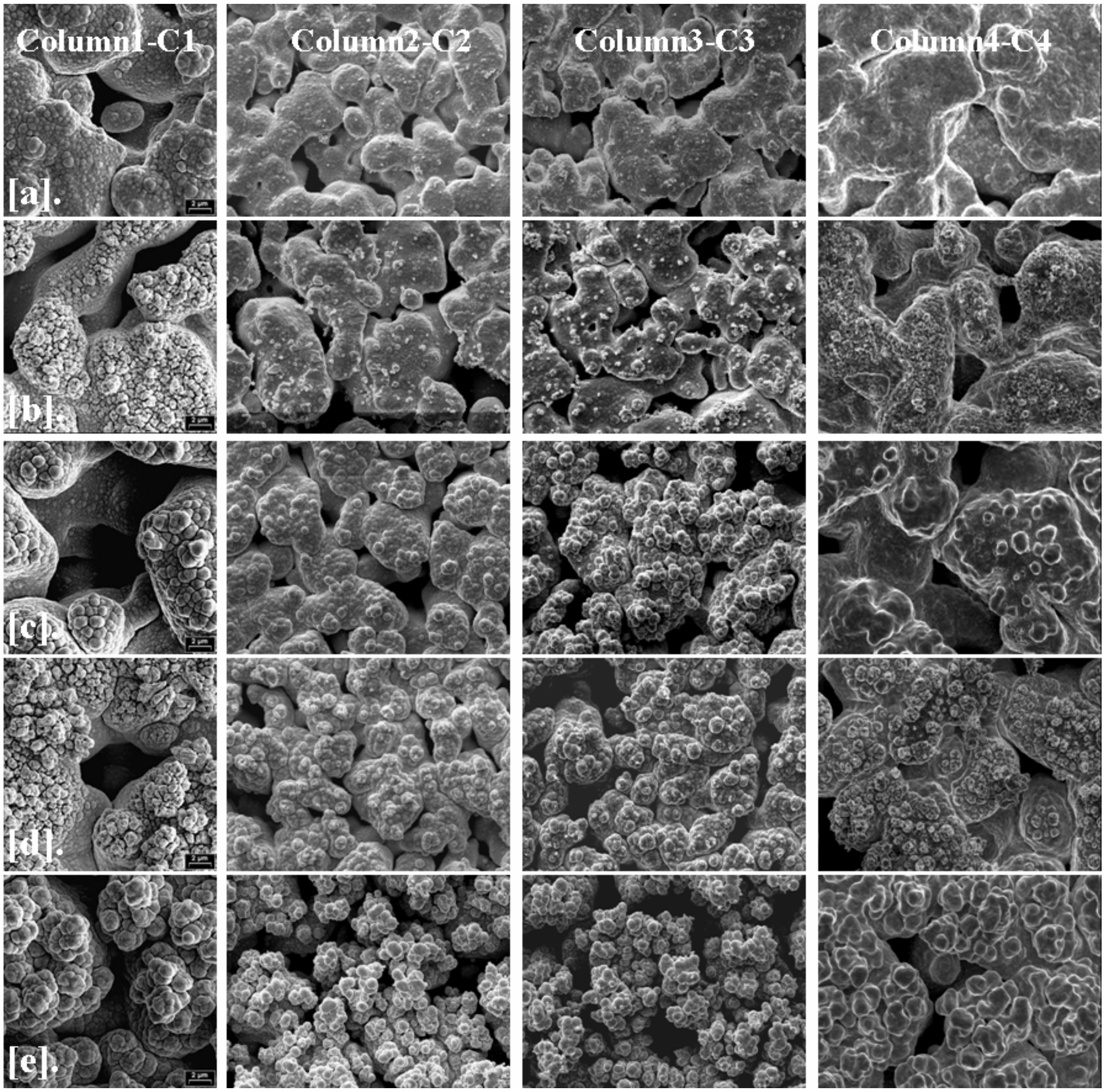

Figure 5-8: SEI micrographs of the steps in depositing a standard cycle of the 5 layer porous Pd/Ag inter-metallic diffusion barrier: [a]. First Pd, [b]. First Ag, [c]. Middle Pd, [d]. Second Ag, [e]. Final Pd (Column-1: As-synthesized (2kX), Column-2: Annealed @ 500°C/He/10h (1kX), Column-3: Annealed @ 500°C/He/+20h (1kX) and Column-4: Annealed @ 600°C/He/10h) (1kX)

Furthermore, the silver coverage did not appear to penetrate down into the pores. The visible surfaces at the bottom of the cavities and recessed areas in the center and upper left corner of Figure 5-8[b]-C1 appeared to be very similar to the entire plated surface shown in Figure 5-8[a]-C1. This indicates that these recessed areas were covered only by Pd from the first Pd plating. This assertion has been confirmed by similar observations from numerous other samples.

After the deposition of Ag, the morphology of subsequent Pd depositions was dramatically altered. In Figure 5-8[c]-C1, two distinct morphologies were clearly visible for the Pd. In the bottom of the large cavity in the center of Figure 5-8[c]-C1 the Pd was identical in appearance to the Pd deposits which covered the entire surface in Figure 5-8[a]-C1. Little or no silver deposition was likely to have occurred in this recessed region. Therefore, the only material covering the support in this region prior to the second Pd plating was Pd from the first Pd plating. The Pd in this region was similar in appearance to what would be expected from the later stages of Pd plating on a Pd-PSS membrane. However, the elevated regions surrounding the cavity in Figure 5-8[c]-C1 were likely to have been covered with a layer of rough, loosely packed, irregular Ag particles prior to the second Pd plating. It was in these regions that a new "silver directed" Pd morphology was observed. The silver directed Pd morphology had smooth loosely packed particles which were larger than the clusters in the Pd-only deposition morphology. Many of the Pd particles which developed on the surfaces previously covered by Ag in Figure 5-8[c]-C1 were 1-2 μm in size. As the Pd/Ag barrier formation cycle was continued, a repetition of the rough irregular Ag morphology was repeated in Figure 5-8[d]-C1, with little or no Ag deposition visible in the recessed regions. These unique deposition characteristics of Ag metal was one of the possible reasons for the unaffected overall support resistance, as observed in Figure 5-7, upon the BMML deposition. The final Pd plating in the cycle, shown in Figure 5-8[e]-C1, resulted in even larger Pd particles. These particles and clusters were less regular than those observed in the initial stages of Ag directed Pd deposition shown in Figure 5-8[c]-C1. Furthermore, the Pd-only deposition morphology, which dominated the surface in Figure 5-8[a]-C1, was scarcely visible in Figure 5-8[e]-C1. This indicates that in the advanced stages, the Pd-only deposition morphology was suppressed in favor of the larger, less regular, loose Pd clusters.

The SEI micrographs for the 500°C/He/10h and 500°C/He/+20h annealed samples are given in Columns 2 and 3 of Figure 5-8. At a temperature of 500°C, SEI micrographs (Column 2 of Figure 5-8[a]-[e]), representing the surface for each stage in the BMML deposition cycle, indicated that the changes in the deposition morphology upon alloying at 500°C were not significant. This temperature was above the Tamman temperature of

Ag metal (344°C), but below the Tamman temperatures for Pd (640°C) and the support metal (560°C). Similarly, the morphology of the samples, which were annealed at 500°C for an additional 20 hours (Column 3 of Figure 5-8[a]-[e]), remained the same as the SEI micrographs shown in Column 2 of Figure 5-8[a] to Figure 5-8[e] for the 500°C/He/10h annealed samples.

The final heat treatment was conducted at 600°C for 10 hours in helium. Following the altered deposition morphology after the Ag deposition, Figure 5-8[c]-C1, changes in the surface morphology of the 600°C/He/10h annealed sample, shown in Figure 5-8[a]-C4, was quite different. With the increasing Ag content and the layering as we move towards the 3rd, 4th and the final stages of BMML deposition, changes in the deposition morphology upon annealing at 600°C/He/10h were quite noticeable (Column 4 of Figure 5-8[c], [d] and [e]) most likely due to the cluster sintering between deposition metals Pd and Ag. At 600°C, the membrane temperature had approached to within 40°C of the Tamman temperature of Pd, which appears to be high enough to provide enough energy for cluster sintering and allow a significant migration of Ag to the Pd layer. The resulting surface of the completed porous Pd/Ag layer, shown in Figure 5-8[e]-C4, was comprised of loosely interconnected particles with clear voids and gaps. These particles seem to have been a little more regular in shape and size than the un-annealed Ag directed Pd morphology shown in Figure 5-8[e]-C1. The surface had a qualitative resemblance to the surfaces of un-plated and annealed porous metal supports, although the particle size was clearly much smaller. It is also noteworthy to mention that the porosity of the Pd/Ag barrier layer, shown in Figure 5-8 was maintained even after annealing at 500°C and 600°C.

The samples shown in Figure 5-8[e]-C1, [e]-C2 and [e]-C3 were used to obtain XRD patterns to see the phase changes before and after the annealing of the Pd/Ag barrier layers. The XRD patterns for the un-annealed and annealed samples, at 500°C/He/10h and 500°C/He/+20h respectively, are shown in Figure 5-9.

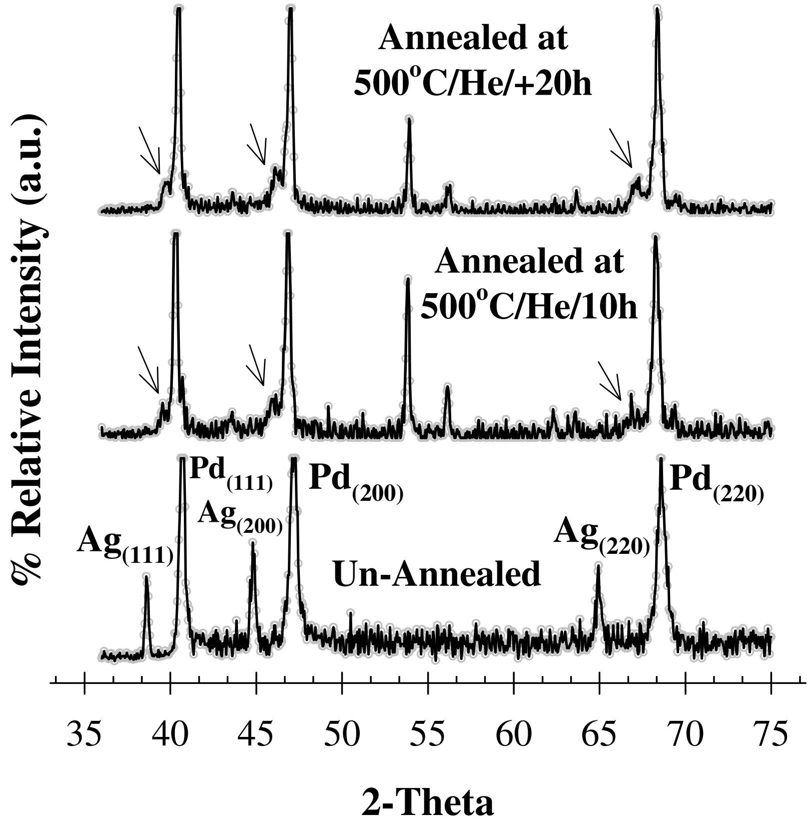

Figure 5-9: XRD patterns of a standard Pd/Ag barrier layer before and after annealing at 500 °C for 10 hours and an additional 20 hours in Helium

As expected, the un-annealed sample had patterns for both the pure fcc Pd and fcc Ag phases. The XRD patterns taken after annealing at 500°C/He/10h and 500°C/He/+20h indicated that the alloying of the porous Pd/Ag layers was not complete (Figure 5-9). Indeed, shoulders appeared at the characteristic planes (111), (200) and (220) indicated that the pure Pd and pure Ag phases co-existed with a Pd-rich Pd/Ag alloy phase, shown by the arrows in Figure 5-9. On the other hand, upon annealing at 600°C/He/10h, the porous Pd/Ag barrier was comprised of a single fcc Pd/Ag alloy as shown in Figure 5-10.

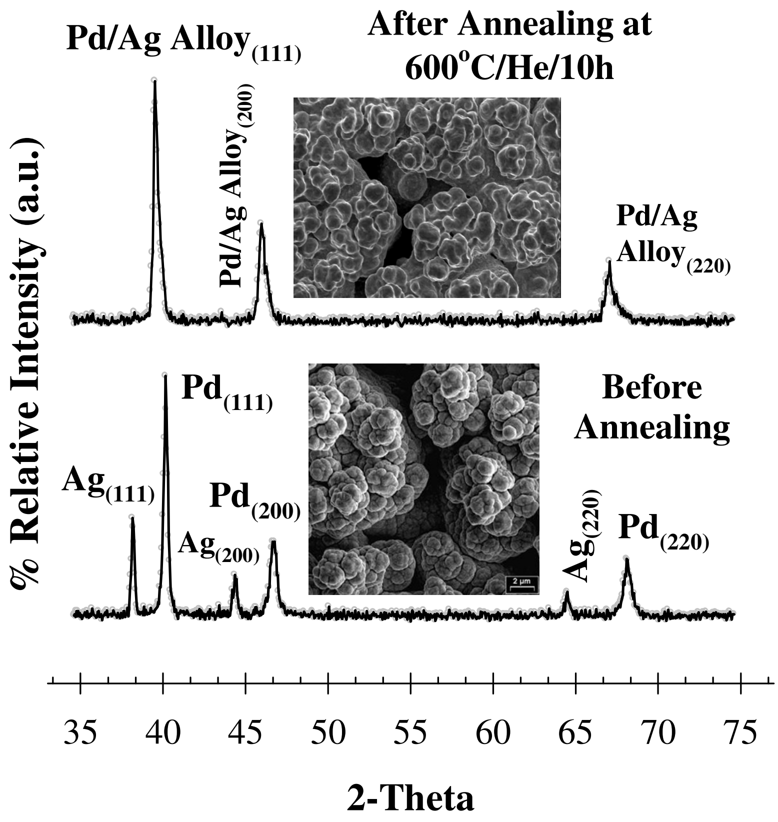

Figure 5-10: XRD patterns of a standard Pd/Ag barrier layer before and after annealing at 600 ℃ for 10 hours in Helium

These results were in good qualitative agreement with the literature results which indicated that the annealing temperatures at or above 500°C were required to achieve a homogeneous alloy (Uemiya *et al.*, 1991b; Shu *et al.*, 1996; Ayturk *et al.*, 2004a).

To further confirm the cluster sintering and the alloy phase formation at high annealing temperatures and the effect of alloying on the distribution of the deposited metals within the Pd/Ag barrier layer, cross-section EDX line scans, shown in Figure 5-11, were conducted for the un-annealed sample (Figure 5-8[e]-C1) and the sample annealed at 600°C/He/10h (Figure 5-8[e]-C4). As shown in Figure 5-11[a], the distribution of the wt% Pd and Ag metal compositions was consistent with the BMML deposition sequence of the as-synthesized Pd/Ag barrier layer. As mentioned earlier, standard 5-stage BMML deposition cycle was in the order of Pd/Ag/Pd/Ag/Pd.

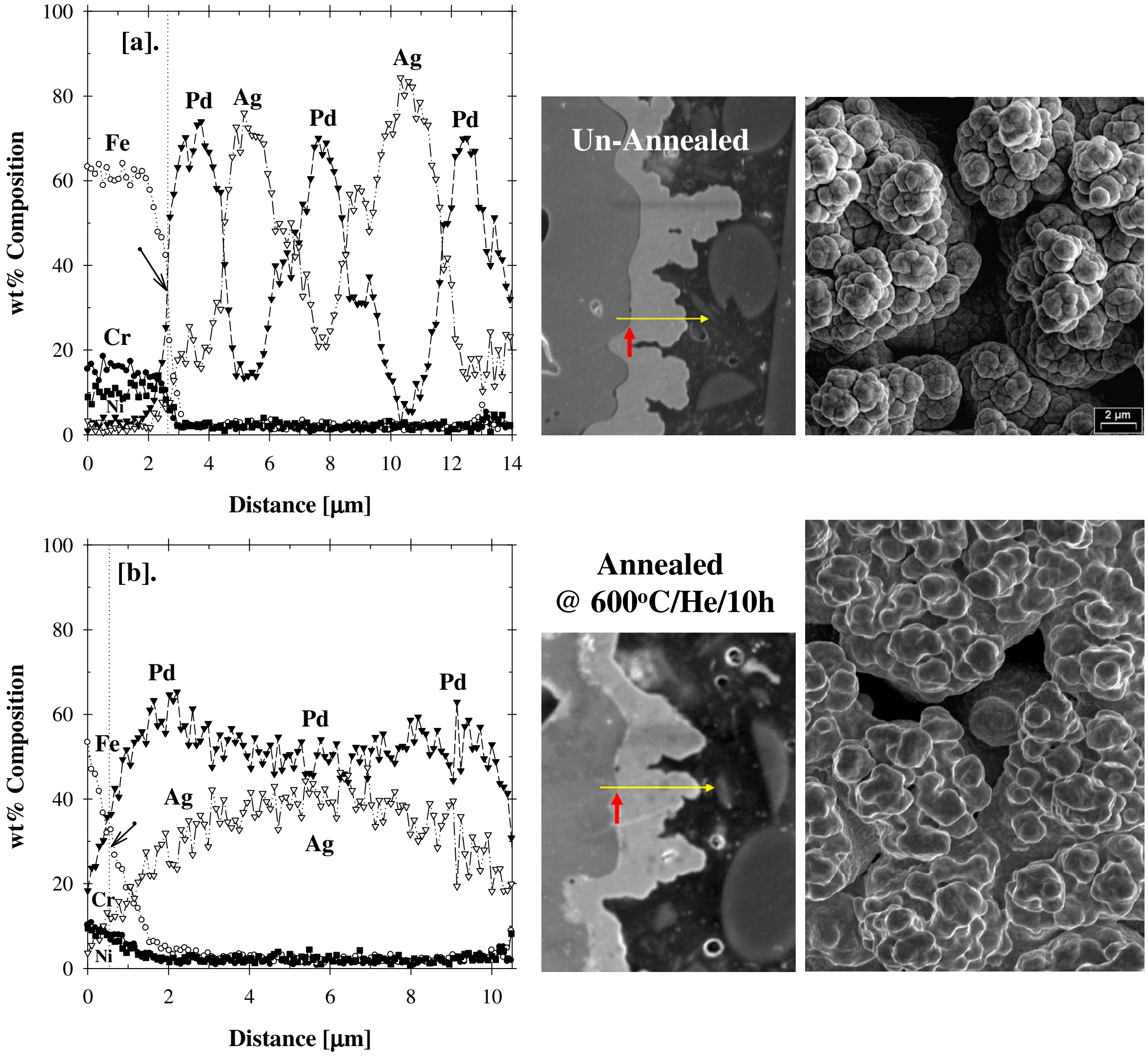

Figure 5-11: Cross-section EDX Line Scans [a] Before and [b] After Annealing at 600 ℃/He/10h (Interface is denoted by the dotted lines and marked by the arrows)

Upon annealing at 600°C/He/10h, the Pd and Ag metal compositions redistributed within the Pd/Ag barrier layer as shown in Figure 5-11[b], which was in good agreement with the top surface SEI micrographs for cluster sintering shown in Figure 5-8 and the XRD patterns for the alloy phase formation shown in Figure 5-10.

5.4. Conclusions

The most significant improvement in membrane performance has been the increase in the safe operational temperature of the composite Pd/PSS and Pd/Alloy/PSS membranes to 500°C and above. This has been achieved by the development of a method to produce a porous Pd/Ag intermetallic diffusion barrier layer on the surface of the support, prior to application of the dense hydrogen selective layer. The synthesis of the porous Pd/Ag barrier was conducted by the bi-metal multilayer (BMML) deposition technique. The porosity of the Pd/Ag barrier layer was confirmed with the room temperature helium permeance measurements coupled with the SEI micrographs of the deposition morphology. The porosity of the Pd/Ag layer upon annealing was also stable at 500°C and above. Furthermore, the XRD phase identification and cross-section EDX line scan analyses showed that the Pd/Ag barrier layer formed an fcc Pd/Ag alloy phase upon high temperature annealing at 600°C. The porous Pd/Ag barrier was extremely effective as a barrier layer against intermetallic diffusion, which significantly improved the thermal and long-term stability of the membranes for high temperature applications.